



저작자표시-비영리-변경금지 2.0 대한민국

이용자는 아래의 조건을 따르는 경우에 한하여 자유롭게

- 이 저작물을 복제, 배포, 전송, 전시, 공연 및 방송할 수 있습니다.

다음과 같은 조건을 따라야 합니다:



저작자표시. 귀하는 원저작자를 표시하여야 합니다.



비영리. 귀하는 이 저작물을 영리 목적으로 이용할 수 없습니다.



변경금지. 귀하는 이 저작물을 개작, 변형 또는 가공할 수 없습니다.

- 귀하는, 이 저작물의 재이용이나 배포의 경우, 이 저작물에 적용된 이용허락조건을 명확하게 나타내어야 합니다.
- 저작권자로부터 별도의 허가를 받으면 이러한 조건들은 적용되지 않습니다.

저작권법에 따른 이용자의 권리는 위의 내용에 의하여 영향을 받지 않습니다.

이것은 [이용허락규약\(Legal Code\)](#)을 이해하기 쉽게 요약한 것입니다.

[Disclaimer](#)

공학박사 학위논문

**Low field magnetoresistance in
LSMO-based composites and
MnZn ferrites**

LSMO - 기반 복합체와 MnZn 페라이트의
저자장 자기저항효과 연구

2014년 8월

서울대학교 대학원

재료공학부

김 효 진

Abstract

Low field magnetoresistance in LSMO-based composites and MnZn ferrites

Hyo-Jin Kim

Department of Materials Science and Engineering

The Graduate School

Seoul National University

Enhanced low field magnetoresistance (LFMR) in Perovskite type $\text{La}_{0.7}\text{Sr}_{0.3}\text{MnO}_3$ (LSMO)-based composite bulks and films have been successfully investigated. LSMO is one of the most attractive LFMR materials since it has high Curie temperature ($T_C \approx 370$ K) which makes it possible to fabricate devices operating at room temperature. The LFMR effect, normally observed at the temperatures below T_C in low fields (< 0.2 T), is attributable to a spin-polarized tunneling at the grain boundaries, and thus, it is very important to control the microstructures of LSMO polycrystalline samples for the enhancement of LFMR. In comparison with a pure polycrystalline LSMO sample, the LSMO-based composites exhibited

much improved LFMR effect, which was normally accompanied by a significant increase in their electrical resistivities and an abrupt decrease in their T_C values. In this research, we mainly focused to enhance the LFMR effects in LSMO-based composite at room temperature (RT) with out increase in resistivity and decrease in T_c values. First, we systemically investigated that the second phases like La_2O_3 and Mn_2O_3 (or Mn_3O_4), chemically compatible with LSMO, were very effective for avoiding such a serious degradation in both T_C and electrical conductivity. In order to improve the LFMR effect of LSMO, in this study, we tried to modify the LSMO grain boundaries by forming the second phases of La_2O_3 and eutectic structures between LSMO and manganese oxide via solid state reaions and liquid phase sintering, respectively. Second, we investigated the LFMR properties of pure LSMO and LSMO-manganese oxide composite films prepared by aerosol deposition (AD). As-deposited films by the AD method were post-annealed at 1100, 1200°C for the recovery of magnetism and also for a modification of LSMO grain boundary. While as-deposited films commonly exhibited a poor LFMR property with depressed T_c , post-annealed films exhibited a very good LFMR property with high T_c values ranging from 355 to 370 K. The highest LFMR value of 1.2% in 0.5 kOe and unprecedentedly high $(dMR/dH)_{\text{max}}$ value of 158.8 % kOe⁻¹ were obtainable at 300 K from the LSMM composite film annealed at 1200°C.

Futhermore, we carried out to find new materials such as spinel ferrites for real LFMR devices. MnZn ferrite is a ferrimagnetic material with the spinel structure and has the high T_c of ~ 600 K. It is clear that a LFMR sensor should be operated at temperatures close or even higher than RT; therefore, due to the fact that the LFMR properities become weaker at high

temperature, the possible applications of these MnZn ferrites are challenging. However, the origin for LFMR effects in MnZn ferrites, even though spinel ferrites, has not been clarified yet. We first attempt to understand the mechanism of the LFMR properties and to obtain an enhanced LFMR properties of MnZn ferrites. Therefore, numerous mechanism for understanding LFMR properties in MnZn ferrites and various attempts for improving the LFMR properties of MnZn ferrites have been suggested in literatures. We confirmed that the LFMR properties of Ga-doped MnZn ferrites were systemically investigated the microstructures, electric properties, and magnetotransport properties depending on the various amounts of Ga₂O₃ and sintering conditions. From these studies, LFMR value of 3.1% in 0.5 kOe at RT is achieved from 2 mol% Ga-doped MnZn ferrites fabricated by two step sintering. The data measured by complex impedance (Z^*) spectroscopy revealed that the variation of LFMR values in samples was exactly coincident with those of differences in activation energy (E_a) values between grain and grain boundary.

Keywords: Perovskite manganites, spinel ferrites, La_{0.7}Sr_{0.3}MnO₃ (LSMO), LSMO-manganese oxide composite, MnZn ferrites, Ga-doped MnZn ferrites, aerosol deposition (AD), post-annelaing, low filed magnetoresistance (LFMR), spin dependent scattering, magneto transport property, magnetic property, electrical property

Student Number: 2008-20640

Contents

List of Tables and Figures	vii
Chapter 1 General Introduction.....	1
Chapter 2 General Background	7
2.1 The phenomena of magnetoresistance (MR).....	7
2.2 LFMR and spin-dependant scattering.....	10
2.3 LFMR properties in perovskite manganites and spinel ferrites	12
2.3.1 LFMR properties of perovskite manganites	12
2.3.2 LFMR properties of spinel ferrites	17
Chapter 3 LSMO-La ₂ O ₃ composites.. ..	45
3.1 Introduction.....	45
3.2 Experimental	46
3.3 Results and discussion.....	47
3.4 Conclusions	51

Chapter 4 LSMO-manganese oxide composite prepared by liquid phase sintering.....	62
4.1 Introduction.....	62
4.2 Experimental	62
4.3 Results and discussion.....	63
4.4 Conclusions.....	68
 Chapter 5 LSMO-manganese oxide composite thick films prepared by aerosol deposition.....	 77
5.1 Introduction.....	77
5.2 Experimental	77
5.3 Results and discussion.....	79
5.4 Conclusions.....	84
 Chapter 6 Ga-doped MnZn ferrites	 95
6.1 Introduction.....	95
6.2 Experimental	96
6.3 Results and discussion.....	97
6.3.1 LFMR properties of Ga-doped MnZn ferrites	97
6.3.2 Effects of the the annealing conditions on the LFMR properties of Ga-doped MnZn ferrites	101

6.4 Summary	106
Chapter 7 Summary	130
Publications	133
Abstract in Korean	135

List of Tables

Table 3.1. Sample identifications (IDs) and properties of LSMO and LSMO - La₂O₃ composites: sample resistivity (ρ), MR at 100 and 300 K and $(dMR/dH)_{\max}$ at 300 K.....55

Table 4.1. Sample identifications (IDs) and properties of the LSMO and LSMO - manganese oxide composite samples. Mn mole fraction, $f_{\text{Mn}} = \text{Mn}/(\text{La}+\text{Sr}+\text{Mn})$ in the total precursor powders, sample resistivity (ρ) at 290 K, MR at 290 K in 500 Oe and $(dMR/dH)_{\max}$ at 290 K 70

Table 5.1. Sample identifications (IDs) and properties of samples: Curie temperature (T_c), Coercivity (H_c), resistivity (ρ) measured at 300 K, MR values at 100 K in 1.5 kOe, MR values and $(dMR/dH)_{\max}$ values at 300K in 0.5 kOe of the LSMO and LSMO-manganese oxide composite films prepared at the T_{an} of 1100 and 1200°C, respectively. The data from ref. [9] for the composite bulk with the same composition are also listed for a comparison.87

Table 6.1. Properties of Ga-doped MnZn ferrites: sample resistivity (ρ),

LFMR and $(dMR/dH)_{\max}$ at RT, and relative sintered density 110

Table 6.2. Atomic percentages of Fe^{2+} and Fe^{3+} ions in 2 mol% Ga-doped MnZn ferrites prepared by different sintering conditions. The data were analyzed by XPS..... 111

Table 6.3. The evaluated E_g , E_{gb} , $E_{\text{gb}}-E_g$, ρ_g , ρ_{gb} , C_g , and C_{gb} values of 2 mol% Ga-doped MnZn ferrites prepared by different sintering conditions. These data were analyzed by Impedance analysis 112

List of Figures

Fig. 2.1. The magnetoresistance family	28
Fig. 2.2. Top panel: $\rho (T)$ of $\text{La}_{2/3}\text{Sr}_{1/3}\text{MnO}_3$ for a single-crystal sample and two polycrystalline samples with final sintering temperatures of 1300 and 1700°C. Bottom panel: the temperature dependence of the magnetization for these three samples at 0.5 T. Inset: the field-dependent magnetization of these three samples at 5 and 280 K. (data from ref. [18])	29
Fig. 2.3. (a), (c), (e) The magnetic field dependence of the normalized resistance at various temperatures from 5 to 280 K. (c), (d), (f) The magnetic field dependence of the magnetization (normalized to the 5 T value) at various temperatures from 5 to 280 K. (data from ref. [18])	30
Fig. 2.4. The ideal cubic $\text{RE}_{1-x}\text{AE}_x\text{MnO}_3$ perovskite structure.....	31
Fig. 2.5. Structure of distorted perovskite manganese: (a) orthorhombic and (b) rhombohedral structures.	32

Fig. 2.6. Schematic view of the band structure of ferromagnetic-doped LaMnO_3 . The energies and filling of the bands correspond to $\text{La}_{2/3}\text{Sr}_{1/3}\text{MnO}_3$. The level diagram on left is that of an isolated Mn ion in an octahedral crystal field. (data from ref [23])33

Fig. 2.7. (left) Phase diagram of temperature versus tolerance factor and average radius of cation at A site for the system $\text{RE}_{0.7}\text{AE}_{0.3}\text{MnO}_3$. (right) Phase diagram showing transition temperature versus concentration, x , of single crystals of $\text{La}_{1-x}\text{Sr}_x\text{MnO}_3$. (data from [23]).....34

Fig. 2.8. High resolution TEM images for (a) single grain boundary for pure LSMO sample and (b) the MgO located between LSMO grains for 5 mol% MgO added LSMO composite sample, LFMR behaviors of (c) pure LSMO sample and composite sample (5 and 10 mol% MgO added composite samples). (data from ref. [52]).....35

Fig. 2.9. (a) cross-sectional TEM images of the LSMO : ZnO vertical aligned nanocomposite (VAN) film deposited by PLD at 1 Hz. The marked distance is 10 domain periods (19.4 nm) along the vertical interface. “Z” stands for ZnO phase and “L” represents the LSMO phases. (b) TEM image

of the 10 Hz VAN film. The insets are the corresponding SAED patterns from the films. (c) MR as a function of temperatures for LSMO : ZnO VAN films deposited at different frequencies. Resistivity ratio ρ_H/ρ_0 and magnetic hysteresis loop of 10 Hz VAN films as a function of magnetic field at a temperature of 40 K. (data from ref. [53])36

Fig. 2.10. (a)-(d) Electron diffraction patterns from different composites and the corresponding TEM photographs. (e) and (f) HRTEM images of LSMO and 50 mol% CeO₂ adding samples. (g) Low field dependence of resistance $\rho(H)/\rho(H_c)$ of several composites at 5 K. Right inset: the partial enlarged figure, left inset: the variation of MR value with increasing LCMO in a 0.05 T at 5 K37

Fig. 2.11. The LFMR values of various LSMO based-composite bulks measured at RT in 0.5 kOe. Additional materials: La₂O₃ (present study), CeO₂ (data from ref. [39]), Mn₂O₃ (data from ref. [30]), glass (data from ref. [50]), NiO (data from ref. [45])38

Fig. 2.12. The ideal cubic *MeFe₂O₄* spinel structure.....39

Fig. 2.13. Magnetic moment in transition metal-zinc ferrites as $T = \text{Cu, Ni, Co, and so on are substituted for divalent iron. (data from ref. [59])}$	40
Fig. 2.14. The resistivities of various spinel ferrites with sintering temperature. (data from ref. [60])	41
Fig. 2.15. The magnetization versus temperature curves of various spinel ferrites. (data from ref. [61]).....	42
Fig. 2.16. Temperature dependence of D.C. resistivity for several spinel ferrites. (data from ref. [64]).....	43
Fig. 2.17. Room temperature MR of (a) single crystal, (b) polycrystalline film, and (c) powder compact. Note the different resistivity scales. (data from ref. [67]).....	44
Fig. 3.1. XRD patterns of pure LSMO and LSMO–La ₂ O ₃ composites.....	56
Fig. 3.2. SEM back-scattered electron images of samples: (a) LSMO, (b) LS–L1, (c) LS–L2, (d) LS–L3 (e) LS–L4, (f) LS–L5. Low magnification	

micrographs are for the samples of (g) LS-L5 and (h) LS-L6.....	57
Fig. 3.3. The average LSMO grain size of samples as a function of the La_2O_3 content.....	58
Fig. 3.4. Temperature dependence of magnetization for samples. The $M-T$ curves were measured with field-cooled warming procedure under the applied field of 100 Oe.....	59
Fig. 3.5. The LFMR behaviors of samples measured at (a) 100 K and (b) 300 K. The electrical resistivity and LFMR values of samples are plotted as a function of the La_2O_3 content at (c) 100 K in 1500 Oe and (d) 300 K in 500 Oe.....	60
Fig. 3.6. The $R(H) / R(H=O)$ ratios of LSMO and LS-L4 samples, measured at 100 and 300 K, versus the applied field up to 1 T.....	61
Fig. 4.1. XRD patterns of pure LSMO and LSMO-manganese oxide composites sintered at 1450°C for 1 h in air.....	71

Fig. 4.2. SEM back-scattered electron images of (a) LSMO, (b) LSM1, (c) LSM2, (d) LSM3, (e) LSM4, and (f) LSM5 72

Fig. 4.3. (a) Z-contrast STEM image of the LSM3 sample and (b) the La, Sr, Mn, and O spectral images. (c) Cross-sectional TEM images of the LSM3 sample. Inset is SAD patterns of A and B areas (d) HR-TEM images of the LSMO (marked by P) and Mn₃O₄ phases (marked by A, B, C and D). Insets are FFT patterns of A, B, C and D areas in (c) 73

Fig. 4.4. The ρ - T curves for LSMO and LSMO-manganese oxide composite samples 71

Fig. 4.5. Temperature dependence of magnetization for samples. The M - T curves were measured with field-cooled warming procedure under the applied field of 100 Oe 75

Fig. 4.6. The LFMR behaviors of the LSMO and composite samples measured at 290 K in 500 Oe 76

Fig. 5.1. XRD patterns of (a) calcined LSMO powder, *as*-deposited LSMO

film by AD process, and annealed LSMO films, and (b) calcined LSMM composite powder, *as*-deposited LSMM composite film by AD process, and annealed LSMM composite films 88

Fig. 5.2. SEM micrographs of (a) *as*-deposited LSMO, and (b) composite films, (c) LSMO film, and (d) LSMM composite film annealed at 1100°C, and (e) LSMO film and (f) LSMM composite film annealed at 1200°C 89

Fig. 5.3. The cross-sectional TEM images of the (a) LSMO and (b) LSMO composite films annealed at 1200°C. The cross-sectional Z-contrast STEM images of the (c) LSMO and (d) LSMM composite film, and the La, Sr, Mn spectral images. High resolution TEM images of the (e) LSMO and (f) LSMM composite film, and inset in (e) and (f) represents FFT patterns of the square area related by a yellow line 90

Fig. 5.4. $\rho - T$ curves for post-annealed LSMO and LSMM composite films 91

Fig. 5.5. The $M-T$ curves for annealed LSMO films and LSMM composite films. Inset figure shows the $M-T$ curves for *as*-deposited LSMO and composite films by AD process 92

Fig. 5.6. The LFMR behaviors of post-annealed films: (a) LSMO and (b) LSMM composite films measured at 100 K, (c) LSMO and (d) LSMM composite films measured at 300 K.....93

Fig. 5.7. The $R(H) / R(H=0)$ ratios of LSMO and LSMM composite films annealed at 1200°C, versus the applied field up to 10 kOe, measured at 100 and 300 K.....94

Fig. 6.1. Schematic of the magnetoresistance measurement system 113

Fig. 6.2. ((a) The XRD patterns and (b) the variation of the lattice constants of $(\text{Mn}_{0.8}\text{Zn}_{0.2})_{(1-x)}\text{Ga}_x\text{Fe}_2\text{O}_4$ ($x = 0, 0.01, 0.02, 0.03, 0.05, 0.1$) samples..... 114

Fig. 6.3. SEM micrographs of (a) 0, (b) 2, (c) 3, (d) 5, and (e) 10 mol% Ga-doped MnZn ferrites. The average grain sizes versus the Ga_2O_3 contents in $(\text{Mn}_{0.8}\text{Zn}_{0.2})_{(1-x)}\text{Ga}_x\text{Fe}_2\text{O}_4$ ($x = 0, 0.01, 0.02, 0.03, 0.05, 0.1$) samples 115

Fig. 6.4. (a) Temperature dependence of magnetization for MnZn ferrites. The $M-T$ curves for the samples with $x = 0$ and 0.02 in $(\text{Mn}_{0.8}\text{Zn}_{0.2})_{(1-x)}\text{Ga}_x\text{Fe}_2\text{O}_4$ were measured with field-cooled warming procedure under the

applied field of 3kOe. (b) $M-H$ curves and (c) M/M_s-H curves for the samples with $x = 0, 0.02, 0.05, \text{ and } 0.1$ 116

Fig. 6.5. The temperature dependence of resistivity for the $(\text{Mn}_{0.8}\text{Zn}_{0.2})_{(1-x)}\text{Ga}_x\text{Fe}_2\text{O}_4$ ($x = 0, 0.01, 0.02, 0.03, 0.05, 0.1$) samples. (a) Resistivity (ρ) vs T and (b) $\log \rho$ vs T plots. 117

Fig. 6.6. The LFMR behaviors at RT for undoped and Ga-doped MnZn polycrystalline samples with $x = 0, 0.02, 0.03, 0.05, \text{ and } 0.1$ in $(\text{Mn}_{0.8}\text{Zn}_{0.2})_{(1-x)}\text{Ga}_x\text{Fe}_2\text{O}_4$ 118

Fig. 6.7. $R(H)/R(H=0)$ at RT as a function of the applied magnetic field up to 0.3 kOe for Ga-doped MnZn ferrites with $x = 0, 0.2, 0.03, 0.05, \text{ and } 0.1$ 119

Fig. 6.8. XRD patterns of 2 mol% Ga-doped MnZn ferrite samples with various sintering conditions in air 120

Fig. 6.9. SEM micrographs of 2 mol% Ga-doped MnZn ferrites samples sintered at (a) 1250°C, (b) 1300°C, (c) 1350°C, and (d) 1400°C for 2 h in air 121

Fig. 6.10. The relationship among relative sintered density, average grain size (d_g), dc resistivity (ρ), and LFMR at RT of 2 mol% Ga-doped MnZn ferrite samples as a function of sintering temperatures (a) and holding periods (b)	122
Fig. 6.11. The heat treatment schedules for the one step and two step sintering.....	123
Fig. 6.12. XRD patterns of 2 mol% Ga-doped MnZn ferrite samples prepared by three different sintering conditions	124
Fig. 6.13. SEM micrographs of MnZn ferrite samples with $x = 0.2$ sintered by (a) one step sintering, (b) two step sintering for 5 min, and (c) two step sintering for 10 min.....	125
Fig. 6.14. SEM micrograph (a) and its EBSD image (b) for 2 mol% Ga-doped MnZn ferrite sample sintered by two step sintering for 10 min	126
Fig. 6.15. (a) XPS data of 2 mol% Ga-doped MnZn ferrite sample prepared by three different sintering conditions. The dotted region in (a) was enlarged	

in (b)..... 127

Fig. 6.16. The relationship among relative density, grain size (d_g), dc resistivity (ρ), and LFMR at RT of samples prepared by three different sintering conditions..... 128

Fig. 6.17. Z'' properties of samples sintered by (a) one step sintering, (c) two step sintering for 5 min, and (e) two step sintering for 10 min in the measurement frequency ranging from 10^2 to 10^7 Hz. The Arrhenius plots of $T\sigma$ versus $1000/T$ of samples sintered by (b) one step sintering, (d) two step sintering for 5 min, and (f) two step sintering for 10 min 129

Chapter 1. General Introduction

$RE_{1-x}A_xMnO_3$ perovskite manganites (where RE is a rare earth element and A is a divalent cation), exhibiting the colossal magnetoresistance (CMR) effect, have drawn a considerable attention in recent years because of their abundant physical properties and potential applications such as magnetoresistive transducers and sensors [1,2]. LSMO is one of the most attractive CMR materials since it has high Curie temperature ($T_C \approx 370$ K) which makes it possible to fabricate devices operating at room temperature [3, 4]. The MR effects of LSMO polycrystalline materials have two types of high-field and low-field MR, depending on their origin [5-8]. The high field MR (HFMR) effect is observable at the temperatures below T_C only in high fields (>1 T). The HFMR effect originates from the existence of a noncollinear spin structure in the surface layer. On the other hand, a low field MR (LFMR) effect can be observed at the temperatures below T_C in low fields (< 0.2 T). A number of subsequent studies, both on bulks and films, have confirmed the important role of grain boundaries as a source of the LFMR effect. The LFMR is usually interpreted in terms of spin-polarized tunneling through electronic barriers across the grain boundaries. Hence, the nature and size of grain boundaries plays a major role in the LFMR mechanism. Unfortunately, the LFMR values of the CMR manganites rapidly decrease with increasing temperature and thus become very small at room temperature. The rapid degradation of the LFMR effect with increasing temperature is intimately related to the magnetism of grain boundary which is significantly different from that of grain because the grain boundary can act as not only

spin-dependent scattering centers but also the spin-flipping centers degrading the LFMR effect [9-12]. Therefore, for the enhancement of the LFMR effect, it is very critical to control the grain boundary properties of LSMO polycrystalline samples. In this research, we mainly focused to enhance the LFMR effects in LSMO-based composite at RT for the real magnetic sensor application.

Next, the discovery of the LFMR effects in perovskite manganites revolutionized material science and a lot of effort has been carried out to find magnetals with improved MR around room temperature in low magnetic fields [13-17]. Particularly, the ferrimagnetic magnetite (Fe_3O_4), with a T_c of 858 K, is a very good candidate to show the required properties. The epitaxial Fe_3O_4 films show no MR in low fields, whereas the polycrystalline sample exhibits an MR of 1.7% at RT in 1.5 kOe, indicative of the spin-polarized tunneling between the adjacent grains [17]. It is similar to LFMR effects in perovskite manganites. In other words, grain boundaries are believed to be important in understanding the LFMR properties of the ferrimagnetic materials. However, the reason for the LFMR property in this material is still not clear. Even the conclusion about the natural grain boundaries resistance is also not clear. The data for LFMR effects in ferromagnetic spinel ferrites from the bulks and films are very limited and not specific to the grain boundaries properties. The aim of this study is to present the relationships between microstructure, grain boundary properties, electrical properties, and LFMR properties in MnZn ferrites. In addition, we carefully investigated the annealing conditions and doping effects on MnZn ferrites to obtain a single phase of MnZn ferrites. The condition for LFMR observation have been revealed, and the experimental results have been

explained by magnetically disordered grain boundaries model. The major results of this literature are summarized as the following.

First, we report the enhanced LFMR properties of composite bulks of (1-x) LSMO - x La₂O₃ (x= 0, 0.025, 0.05, 0.075, 0.1, 0.2, 0.3) prepared using the conventional solid state reaction. In order to improve the LFMR effect, grain boundary engineering is very crucial since more effective spin-dependent tunneling barriers are achievable at the grain boundaries. Since La₂O₃ phases are thermodynamically compatible with LSMO at high temperatures, all composite samples are composed of two different phases of LSMO and La₂O₃. While the T_c of all composites were almost unaltered in the range of 355~358 K, an optimally processed LSMO-La₂O₃ composite exhibited greatly enhanced LFMR of 2.22% at 300 K in 500 Oe with only one order increase in its resistivity in comparison with LSMO. We also tried to modify the LSMO grain boundaries of the LSMO-manganese oxide composite by liquid phase sintering above the eutectic temperature between LSMO and Mn₂O₃ since a large increase in effective spin scattering center at the grain boundaries would be hopefully enabled by a eutectic structure of LSMO and manganite oxide after liquid phase sintering. We here report that it is possible to obtain improved LFMR effects from the LSMO-manganese oxide composites prepared by liquid phase sintering. The maximum LFMR value of 1.28% at 290 K in 500 Oe could be achieved from the composite sample of 30 mol% Mn₂O₃ addition. We also studied a LSMO based composite film system prepared by AD. As-deposited films by the AD method were post-annealed at 1100 and 1200°C for 2 h in air for the recovery of magnetism and also for a modification of LSMO grain boundary. While as-deposited films commonly exhibited a poor LFMR property with

depressed T_c , post-annealed films exhibited a very good LFMR property with high T_c values ranging from 355 to 370 K. The highest LFMR value of 1.2% in 0.5 kOe and unprecedentedly high $(dMR/dH)_{\max}$ value of 158.8 % kOe⁻¹ were obtainable at 300 K from the LSMM composite film annealed at 1200°C. Compared with pure LSMO film, the LSMM composite films possess higher LFMR values with higher $(dMR/dH)_{\max}$ values, which is mainly attributed to a greatly reduced magnetically disordered region near the LSMO grain boundary because of chemically compatible Mn₃O₄ phase.

Second, for the first time, we confirmed that the LFMR properties of Ga₂O₃-doped Mn-Zn ferrites were systematically investigated the microstructures, electric properties, and magnetotransport properties depending on the various amounts of Ga₂O₃ and sintering conditions. Various amounts of Ga₂O₃ were doped to a pure Mn-Zn ferrite to have the nominal composition of (Mn_{0.8}, Zn_{0.2})_{1-x}Ga_xFe₂O₄ ($x = 0\sim 0.1$). The maximum LFMR value of 2.5% in 0.5 kOe at RT could be obtained from the $x = 0.02$ sample sintered at 1400°C for 2 h in air. In order to confirm the annealing condition effects on LFMR properties, 2 mol% Ga₂O₃-doped Mn-Zn ferrites were fabricated by two kinds of sintering processing schedule, which are named by one-step and two step sintering method. While one-step sintering means that the samples were directly ramped up to the sintering temperature, two-step sintering means that the samples were heated up to sintering temperature, and then more heated up to the final firing temperature, held for short time (5 and 10 min, in this experiment, respectively). From this studies, LFMR value of 3.1% in 0.5 kOe at RT is achieved from 2 mol% Ga₂O₃-doped Mn-Zn ferrites fabricated by two step sintering.

Finally, we clarified the origins of enhanced LFMR properties in

MnZn-ferrites. Annealed by 1-step (at 1300°C for 2h) and 2-step (sintered at 1300°C for 2 h and then directly additional sintered at 1400°C for 5 and 10 min, respectively) for 2 mol% Ga₂O₃-doped Mn-Zn ferrite samples were used for this work, respectively. For MnZn-ferrites, the LFMR properties showed a strong dependence on the electric, magnetic properties and microstructures. While sample annealed by 1-step sintering at 1300°C for 2h showed the resistivity value of ~11,994 Ωcm with LFMR value of 2.81% at RT, annealed by 2-step sintering with holding time of 5 min showed the resistivity value of ~1,860 Ωcm with LFMR value of 2.98% at RT. It was accompanied by a very high increase in the electron hopping between Fe²⁺ and Fe³⁺ with the almost same average grain size of ~10 μm. With further increasing additional annealing holding time up to 10 min, an abnormal grain growth was occurred. This sample with the average grain size of ~100 μm showed the LFMR value of 3.07% with relatively lower resistivity of ~262 Ωcm at RT. The data measured by complex impedance (Z^*) spectroscopy revealed that the variation of LFMR values in samples was exactly coincident with those of differences in activation energy (E_a) values between grain and grain boundary. With increasing the difference in E_a between grain and grain boundary, LFMR value of samples was increased, indicating that the LFMR property in MnZn-ferrites was originated from the spin dependent scattering at the grain boundary.

References

- [1] R. von Helmolt et al., *Phys. Rev. Lett.* **71** (1993) 2331.
- [2] S. Jin et al., *Science* **264** (1994) 413.
- [3] Hwang H Y et al., *Phys. Rev. Lett.* **77** (1996) 2041.
- [4] L1. Balcells et al., *J. Phys.: Condens. Matter.* **10** (1998) 1883.
- [5] Salamon M B and Jaime M, *Rev. Mod. Phys.* **73** (2001) 583.
- [6] Ramirez A P, *J. Phys.: Condens. Matter* **9** (1997) 8171.
- [7] Coey J et al., *Adv. Phys.* **48** (1999) 167.
- [8] Bao-xin Huang et al., *J. Magn. Magn. Mater.* **280** (2004) 176.
- [9] J. H. Park et al., *Phys. Rev. Lett.* **81**, 1953 (1998).
- [10] R. Mahesh et al., *Appl. Phys. Lett.* **68**, 2291 (1996).
- [11] A. Gupta et al., *Phys. Rev. B* **54**, R15629 (1996).
- [12] X. S. Yang et al., *J. Phys. D: Appl. Phys.* **41**, 115009 (2008).
- [13] P. K. Siwach et al., *J. Phys.: Condens. Matter.* **20** (2008) 273201.
- [14] Ramirez A. P. and Subramanian M. A. *Science* **277** (1997) 546.
- [15] Ramirez A. P. et al., *Nature* **387** (1997) 268.
- [16] Kobayashi K. S. et al., *Nature* **395** (1998) 677.
- [17] J. M. D. Coey et al., *Appl. Phys. Lett.* **72** (1998) 734.

Chapter 2. General background

2.1 The Phenomena of Magnetoresistance

Magnetoresistance (MR) refers to the relative change of the electrical resistivity of a material in the magnetic field. MR is generally defined by the equation

$$MR(\%) = \Delta\rho / \rho_0 \times 100 = [\rho_0 - \rho_H / \rho_0] \times 100 \quad (\text{Eq. 2.1})$$

, where ρ_H and ρ_0 are the resistivities at a given temperature in the applied and zero magnetic fields, respectively. MR can be positive or negative depending on the increase or decrease in resistivity, respectively.

A classification, summarized in Fig. 2.1, is based on the distinction familiar in magnetism between *intrinsic* properties such as anisotropy constants which depend only on the crystal structure, composition, and purity, and *extrinsic* properties such as coercivity which depend on the structure with a mesoscopic or microscopic length scale. The extrinsic properties are influenced by critical processing conditions. Those depending on the microscale magnetization distribution may be regarded as micromagnetic MR effects, although the influence of domain structure in the usual sense [1] is usually negligible. Large effects arise when there is a sharp change of magnetization direction from one ferromagnetic region to the next.

The classical positive MR which varies as B^2 is an intrinsic property [2], which has been observed in half-metallic ferromagnets such as

CrO₂ at low temperatures [3]. It is absent in the free electron gas [4], but appears when the Fermi surface is nonspherical. It is anisotropic in the sense that the field must be perpendicular to the current direction to observe the effect.

Anisotropic MR (AMR) is an intrinsic property [5] related to the orbital moment of the atomic charge distribution. It changes sign with the relative orientation of the current and magnetization. The magnitude is generally < 1%.

A third intrinsic effect which has attracted much attention is the colossal MR (CMR) exhibited by ferromagnetic oxides which undergo a metal-insulator transition near their T_c [6]. Typical is La_{0.7}Ca_{0.3}MnO₃, where changes of 10%~90% are observed in large fields found in suitably prepared thin films. CMR effects are normally restricted to a limited range of temperature near T_c , but in compositions with noncollinear ferromagnetic structures they may extend down to the lowest temperatures. CMR is essentially due to the increased ferromagnetic alignment in the applied field, and the great sensitivity of electron localization to magnetic disorder in these oxides, whether directly or via bandwidth or polaron effects [6].

The first of the extrinsic effects was giant MR (GMR) in thin-film multilayers of magnetic metals [7]. Large change of resistance (~10%) are seen in small fields (~100 Oe), sufficient to modify the relative orientation of the ferromagnetic layers. Effects are greater when the current flows perpendicular to the plane of the layers, but to achieve a useful resistance it is necessary to pattern small structures on a micrometer scale. The magnetoresistance here depends on a difference in conductivity in the spin-

up and spin-down channels, and the spin diffusion length in the normal metal must be at least comparable to the spacing of the ferromagnetic regions. Analogous results appear in granular alloy systems where a ferromagnetic metal such as cobalt dispersed in a normal metal such as copper or silver, in which it is insoluble. These systems may be prepared by melt spinning [8,9], by mechanical alloying [10], as granular multilayers [11].

A second type of extrinsic negative MR arises in tunnel spin-valve structures where ferromagnetic layers are separated by thin insulating layers. Typically, these barriers are made of Al_2O_3 about 5 nm thick separating layers of the 3d ferromagnets or their alloys whose relative magnetic orientation can be changed by a small applied field [12], but other oxide barriers and ferromagnetic metals may be used instead, such as SrTiO_3 separating layers of $(\text{La}_{0.7}\text{A}_{0.3})\text{MnO}_3$; A=Ca, Sr [13-16]. The tunneling MR (TMR) may be very large (> 90%) at low temperatures. Layers or granular metals such as cobalt particles embedded in SiO_2 show similar behavior [17].

The LFMR observed in polycrystalline ceramic samples of ferromagnetic manganese perovskites which increases with decreasing particle size is also an extrinsic phenomenon related to alignment of the magnetic moments of adjacent grains. It was clearly described by Hwang *et al.*, [18] who compared polycrystalline ceramics with different grain sizes with single-crystal $(\text{La}_{0.67}\text{Sr}_{0.33})\text{MnO}_3$. Both exhibited colossal magnetoresistance, but only the polycrystalline ceramics showed an additional low-field effect. The conductance at the grain boundary depends on the relative orientation of the magnetization direction in the adjacent grains. Details will be shown in the next section.

2.2. LFMR and spin-dependent scattering

Recently, a large LFMR over a wide temperature range from 4.2 K up to the ferromagnetic order temperature T_c has been discovered for sintered bulk samples and polycrystalline films of perovskite manganites [18, 20]. This extrinsic LFMR has been attributed to the properties of grain boundaries and interpreted in terms of spin-polarized tunneling transport across the magnetic domains or grain boundaries. The LFMR is quite interesting for both fundamental understanding and potential sensor applications of these materials. Apart from high $\Delta R/R_H$ values at low field and over a wide temperature range, chemical stability, adjustable T_c , straightforward synthesis, and low production costs make polycrystalline perovskite materials very competitive in the field of magnetoresistive applications.

Recent work on ferromagnetic manganites has revealed that the LFMR is unambiguously associated with the properties of grain boundaries due to a variety of clear experimental findings. In detail, the observations have been attributed to spin-dependent tunneling through grain boundaries for the following reasons: (1) since the up- and down-spin bands are well separated in $\text{La}_{1-x}\text{D}_x\text{MnO}_3$, the magnetic polarization (saturation moment) is 100% [18]. (2) The LFMR is observed below the ferromagnetic transition temperature. (3) The phenomena are greatly enhanced by the high degree of spin polarization in the low-temperature ferromagnetic regime. The spin-dependent tunneling is seen as follows: The electrons tunnel between two ferromagnetic metals without spin flip (spin is conserved in tunneling). The tunnel current is dependent on the density of states of the metals. The tunnel resistance change can be written as $\Delta R/R = 2PP'/(1+PP')$, where P and P' are the conduction–electron spin polarizations of the two metals [22].

H. Y. Hwang et al., [18] conducted careful studies on the role of grain boundaries through comparing the single crystal and polycrystalline

$\text{La}_{0.67}\text{Sr}_{0.33}\text{MnO}_3$ samples. The single crystal $\text{La}_{0.67}\text{Sr}_{0.33}\text{MnO}_3$ was prepared by floating zone method, whereas polycrystalline $\text{La}_{0.67}\text{Sr}_{0.33}\text{MnO}_3$ samples are by conventional solid-state reaction in air at 1300 and 1700°C. Fig. 2.2 shows temperature dependence of resistivity and magnetization of the samples. Both the single crystal and polycrystalline samples show a sharp ferromagnetic transition at $T_c \sim 365\text{K}$. However, at low temperatures, ρ of the polycrystalline samples is significantly higher than that of the single crystal, as shown in Fig. 2.2. At 5K, a ρ of 35 $\mu\Omega\text{cm}$ is observed polycrystalline sample is about an order of magnitude higher owing to scattering introduced by the grain boundaries. Furthermore, the ρ of the 1300°C sintered sample is almost an order of magnitude larger than the 1700°C sintered sample because of increased scattering that is due to smaller grain size. As shown in Fig. 2.2, the low temperature ρ depends strongly on the microstructure, whereas the magnetization at 0.5 T is virtually identical for the three samples. The effect of the grain boundaries on the LFMR is even more surprising. Fig. 2.3 shows the field-dependent magnetoresistance and magnetization of the samples investigated. For a single crystal there is negligible MR at low temperatures, and with increasing temperature there is increasing negative MR. Correspondingly, the magnetization shows a rapid rise because of magnetic domain rotation at low applied fields, followed by a slow approach toward saturation at higher fields. The magnitude of LFMR increases with decreasing temperature, while the intrinsic MR that has a maximum near the T_c decreases with lowering temperature. This suggests that the MR in the polycrystalline samples is dominated by intergrain effects, with the magnetic field associated with the sharp drop in resistance identical to that associated with magnetic domain rotation. Another important observation, apparent from Fig. 2.3, is that above 0.5 T and for the entire temperature range 5-280K the MR in the polycrystalline samples has the field dependence of type $\sim H^2$ in addition to the obvious dominant linear term in H . They concluded that LFMR in polycrystalline samples is due to

spin-polarized tunneling between misaligned grains.

2.3. LFMR properties in perovskite manganites and spinel ferrites

In this chapter, the crystallographic structure, electronic structure, and LFMR properties of perovskite manganites and spinel ferrites in bulks and films, respectively, are briefly introduced.

2.3.1. LFMR properties of perovskite manganites

2.3.1.1 Crystallographic structure of perovskite manganites

The crystalline structure of the doped manganites is based on ABO_3 perovskite structures with general formula $RE_{1-x}AE_xMnO_3$ as shown in Fig. 2.4. The large sized rare earth (RE) trivalent ions and alkaline earth (AE) divalent ions occupy the A -sites with 12-fold oxygen coordination. The smaller Mn ions in the mixed-valence state Mn^{3+} and Mn^{2+} are located at the centre of an oxygen octahedron, the B -sites with 6-fold coordination. The structure of the manganites is governed by the tolerance factor t , defined as

$$t = \frac{(r_A + r_o)}{\sqrt{2}(r_B + r_o)} \quad (\text{Eq 2.2})$$

, where r_A , r_B , r_o are the atomic radius of A , B , O site atoms, respectively, in the perovskite unit cell. The perovskite structure is stable in the range of 0.89

$< t < 1.02$, and $t = 1$ corresponding to the perfect cubic structure. Generally, t differs from 1 and the manganites have lower symmetry of rhombohedral or orthorhombic structures. Fig. 2.5 shows the structure of doped manganite; rhombohedral and orthorhombic structures. The LSMO, which is studied here, have the rhombohedral structure and also drawn as pseudo-cubic structure.

2.3.1.2 Electronic structure of manganites

The basic building blocks of the manganites are the MnO_6 octahedra. In the cubic environment of the MnO_6 octahedron, hybridization and electrostatic interaction with oxygen $2p$ electrons will create a crystal field for the outer $3d$ electrons in Mn^{3+} . Thus, the five d -orbitals are split by a cubic crystal field into three t_{2g} orbitals and two e_g orbitals. The lower t_{2g} triplet consists of the d_{xy} , d_{yz} , and d_{zx} orbitals and the higher energy e_g doublet consists of the $d_{x^2-y^2}$ and $d_{3z^2-r^2}$ orbitals. The energy splitting between the lowest t_{2g} level and the highest e_g level is ~ 1.5 eV as shown in Fig. 2.6. Due to strong intratomic Hund's coupling, all electrons of Mn^{3+} and Mn^{4+} ions are aligned parallel, leading to $S=2$ and $S=3/2$ (magnetic moments of $4\mu_B$ and $3\mu_B$) for Mn^{3+} and Mn^{4+} ions, respectively, and the corresponding exchange energy is about 2.5 eV, which is larger than the crystal field splitting. All three outer electrons of Mn^{4+} occupy the t_{2g} sites, while the extra electron of Mn^{3+} is situated in one of the e_g levels. The t_{2g} orbitals overlap relatively little with the p -orbitals of nearby oxygen atoms, so that the t_{2g} electrons can be considered as forming a localized core spin ($s = 3/2$). The e_g orbitals on the other hand overlap with the p -orbitals of neighboring oxygen atoms. Although

strongly coupled ferromagnetically to the t_{2g} spin, the e_g electron ($S=1/2$) is more mobile and can hop between different Mn ions. Thus the partial degeneracy of the $3d$ orbitals has been removed by crystal field splitting. The remaining degeneracy is usually broken by the lattice motion. The oxygen ions surrounding the Mn^{3+} ions can slightly readjust their locations, creating an asymmetry between the different directions that effectively removes the degeneracy. This lifting of degeneracy due to the orbital-lattice interaction is named as the Jahn-Teller distortion effect.

2.3.1.3 The LFMR properties of perovskite manganites

The perovskite manganites with a T_c above room temperature as shown in Fig. 2.7, such as $La_{0.7}Sr_{0.3}MnO_3$ (LSMO), showing the LFMR behaviors have attracted a world wide attention. In these manganites intrinsic CMR, which is a gigantic decrease of resistance by the application of an external magnetic field, is observed near the T_c with high applied magnetic fields (> 1 T) [22-24]. Recently, there has been considerable research in order to achieve high MR values with lower magnitude of the applied magnetic fields (< 0.1 T) by taking the advantage of the extrinsic MR effects. [25, 26]. The extrinsic MR effect has been observed in ceramics and polycrystalline films in a wide temperature range in the ferromagnetic region (at temperature much lower than T_c). It is induced by spin-polarized tunneling at the grain boundaries. Grain boundaries, which decouple the neighboring ferromagnetic grains and serve as energy barriers for tunneling, are the key point for the enhanced LFMR effect [27, 28].

Thus many groups have attempted to improve the LFMR effect in manganite-based composites by incorporating a secondary phase, which not only creates additional artificial grain boundaries but further increases the height of the tunneling barriers because of local structural disorder, chemical disorder, spin disorder at the phase boundaries [29-34]. Therefore, recent efforts are being directed to synthesize composite materials consisting of two (or more) different manganites or manganites and polymer/insulator materials which may show large LFMR near room temperatures [35-37, 38-45, 46-48]. Several groups have attempted to enhance LFMR by making and insulating oxide, a hard ferromagnetic material, a polymer, etc.. Bacells et al., [39] and Petrov et al., [40] were the first who reported the LSMO/CeO₂ and LSMO/SrTiO₃ composites and they found enhanced LFMR near the percolative threshold. The LFMR was also found to be enhanced in composites comprising manganites like La_{0.67}Ca_{0.33}MnO₃ (LCMO) and LSMO with secondary phases such as insulators (SiO₂, V₂O₅, ZnO, Al₂O₃, and etc.) [41-45], a hard ferromagnetic material [46], a soft magnetic material [47], polymer materials [48-50], a glass [51], and etc.. But in every case the basic objective is to increase the height of the tunnel barrier between the neighboring ferromagnetic grains. The grain boundaries in polycrystalline manganites mimic the role of the thin insulating layer sandwiched between two ferromagnetic grains, which are magnetically as well as structurally disordered, having disordered Mn spins. In fact, as Mn spin disorder density increases due to second phases, the carrier scattering increases, leading to further enhancement in the resistivity, and the magnetic interaction energy also increases, and hence a higher magnetic field is

needed to suppress them. When a magnetic field is applied, the spin disorder is suppressed, resulting in slightly higher MR, especially above a magnetic field $H < 1$ kOe. Thus the overall positive change in MR at low temperatures is due to the slightly enhanced spin disorder in the intergranular regions, which leads to enhanced spin-polarized tunneling. In interesting study Yao et al., [52] prepared nanocrystalline composites of LCMO-CeO₂ by means of a dispersing particle polymer-network gel method, which leads to both high field (~70% at 50K in 5 T) and LFMR (~16% at 5K in 0.05 T at the percolation threshold of ~35% CeO₂ addition) (Fig. 2.8). They invoked that smaller grain size and good connectivity among neighboring grains because of the dispersing particle polymer-network gel cause enhanced LFMR in the LCMO-CeO₂ nanocomposites. The detailed sintering conditions and LFMR values of LSMO based-composite bulk samples in literatures are summarized in Fig. 2.9

Recently, the LFMR effect has been reported in several manganite composite thin films [53-59], which could be more favorable for device applications. For example, Koster et al., [53] obtained a pronounced LFMR of 25% in 0.5 T at 4.2 K in LSMO columnar films with MgO adding, which are shown in Fig. 2. 10. Aiping C. et al., [54] reported enhanced LFMR value of 17.5% at 40 K and 30% at 154 K in 1 T for epitaxial LSMO-ZnO self assembled vertically aligned nanocomposite thin films which are also shown in Fig. 2. 11.

2.3.2. The LFMR properties of spinel ferrites

2.3.2.1 Crystallographic structure of spinel ferrite

The general chemical formula of ferrites possessing the structure of the spinel is $MeFe_2O_4$ (Me : transition metals, Mn, Fe, Co, Ni, Cu and Zn, or Mg and Cd). The symbol Me can represent a combination of ions which have an average valency of two; in this study Mn^{2+} , Zn^{2+} , Fe^{2+} and Fe^{3+} in MnZn ferrites.

The spinel structure takes its name from the mineral $MgAl_2O_4$, which crystallizes in the cubic system as shown in Fig. 2.12. The smallest cell of the spinel lattice that has cubic symmetry contains eight ‘molecules’ of $MeFe_2O_4$. The relatively large oxygen ions form an FCC lattice. In the cubic close-packed structure two kinds of interstitial sites occur, the tetrahedral and octahedral sites which are surrounded by 4 and 6 oxygen ions, respectively. In the above cubic unit cell, 64 tetrahedral sites and 32 octahedral sites are present, of which only 8 and 16 respectively are occupied by metal ions (called A and B sites respectively). The eight divalent ions were in the eight tetrahedral sites and the sixteen trivalent ions in the sixteen octahedral sites, which are known as a *normal* spinel. The spinels also occur with the 8 divalent ions in eight of the sixteen available octahedral sites, and with the sixteen trivalent ions uniformly distributed over the remaining sites. The eight divalent and the eight trivalent ions are in this case distributed at random over the sixteen octahedral sites. Spinel having an ionic distribution of this nature are called *inverse* spinels.

A completely normal of completely inverse spinel represents

extreme cases. The general cation distribution can be indicated as



, where the ions on tetrahedral sites are given in front of the square brackets and the octahedral ions between the brackets. For a completely random distribution, $x = 1/3$, for a normal spinel $x = 1$ and for an inverse spinel $x = 0$. An interesting aspect, typical of ferrimagnetism, is exhibited by the mixed zinc ferrites in which the ion distribution is:



Since, owing to presence of (non-magnetic) zinc ions, the magnetization of the tetrahedral lattice will be smaller than in the case of the simple ferrite, and since the Fe^{3+} ions have the largest magnetic moment, the saturation magnetization of a mixed ferrite at the 0K would be expected to increase with rising zinc content. Thus the remarkable fact appears that the substitution of magnetic ions in a ferromagnetic substrate by non-magnetic ions can lead to an increase in the saturation magnetization. The Zn^{2+} and Ga^{3+} have a preference for a tetrahedral site. Thus, small concentrations of Zn^{2+} and Ga^{3+} increase the saturation magnetization of simple ferrimagnetic spinels at 0K. Theoretically the saturation magnetic moment should rise linearly with the zinc content and should reach the value of $10 \mu_B$ (μ_B : Bohr magneton) for $x = 1$, when all divalent magnetic ions have been replaced by zinc ions. For small concentrations, the linear rise with the theoretical slope

has been found experimentally [60], as appears from Fig. 2.13. For larger concentrations, however, deviations are found. The magnetic moments of a few remaining Fe^{3+} ions on the A sites are no longer able to align all the moments of the B sites antiparallel to themselves. This is opposed by the negative B - B exchange interaction, which remains unaffected. The most important soft ferrite material is MnZn ferrites due to its saturation magnetization and relatively lower resistivity compared to other spinel ferrites (Fig. 2.14, 2.15) [61, 62].

2.3.2.2 Electronic structure of spinel ferrites

The spinel ferrite has semiconducting properties, but the conduction mechanisms are different and much less fully understood than those of the elemental group IV semiconductors, such as Si and Ge. One of these mechanisms was described by Verwey as the hopping effects [63], and can be controlled by the addition of minor constituents. Resistivity of spinel ferrites decreases with increasing temperature according to the relation

$$\rho = \rho_0 e^{E_\rho/kT} \quad (\text{Eq. 2.3})$$

, where E_ρ represents an activation energy, which according to Verwey is the energy needed to release an electron from the ion for a jump to the neighbouring ion, so giving rise to electrical conductivity. Upon electron jump, a displacement occurs of the ions in the neighborhood of the electron in question. The mean free path is only about 3 Å. It has been pointed out by

Jonker [64] that in these non-impurity (intrinsic) semiconductors the influence of temperature on the concentration of the conduction carriers is relatively small. This means that the temperature influence on the conductivity is only a result of the change in the mobility for the electrons or holes with temperature. Fig. 2.16 from ref. [65] gives the relation between $\log \rho$ and $1/T$ for various ferrites. In most cases a straight line is found in a side temperature range, with a slope corresponding to E_ρ according to the relation of

$$E_\rho = 0.198 \times 10^{-3} \times d(\log \rho) / d(1/T). \quad (\text{Eq. 2.4})$$

The values of E_ρ lie between 0.1 and 0.5 eV. A high E_ρ always goes hand in hand with a high resistivity of the ferrite at RT. In a few cases a change in slope is found in the curve, which points to two parallel conductivity mechanisms with differing activation energies. Similar changes have also been found at the T_c of Mn ferrites, Ni ferrites, and Cu ferrites [66].

For spinel ferrites the resistivity at RT can vary, depending on the chemical composition between about $10^{-2} \Omega\text{cm}$ and higher than $10^{11} \Omega\text{cm}$. It has been known that low resistivities are caused in particular by the simultaneous presence of Fe^{2+} and Fe^{3+} ions on equivalent lattice sites (octahedral sites). For example, Fe_3O_4 at RT has a resistivity of approximately $\sim 10^{-3} \Omega\text{cm}$, and NiFe_2O_4 with some deficiency in iron and sintered in a sufficiently oxidizing atmosphere so that the product contains no Fe^{2+} , can have a resistivity higher than $10^6 \Omega\text{cm}$.

2.3.2.3 The LFMR properties of spinel ferrites

The discovery of the LFMR effect in doped perovskite manganites revolutionized material science and a lot of effort has been carried out (and is still going on) to find materials with improved MR at RT in low magnetic fields. Another promising compound of the LFMR family is the spinel ferrites with comparatively high T_c of < 600 K. However, The LFMR effect in spinel ferrites has been studied on only magnetite (Fe_3O_4) with different forms. In this system, the spin-polarized carriers originating from the half-metallic band structure of magnetite are also believed to affect the transport properties of magnetite, especially the LFMR.

For decades, the MR phenomena in magnetite have been investigated for samples with different crystalline quality [67-70] and preparation methods [71-75]. No LFMR was observed for a single-crystalline magnetite sample [68], as shown in Fig. 2.17, although it is expected to contain spin-polarized carriers. This result implies that the existence of spin-polarized carriers alone is not sufficient for inducing LFMR effect in such magnetic materials. Coey et al., had reported that the LFMR values of magnetite in polycrystalline thin film and compacted powder were 1.7% and 1.2% at RT in 1.5 kOe, respectively. Recent researches effort on magnetite has focused on varying its chemical composition by replacing Fe ions with other transition metal elements for studying the effects on the LFMR properties [76-80]. A number of LFMR results were reported for ternary spinel ferrites $T_x\text{Fe}_{3-x}\text{O}_4$ ($T = \text{Cr}, \text{Mn}, \text{Co}, \text{Ni}, \text{Zn}, \text{etc.}$). Isakawa et al., [76] have prepared epitaxial films of Mn-doped magnetite using pulsed laser deposition technique and confirmed that

as Mn concentration in doped film was increased, carrier concentration became lower, thus indicating potential for field effect transistor or magnetization reversal by spin injection. Valence band studies of Zn-doped Fe_3O_4 films have revealed that the density of states near the Fermi level was reduced that with increasing Zn concentration [81]. These results indicate that such a system could serve as a tunable ferromagnetic semiconductor with a strong electron correlation.

References

- [1] J. F. Gregg et al., *Phys. Rev. Lett.* **77** (1997) 1580.
- [2] A. B. Pippard, “Magnetoresistance” Cambridge Univ. press, Cambridge (1984).
- [3] J. M. D. coey et al., *J. Appl. Phys.* **91** (2002) 8345.
- [4] N. Ashcroft and B. Mermin, “*Solid state physics*” Holt, Rinehart and Winston, New York, (1976).
- [5] T. R. McGuire and R. I. Potter, *IEEE Trans. Magn.* **11** (1975) 1018.
- [6] J. M. D. Coey et al., *Adv. Phys.* **48** (1999) 150.
- [7] M. baibich et al., *Phys. Rev. Lett.* **64** (1988) 2472.
- [8] A. E. Berkowitz et al., *Phys. Rev. Lett.* **68** (1992) 3745.
- [9] J. Q. Xiao et al., *Phys. Rev. Lett.* **64** (1992) 3749.
- [10] A. Fagan et al., *J. Phys.: Condens. Matter.* **7** (1995) 8953.
- [11] B. Rodmacq et al., *J. Magn. Magn. Mater.* **118** (1993) L11.
- [12] T. Miyazaki and N. Tekura, *J. Magn. Magn. Mater.* **139** (1995) L231.
- [13] J. Z. Sun, *Philos. Trans. R. Soc. London Ser. A* **356** (1998) 1693.
- [14] Y. Lu et al., *Phys. Rev. B* **54** (1996) R8357.
- [15] J. Z. Sun et al., *Appl. Phys. Lett.* **69** (1996) 3266.
- [16] M. Viret et al., *Europhys. Lett.* **39**, (1997) 545.
- [17] A. E. Berkowitz et al., *Appl. Phys. Lett.* **73** (1998) 535.

- [18] H. Y. Hwang et al., *Phys. Rev. Lett.* **77** (1996) 2041.
- [19] A. Gupta et al., *Phys. Rev. B* **54** (1996) R15629.
- [20] R. Mahesh et al., *Appl. Phys. Lett.* **68** (1996) 2291.
- [21] J. S. Moodera and L. R. Kinder, *J. Appl. Phys.* **79** (1996) 4724.
- [22] A. Urushibara et al., *Phys. Rev. B* **51** (1995) 14103.
- [23] A. M. Haghiri-Gosnet et al., *J. Phys. D: Appl. Phys.* **36** (2003) R127.
- [24] M. Jain et al., *J. Am. Ceram. Soc.* **91** (2008) 1858.
- [25] J. H. Park et al., *Nature* **392** (1998) 794.
- [26] N. Zhang et al., *Phys. Rev. B* **56**(1997) 8138.
- [27] R. Gross et al., *J. Magn. Magn. Mater.* **211** (2000) 150.
- [28] X. L. Wang et al., *Appl. Phys. Lett.* **73** (1998) 396.
- [29] Aiping Chen et al., *Adv. Funct. Mater.* **21** (2011) 2423.
- [30] Y. M. Kang et al, *Appl. Phys. Lett.* **95** (2009) 052510.
- [31] P. K. Siwach et al., *J. Phys. Condens. Matter* **20** (2008) 273201.
- [32] X. S. Yang et al., *J. Phys. D* **41** (2008) 115009.
- [33] C. S. Xiong et al., *Phys. B* **403** (2008) 3266.
- [34] L. Yan et al., *J. Appl. Phys.* **96** (2004) 1568.
- [35] Huang Y. H. et al., *Appl. Phys. Lett.* **81** (2002) 76.
- [36] Yan X. B. et al., *J. Phys. D: Appl. Phys.* **38** (2005) 3360.
- [37] Pal S. et al., *J. Appl. Phys.* **94** (2003) 3485.

- [38] Shiyakhtin O. A. et al., *J. Appl. Phys.* **91** (2002) 7403.
- [39] Balcells L. I. et al., *Appl. Phys. Lett.* **74** (1999) 4014.
- [40] Petrov D. K. et al., *Appl. Phys. Lett.* **75** (1999) 995.
- [41] Das D. et al., *J. Magn. Magn. Mater.* **238** (2002) 178
- [42] Xia Z. C. et al., *J. Phys. D: Appl. Phys.* **36** (2003) 217
- [43] Das D. et al., *J. Phys. Condens. Matter* **16** (2004) 4089.
- [44] Shilpi K. et al., *J. Phys. D: Appl. Phys.* **38** (2005) 3757.
- [45] A. Gaur et al., *Solid. State Commun.* **139** (2006) 310
- [46] Huang Q. et al., *J. Appl. Phys.* **90** (2001) 2924.
- [47] Yan C. H. et al., *J. Appl. Phys.* **87** (2000) 5588.
- [48] Yan C. H. et al *J. Phys. Condens. Matter* **14** (2002) 9607.
- [49] Huang Y. H et al., *J. Appl. Phys.* **91** (2002) 7733.
- [50] Kumar J. et al., *J. Alloys Compounds* **455** (2008) 289.
- [51] Gupta S. et al., *Appl. Phys. Lett.* **78** (2001) 362.
- [52] Yao L. D. et al., *J. Appl. Phys.* **101** (2007) 063905.
- [53] S. A. Koster et al., *Appl. Phys. Lett.* **81** (2002) 1648.
- [54] Aiping C. et al., *Adv. Funct. Mater.* **21** (2011) 2423.
- [55] Y. M. Kang et al., *J. Appl. Phys.* **105** (2009) 07D711.
- [56] Zhensheng Bi et al., *J. Appl. Phys.* **109** (2011) 054302.
- [57] Margo S. et al., *Adv. Funct. Mater.* **22** (2012) 3591.

- [58] S. Valencia et al., *J. Appl. Phys.* **94** (2003) 2524.
- [59] Yuchun Feng et al., *J. Magn. Magn. Mater.* **322** (2010) 2675.
- [60] Guillaud P. C. et al., *J. Phys. Rad.* **12** (1951) 239.
- [61] Long Wu et al, *J. Phys. D: Appl. Phys.* **13** (1980) 259.
- [62] R. Pauthenet et al., *Compt. R. Ac. Sc. Paris* **230** (1950) 1842.
- [63] E. J. W. Verwey et al., *J. Chem. Phys.* **15** (1947) 181.
- [64] G. h. Jonker to appear in *J. Phys. Chem. Sol.*
- [65] J. Smit and H. P. J. Wijn., “Ferrites” (1965).
- [66] A. P. Komar et al., *Physics* **18** (1954) 45.
- [67] S. B. Ogale, et al., *Phys. Rev. B.* **57** (1988) 7823.
- [68] J. M. D. Coey, et al., *Appl. Phys. Lett.* **72** (1998) 734.
- [69] G. Q. Gong, et al., *Phys. Rev. B* **56** (1997) 5096.
- [70] W. Erenstein, et al., *Phys. Rev. Lett.* **88** (2002) 247204.
- [71] M. Ziese, et al., *Eur. Phys. J. B,* **28** (2002) 415.
- [72] H. Liu et al., *Appl. Phys. Lett.* **83** (2003) 3531.
- [73] S. I. Rybchenko et al., *Phys. Rev. B* **72** (2005) 054424.
- [74] Z. L. Lu et al., *J. Phys. Chem. B* **110** (2006) 23817.
- [75] W. Wang et al., *Phys. Rev. B* **73** (2006) 134412.
- [76] M. Ishikawa et al., *Appl. Phys. Lett* **86** (2005) 222503.
- [77] D. Tripathy et al., *J. Appl. Phys.* **101** (2007) 013904.

- [78] C. Y. Chou et al., *IEEE. Trans. Magn.* **41** (2005) 906.
- [79] C. T. Lie et al., *J. Magn. Magn.* **239** (2002) 160.
- [80] K. J. Kim et al., *J. Appl. Phys.* **104** (2008) 083912.
- [81] J. Takaobushi, *Appl. Phys. Lett.* **89** (2006) 242507.

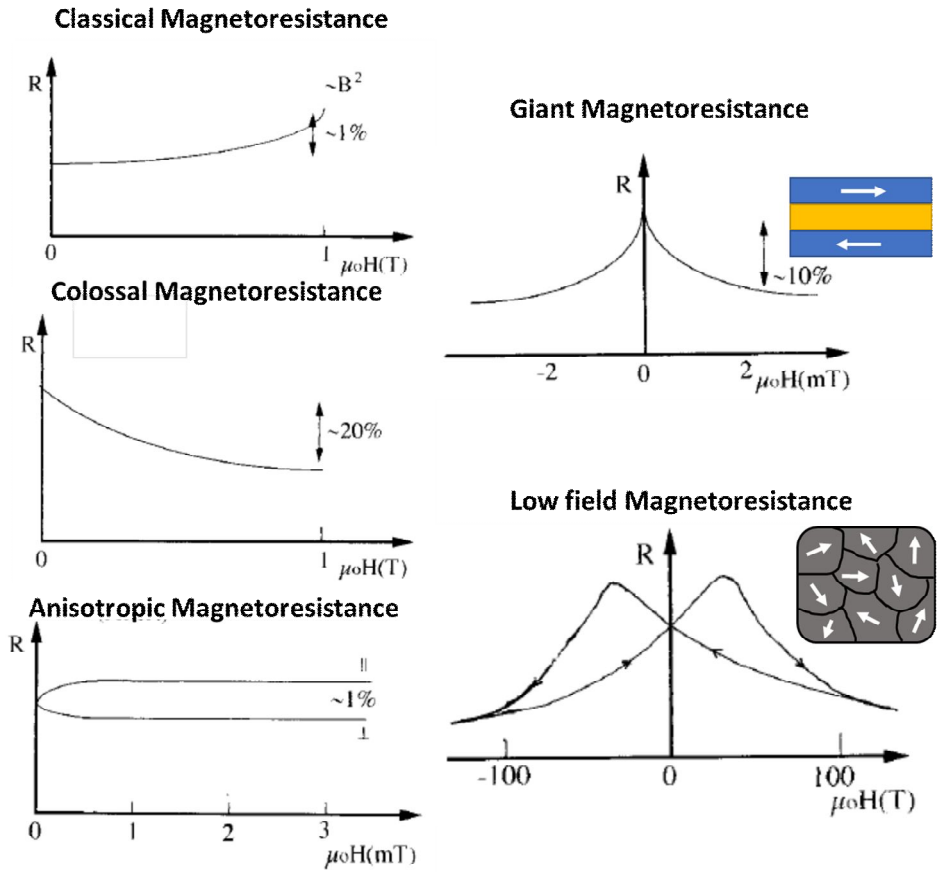


Fig. 2.1. The magnetoresistance family.

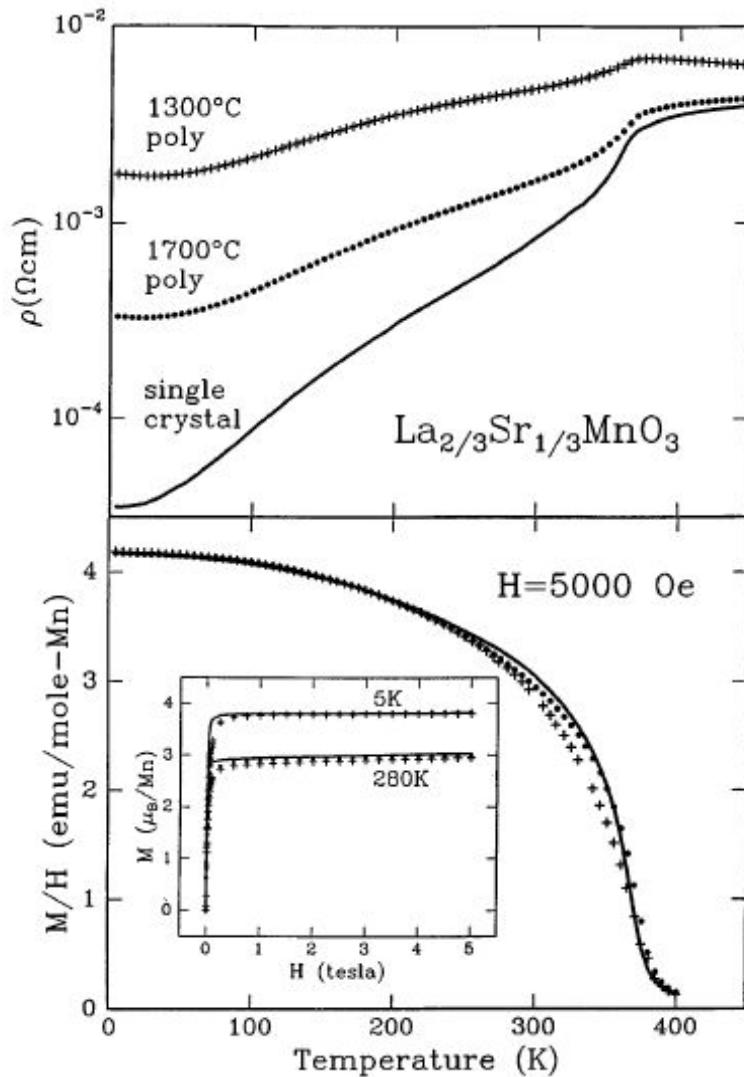


Fig. 2.2. Top panel: $\rho(T)$ of $\text{La}_{2/3}\text{Sr}_{1/3}\text{MnO}_3$ for a single-crystal sample and two polycrystalline samples with final sintering temperatures of 1300 and 1700°C. Bottom panel: the temperature dependence of the magnetization for these three samples at 0.5 T. Inset: the field-dependent magnetization of these three samples at 5 and 280 K (data from ref. [18]).

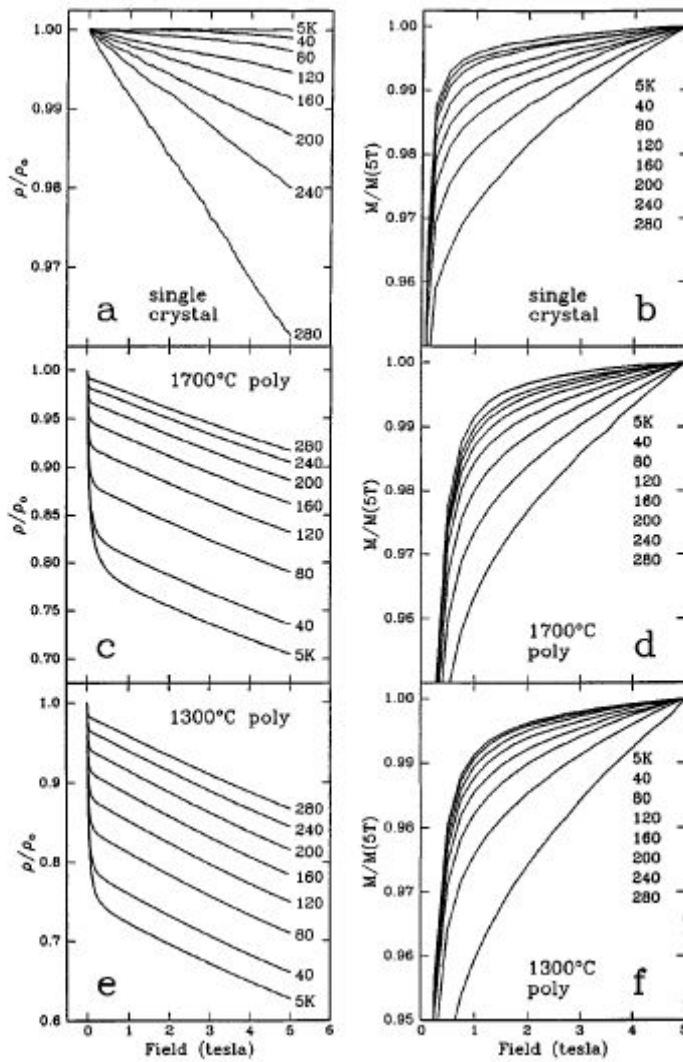


Fig. 2.3. (a), (c), (e) The magnetic field dependence of the normalized resistance at various temperatures from 5 to 280 K. (c), (d), (f) The magnetic field dependence of the magnetization (normalized to the 5 T value) at various temperatures from 5 to 280 K. (data from ref. [18])

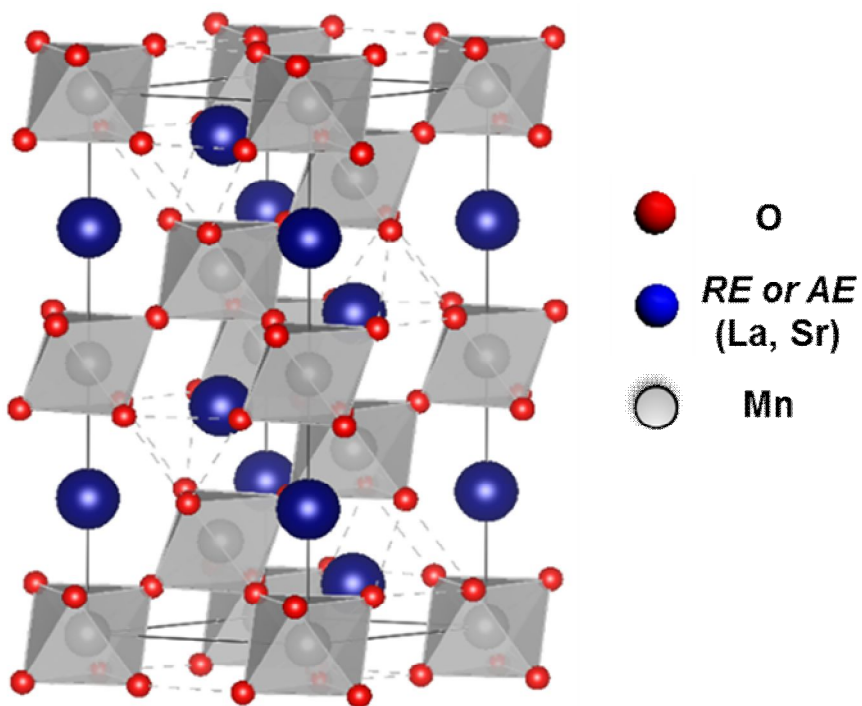


Fig. 2.4. The ideal cubic $RE_{1-x}AE_xMnO_3$ perovskite structure.

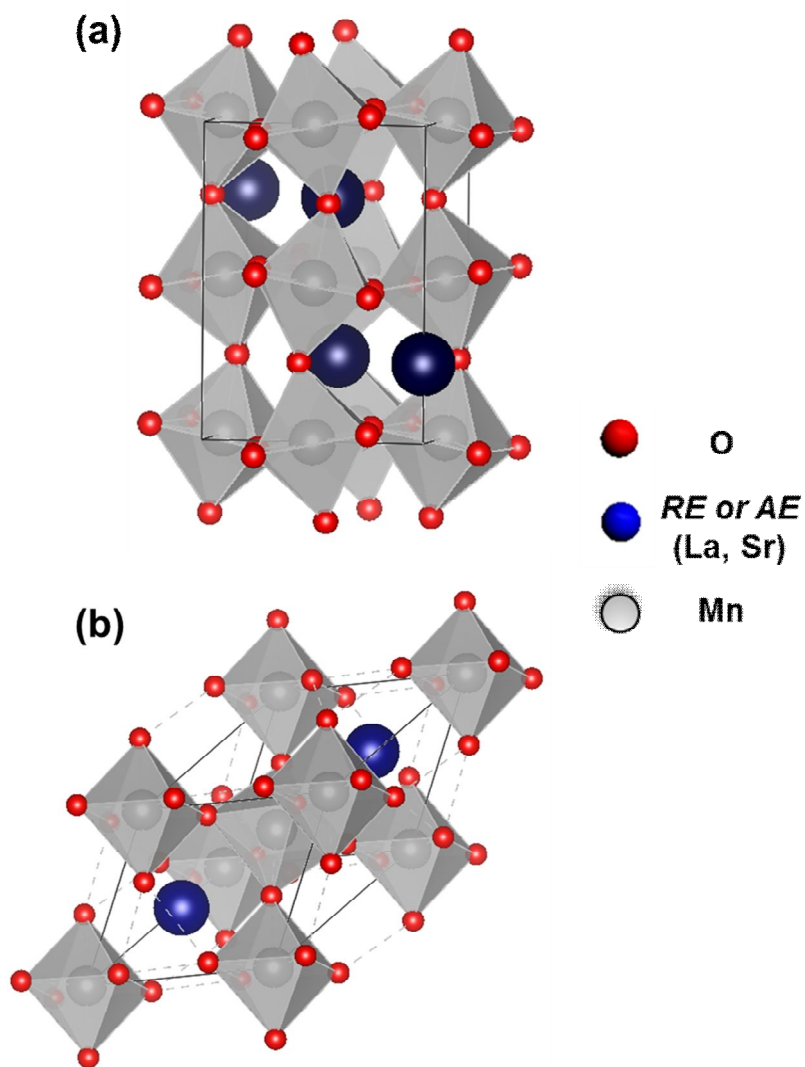


Fig. 2.5. Structure of distorted perovskite mangante: (a) orthorhombic and (b) rhombohedral structures.

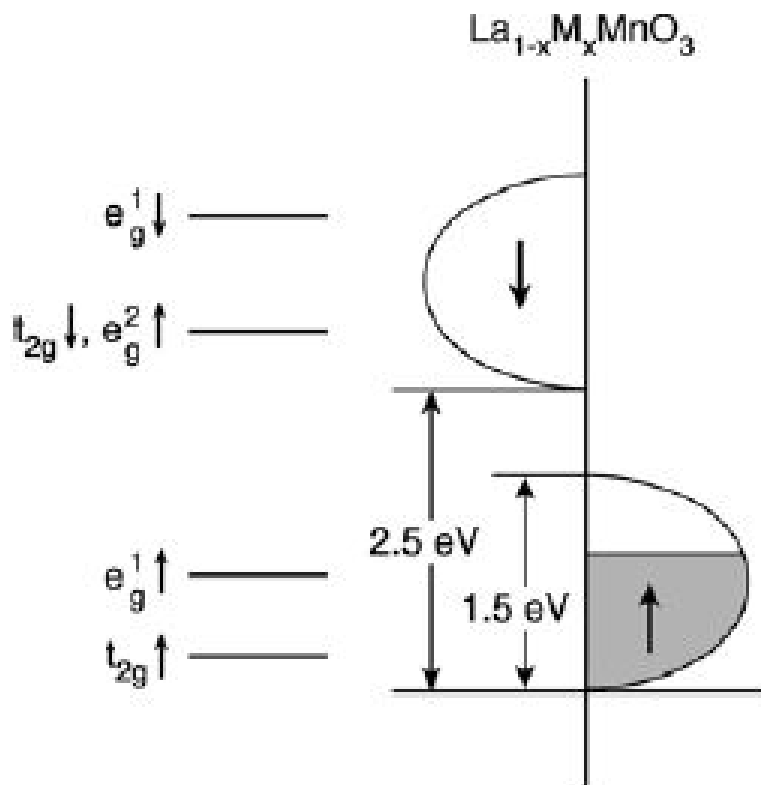


Fig. 2.6 Schematic view of the band structure of ferromagnetic-doped LaMnO_3 . The energies and filling of the bands correspond to $\text{La}_{2/3}\text{Sr}_{1/3}\text{MnO}_3$. The level diagram on left is that of an isolated Mn ion in an octahedral crystal field. (data from ref [23])

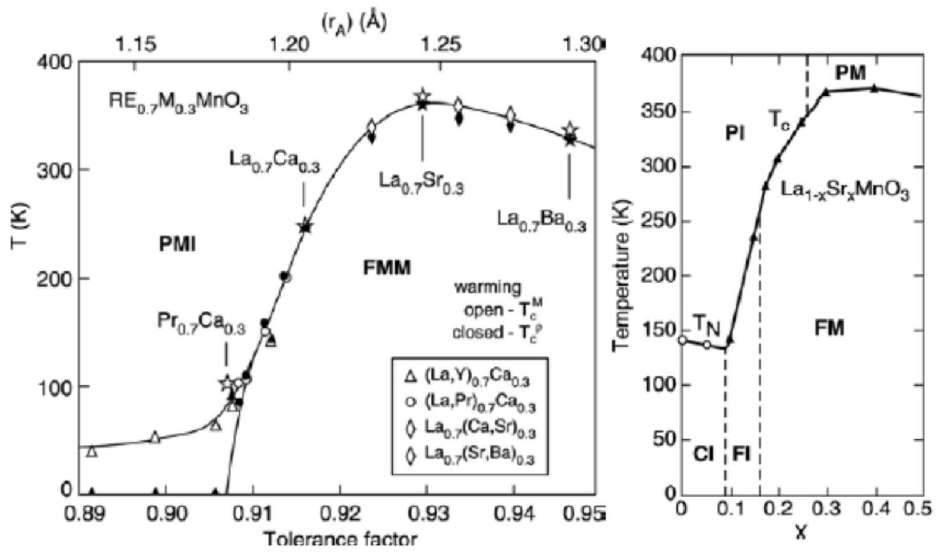


Fig. 2.7. (left) Phase diagram of temperature versus tolerance factor and average radius of cation at A site for the system $RE_{0.7}M_{0.3}MnO_3$. (right) Phase diagram showing transition temperature versus concentration, x , of single crystals of $La_{1-x}Sr_xMnO_3$. (data from [23])

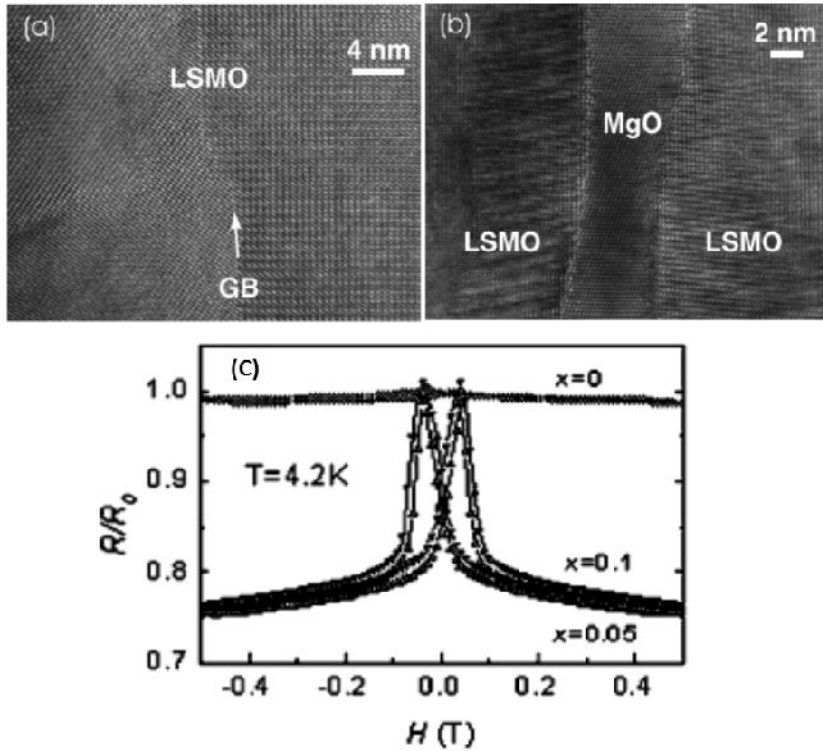


Fig. 2.8. High resolution TEM images for (a) single grain boundary for pure LSMO sample and (b) the MgO located between LSMO grains for 5 mol% MgO added LSMO composite sample, LFMR behaviors of (c) pure LSMO sample and composite sample (5 and 10 mol% MgO added composite samples). (data from ref. [52])

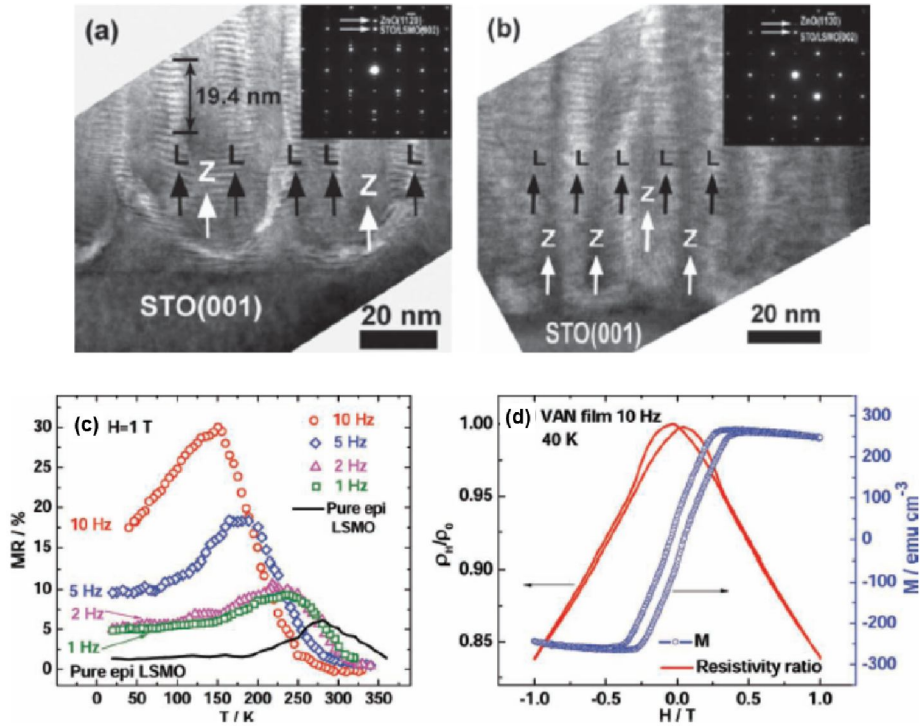


Fig. 2.9. (a) cross-sectional TEM images of the LSMO : ZnO vertical aligned nanocomposite (VAN) film deposited by PLD at 1 Hz. The marked distance is 10 domain periods (19.4 nm) along the vertical interface. “Z” stands for ZnO phase and “L” represents the LSMO phases. (b) TEM image of the 10 Hz VAN film. The insets are the corresponding SAED patterns from the films. (c) MR as a function of temperatures for LSMO : ZnO VAN films deposited at different frequencies. Resistivity ratio ρ_H/ρ_0 and magnetic hysteresis loop of 10 Hz VAN films as a function of magnetic field at a temperature of 40 K. (data from ref. [53])

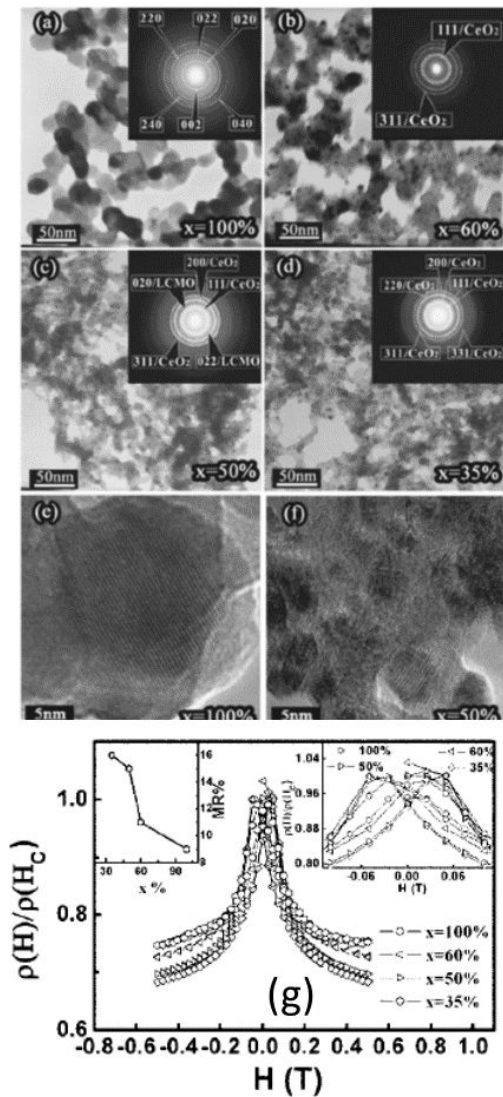


Fig. 2.10. (a)~(d) Electron diffraction patterns form different composites and the corresponding TEM photographs. (e) and (f) HRTEM images of LSMO and 50 mol% CeO₂ adding samples. (g) Low field dependence of resistance $\rho(H)/\rho(H_C)$ of several composites at 5 K. Right inset: the partial enlarged figure, left inset: the variation of MR value with increasing LCMO in a 0.05 T at 5 K.

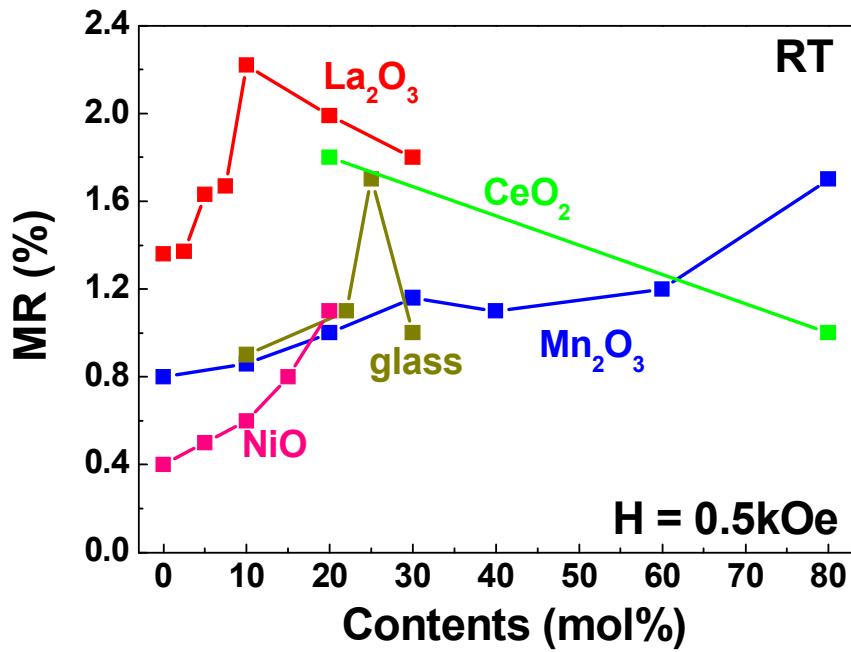


Fig. 2.11. The LFMR values of various LSMO based-composite bulks measured at RT in 0.5 kOe. Additional materials: La₂O₃ (present study), CeO₂ (data from ref. [39]), Mn₂O₃ (data from ref. [30]), glass (data from ref. [50]), NiO (data from ref. [45]).

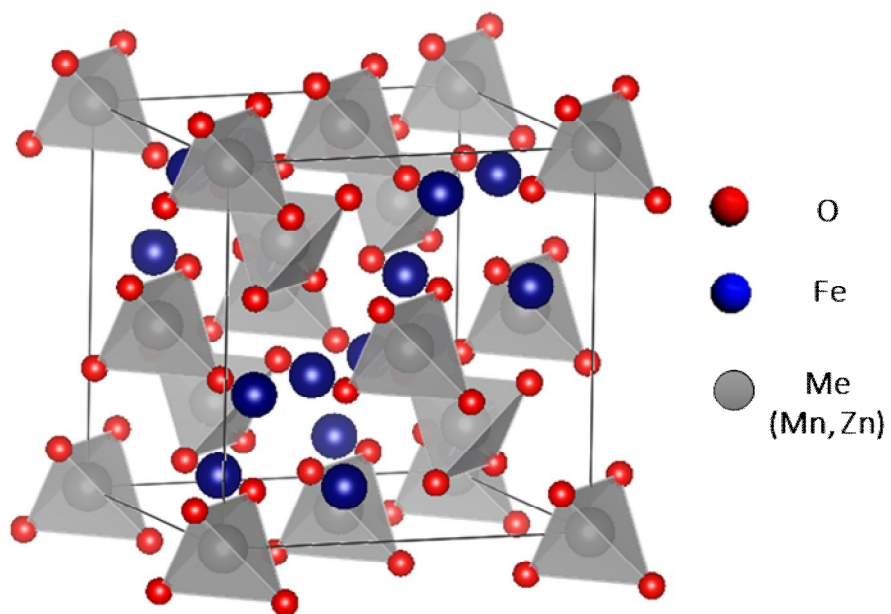


Fig. 2.12. The ideal cubic $MeFe_2O_4$ spinel structure.

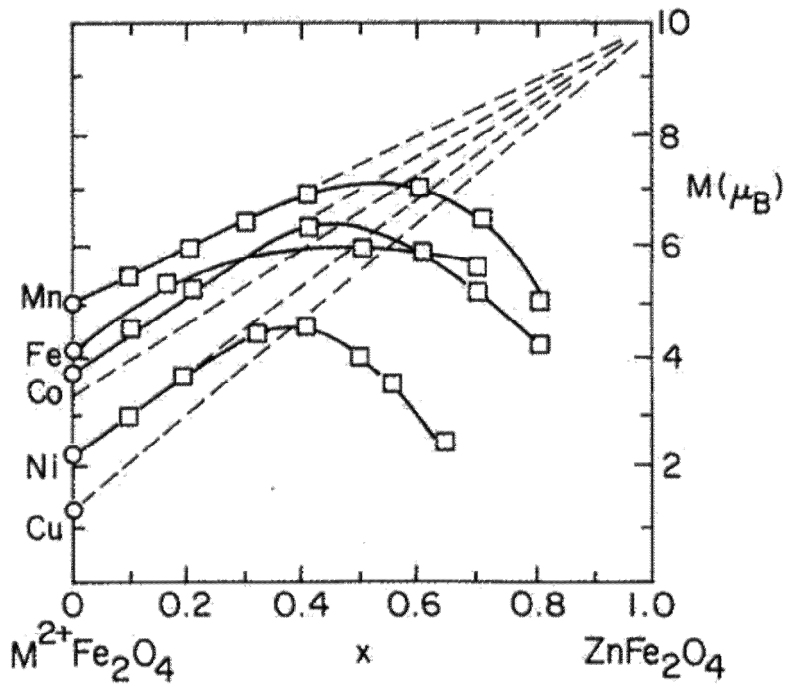


Fig. 2.13. Magnetic moment in transition metal-zinc ferrites as $T = \text{Cu, Ni, Co, Fe, and Mn}$ are substituted for divalent iron. (data from ref. [59])

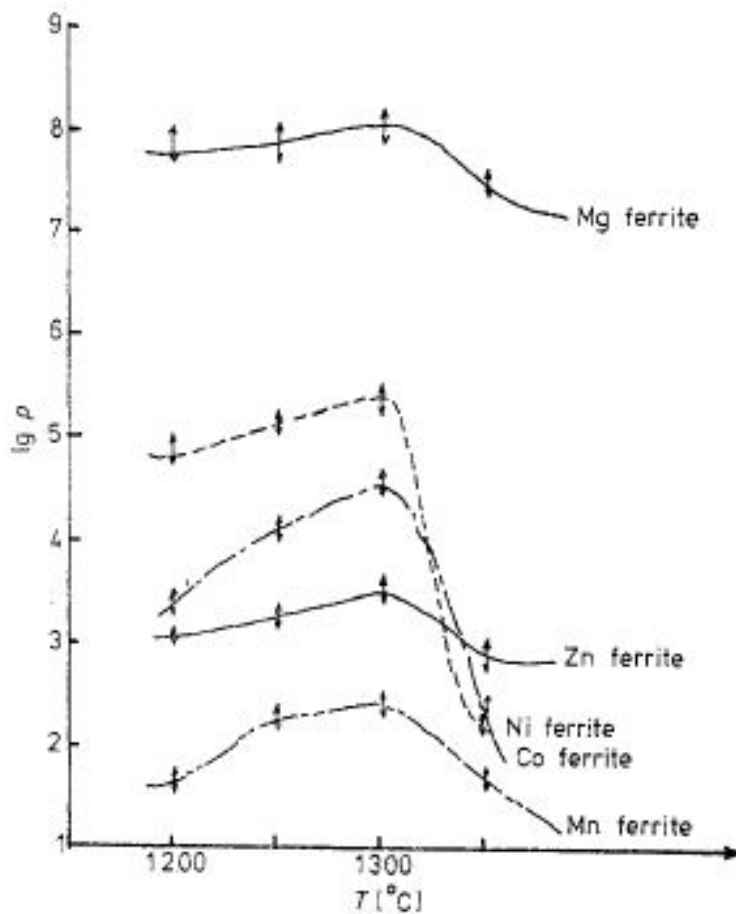


Fig. 2.14. The resistivities of various ferrites with sintering temperature. (data from ref. [60])

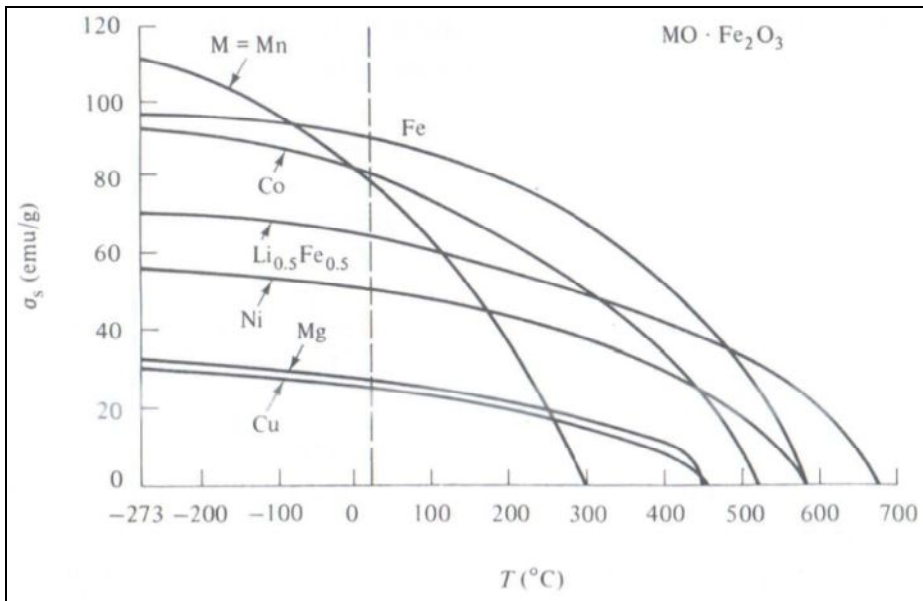


Fig. 2.15. The magnetization versus temperature curves of various ferrites. (data from ref. [61])

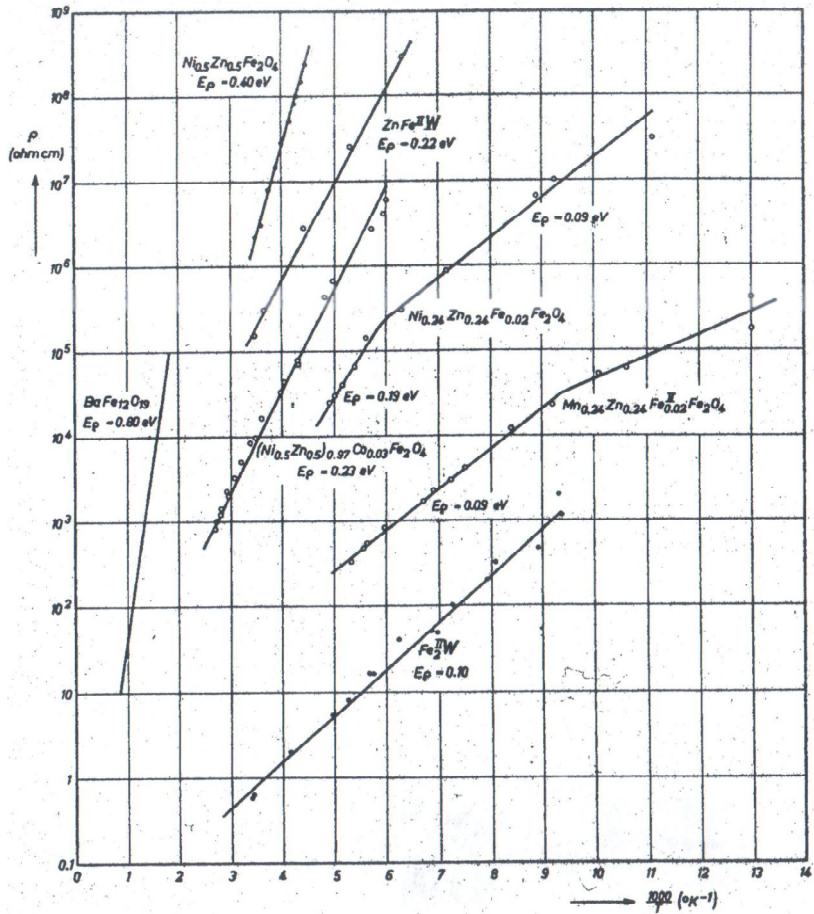


Fig. 2.16. Temperature dependence of *dc* resistivity for several ferrites. (data from ref. [64])

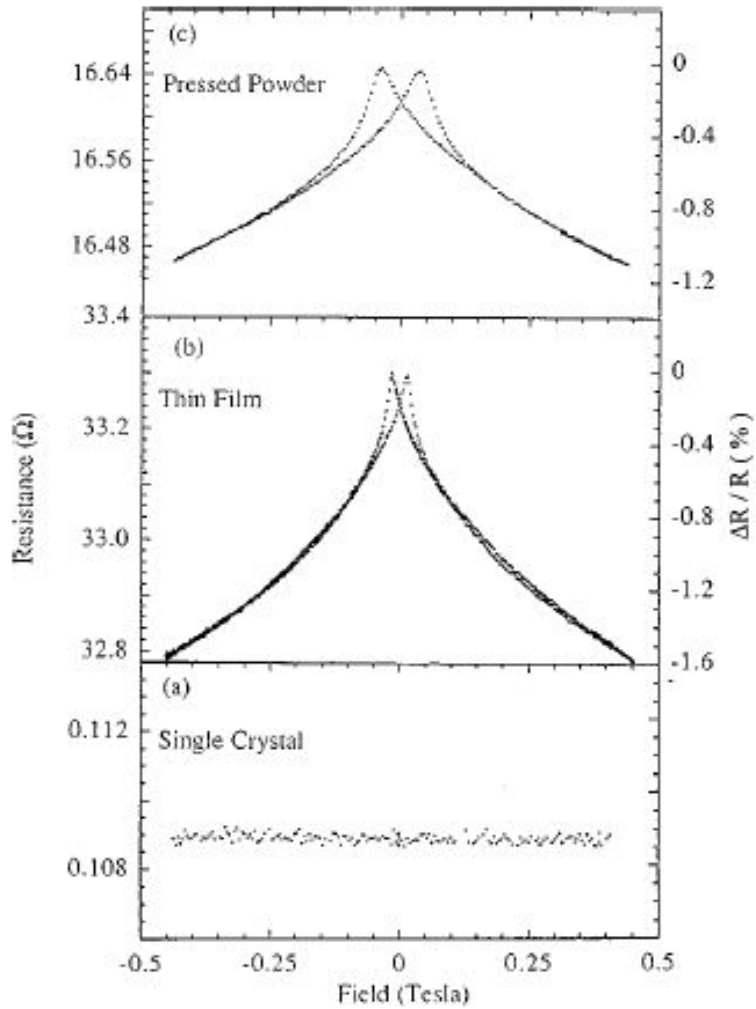


Fig. 2.17. Room temperature MR of (a) single crystal, (b) polycrystalline film, and (c) powder compact. Note the different resistivity scales. (data from ref. [67])

Chapter 3. LSMO-La₂O₃ composites

3.1. Introduction

Since LFMR is applicable to magnetic devices, many groups have attempted to improve the LFMR effect by making a composite of manganites with second phases such as insulators [1-9], metals [10-11], polymers [12-13], and other manganites [14-16]. The second phases usually obstruct the magnetic spin alignment near the grain boundary of the manganite. The improvement of LFMR in the perovskite manganite-oxide composites is normally accompanied by a significant increase in their electrical resistivities by several orders of magnitude higher than that of pure polycrystalline manganite and an abrupt decrease in T_C . To avoid such a serious degradation both in T_C and electrical conductivity, we have tried to select the second phases chemically compatible with LSMO. Referring to the La₂O₃-Mn₂O₃ phase diagram reported by J. A. M. van Roosmalen *et al.* [17], one can see that both Mn₂O₃ (or Mn₃O₄) and La₂O₃ are chemically compatible with LaMnO_{3+d} solid solution phases. For the LSMO-manganese oxide composites, we reported a successful achievement of the highest LFMR value of 1.7% at 500 Oe with the maximum dMR/dH value of 28.3 %kOe⁻¹ at 300 K without a significant variation in T_C and resistivity [18]. In this study, La₂O₃ was selected as an alternative second phase chemically compatible with LSMO. We here report that it is possible to obtain a high LFMR effect from the LSMO-La₂O₃ composite at room temperature as well.

3.2. Experimental

Samples were prepared by using the conventional solid-state reaction. The nominal composition of samples was $(1-x)\text{LSMO}-x\text{La}_2\text{O}_3$ ($x = 0, 0.025, 0.05, 0.075, 0.1, 0.2, 0.3$). The precursor materials were Mn_2O_3 , La_2O_3 , and SrCO_3 powders with all 99.9% purity. The precursors were weighed and ball-milled in ethyl alcohol using ZrO_2 balls for 24 h. The ball-milled slurry was dried and calcined twice at 1100°C for 8 h in air. As-calcined powder were uniaxially pressed into pellets with diameter of 10 mm, and then followed by cold isostatic pressing ($\sim 2 \text{ toncm}^{-2}$). The pellets were sintered at 1400°C for 8 h in air with a heating rate of $5^\circ\text{C}/\text{min}$. High resolution X-ray diffraction (XRD, BRUKER D8 ADVANCE) with θ - 2θ scan using $\text{Cu-K}\alpha$ radiation ($\lambda = 1.54 \text{ \AA}$) and scanning electron microscopy (SEM, JEOL JSM-6360) were performed for phase and microstructure analysis, respectively. Temperature and field dependencies of magnetism were measurement with a superconducting quantum interference device (SQUID) magnetometer (MPMS XL5, Quantum Design). The M - T curves were measured with a field-cooled warming procedure under the applied field of 100 Oe. Measurements of LFMR properties were performed using the standard four probe method within the SQUID magnetometer. Both the electrical current and magnetic field were applied along the long dimension of samples. The Curie temperatures of samples were determined by the maximum point of $|dM/dT|$ in the M versus T curves.

3.3. Results and discussion

Fig. 3.1 shows the powder XRD patterns of pure LSMO and (1-x) LSMO - xLa₂O₃ (x= 0.025, 0.05, 0.075, 0.1, 0.2, and 0.3) composite samples. As can be seen in Fig. 3.1, the relative peak intensity of La₂O₃ is gradually increased with increasing La₂O₃ mole fraction and other second phases are unobservable, representing that LSMO and La₂O₃ phases are chemically compatible. Referring to the La₂O₃-Mn₂O₃ binary phase diagram [17], LaMnO₃ is expected to react with La₂O₃ to form the La_{1+d}MnO₃-type solid solution at the sintering temperature of 1400°C. However, the formation of (La_{0.7+d},Sr_{0.3})MnO₃ type solid solution was hardly detectable in our composite samples. In Fig. 1, it is observed that a small peak of La₂O₃ exists even in the LS-L1 sample having 2.5 mol% La₂O₃. In addition, no peak shift in the LSMO phase was detectable in the LSMO-La₂O₃ composite samples, implying that the cell parameters of the LSMO phase were unaltered after forming the composites. Therefore, it can be suggested that the solubility limit *d* of La³⁺ in (La_{0.7+d},Sr_{0.3})MnO₃ is very small.

The SEM micrographs of pure LSMO and LSMO-La₂O₃ composite samples are shown in Fig. 2. The LSMO and La₂O₃ phases in composites are clearly observed as dark and bright contrasts, respectively. From the SEM micrographs, it is obvious that the La₂O₃ particles are randomly distributed at the LSMO grain boundary up to 10 mol% La₂O₃. Interestingly, however, composites containing 20 and 30 mol% La₂O₃ resulted in a non-uniform microstructure including large agglomerated La₂O₃ grains as shown in low magnification micrographs of Fig. 3.2 (g) and (h).

Fig. 3.3 shows the variation in the average grain size of LSMO grains as a function of La₂O₃ content for all samples, where the average LSMO grain size was analyzed by an image analyzer. It is shown that while the average grain size of LSMO is almost linearly decreased from 2.5 to 1.6 μm with increasing the amount of La₂O₃ up to 10 mol% La₂O₃, it is slightly decreased to 1.4 μm with further increasing the amount of La₂O₃ up to 30 mol%.

The temperature dependency of the magnetization for all samples is shown in Fig. 3.4. One can see that the effect of La₂O₃ addition on the paramagnetic–ferromagnetic transition temperature is insignificant. The T_C values of all samples are listed in Table 1. The T_C values of the composite samples are slightly depressed into the region of 355~358 K compared with that of pure LSMO (362 K), which might be caused by the formation of La_{0.7+d}Sr_{0.3}MnO₃ solid solution with a very limited d value. These results are quite different from the additive effect of perovskite manganite-oxide composites [1, 2, 6-9, 14]. The ferromagnetic ordering of LSMO is usually weakened by the addition of a secondary phase because of its chemical reaction with LSMO resulting in the magnetic dilution [9]. Like the LSMO-manganese composites [18], however, the ferromagnetic ordering of the LSMO phase is insignificantly affected by the addition of La₂O₃ since LSMO is chemically compatible with La₂O₃.

The LFMR values of samples are represented in Fig. 3.5 (a) and (b). The LFMR values at 100 and 300 K were evaluated using the equations of $MR(\%) = (R_H - R_{H=1500Oe})/R_{H=1500Oe} \times 100\%$ and $(R_H - R_{H=500Oe})/R_{H=500Oe} \times 100\%$, respectively. The magnetotransport properties of all samples

measured in this study are summarized in Table 3.1. The resistivity and LFMR values in Table 3.1 were plotted as a function of La_2O_3 content in Fig. 3.5 (c) and (d). First of all, as shown in Fig. 3.5 (c) and (d), while the resistivity values of the LSMO- La_2O_3 composites at the temperatures of 100 and 300 K slightly increase with increasing x from 0 to 7.5 mol%, an order of magnitude increase in resistivity occurs at $x = 10$ mol%, and then it slightly increases with increasing x further up to 30 mol%. This behavior can be understood as the following. The resistivity increase less than three times up to 7.5 mol% addition implies that a metallic percolation path between LSMO grains might not be seriously blocked by the insulating La_2O_3 grains. The abrupt resistivity increase from 7.5 to 10 mol% addition suggests that an effective cross-section of the metallic percolation path is reduced to one tenth, which might be due to more homogeneous distribution of La_2O_3 grains in Fig. 3.2 (e) compared with that in Fig. 3.2 (d). The resistivity increase from 10 to 30 mol% La_2O_3 addition is unexpectedly small, which is obviously attributed to a non-uniform distribution of La_2O_3 grains observed for 20 and 30 mol% additions as shown in Fig. 3.2 (g) and (h), where large agglomerated La_2O_3 particles are found. One can see that the microstructures of Fig. 3.2 (e) and (f) are almost identical except large agglomerated La_2O_3 grains shown in Fig. 3.2 (g) (low magnification micrograph for the same 20 mol% addition with Fig. 3.2 (f)), implying that an additional block of the metallic percolation path is simply due to large agglomerated La_2O_3 grains. If we assume that La_2O_3 particles were not agglomerated, the percolation path would be blocked much more effectively, leading to higher resistivity. Therefore, unexpectedly small increase in resistivity is attributable to the

non-uniform microstructures for 20 and 30 mol% La_2O_3 additions.

On the other hand, the LFMR values at 100 K in 1500 Oe and 300 K in 500 Oe are also represented as a function of the La_2O_3 content in Fig. 3.5 (c) and (d). While the LFMR value at 300K in 500 Oe is monotonously increased from 1.36 to 1.67% with increasing x from 0 to 7.5 mol% La_2O_3 addition, it is abruptly increased to 2.22% for $x = 10$ mol%. Further increase in x from 10 to 30 mol% results in a linear decrease to 1.8%. Hence, the maximum LFMR value of 2.22% at 300 K in 500 Oe can be achieved from the LS-L4 composite of $x = 0.1$. Different from the behavior of the LFMR values in Fig. 3.5 (c) and (d), the maximum dMR/dH values of samples in Table 1 are unaltered up to $x = 2.5$ mol%, significantly increased for the composition region of $x = 2.5$ –7.5 mol%, and then slightly increased up to $x = 30$ mol%. Previous literature [2, 5, 18, 19] reported that the maximum LFMR values of the manganite composites were achievable near a metallic percolation threshold, where their resistivity values were drastically increased (normally over $10^2 \Omega\text{cm}$). However, the maximum LFMR values at 100 and 300 K shown in Fig 3.5 (c) and (d) occur at low resistivity level ($< 1 \Omega\text{cm}$) far below the metallic percolation threshold (see Table 3.1), implying that the maximum LFMR value of the composite with 10 mol% La_2O_3 is irrelevant to metallic percolation threshold. Instead, this peculiar behavior must be closely related to the microstructure variation as described above.

The $R(H) / R(H=0)$ ratios of LSMO and LS-L4 samples, measured at 100 and 300K, versus the applied field up to 1 T are represented in Fig. 3.6. A highly resistive grain boundary provides both the tunneling barrier

and magnetic decoupling of grains. Below the magnetic field of 1 kOe, the MR value abruptly increases with increasing field, which is related to the LFMR effect. At larger fields ($H > 2$ kOe), the MR value almost linearly increases with increasing field. The fast resistivity drop in low field is attributed to the magnetic domain alignment. Much slower and linear resistivity drop in high field is due to a forced spin alignment in spin-disordered region near LSMO grain boundary [20]. Thus, two major factors affecting the MR value include the grain boundary areal density and the degree of a disordered region near the grain boundary. In comparison with pure LSMO, the composite samples surely have higher grain boundary areal density because of reduction in average grain size (see Fig. 3.2) and narrower disordered region near LSMO grain boundary due to the existence of La_2O_3 chemically compatible with LSMO. Therefore, high grain boundary areal density and sharpening of a disordered region near LSMO grain boundary are believed responsible for the enhanced LFMR values of the composite samples. This result is also consistent with that of LSMO-manganite oxide composites of our previous report [18]

3.4. Conclusions

The LSMO- La_2O_3 composites were turned out to have excellent LFMR effects at room temperature. The maximum LFMR value of 2.22% at 300 K in 500 Oe could be achieved from the composite sample of 10 mol% La_2O_3 addition. Remarkably improved LFMR properties of the LSMO - La_2O_3 composites in comparison with pure LSMO are attributable to

sharpening of disordered LSMO grain boundary region acting as more effective spin-dependent scattering centers. Consequently, the LSMO–La₂O₃ composite is very promising alternative for the MR device application. However, since the La₂O₃ phase is very hygroscopic, the LSMO–La₂O₃ composite can be seriously damaged when it is exposed to humidity in air, and hence surface must be required for a real application.

References

- [1] Anurag Gaur, G.D. Varma, *J. Alloys Compd.* **453** (2008) 423.
- [2] D. K. Petrov, *Appl. Phys. Lett.* **75** (1999) 995.
- [3] O. A. Shlyakhtin, *J. Appl. Phys.* **91** (2002) 7403.
- [4] A. Gaur and G. D. Varma, *Cryst. Res. Technol.* **42** (2007) 164.
- [5] L.I. Balcells, *Appl. Phys. Lett.* **74** (1999) 4014.
- [6] Anurag Gaur, G.D. Varma, *Solid. State Commun.* **139** (2006) 310.
- [7] V. Moshinyaga et al., *Nat. Mater.* **2** (2003) 247.
- [8] Chun-Hua yan et al., *J. Appl. Phys.* **87** (2000) 5588.
- [9] Shilpi Karmakar et al., *J. Phys. D: Appl. Phys.* **38** (2005) 3757.
- [10] Caoshui Xionga et al., *J. Alloys compd.* **479** (2009) 357.
- [11] P.T. Phonga et al., *J. Alloys compd.* **484** (2009) 12.
- [12] Yun-Hui Huang et al., *J. Appl. Phys.* **91** (2002) 7733.
- [13] Jitendra Kumar et al., *J. Alloys compd.* **455** (2008) 289.
- [14] P. Kameli et al., *J. Alloys compd.* **463** (2008) 18.
- [15] J.-M. Liu et al., *Appl. Phys. Lett.* **78** (2001) 1110.
- [16] Chun-Hua Yan et al., *J. Appl. Phys.* **91** (2002) 7406.
- [17] J. A. M. van Roosmalen et al., *J. Solid State Chem.* **114** (1995) 516.
- [18] Young-Min Kang et al., *Appl. Phys. Lett.* **95** (2009) 052510.

[19] L. E. Hueso et al., *J. Appl. Phys.* **89** (2001) 1746.

[20] Ll. Balcells et al., *Phy. Rev. B* **58** (1998) R14697.

Table 3.1. Sample identifications (IDs) and properties of LSMO and LSMO - La_2O_3 composites: sample resistivity (ρ), MR at 100 and 300 K and $(d\text{MR}/dH)_{\text{max}}$ at 300 K.

Sample ID	LSMO	LS-L1	LS-L2	LS-L3	LS-L4	LS-L5	LS-L6
x (mol %)	0	2.5	5	7.5	10	20	30
T_C (K)	362	356	358	356	355	358	356
MR (%) at 100K	17.34	18.35	18.90	19.77	22.40	22.30	22.34
MR (%) at 300K	1.33	1.35	1.56	1.60	2.22	2.02	1.80
$\rho_{100\text{K}}$ ($\Omega\cdot\text{cm}$)	0.0039	0.0118	0.0120	0.0122	0.130	0.180	0.181
$\rho_{300\text{K}}$ ($\Omega\cdot\text{cm}$)	0.0124	0.0309	0.0294	0.0320	0.328	0.342	0.348
$d\text{MR}/dH$ ($\%/k\text{Oe}^{-1}$)	1.10	1.11	2.17	3.10	3.21	3.40	3.98

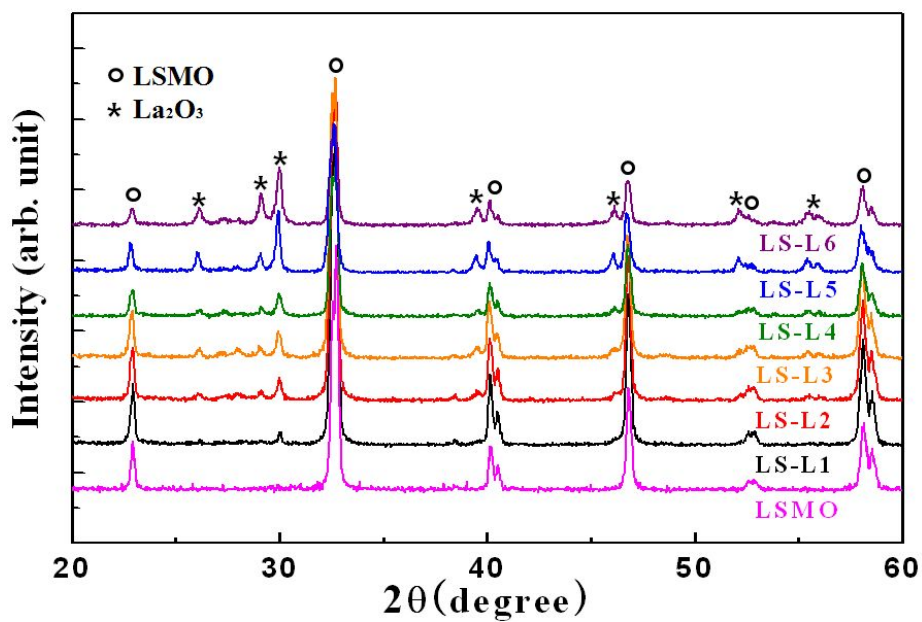


Fig. 3.1. XRD patterns of pure LSMO and LSMO-La₂O₃ composites.

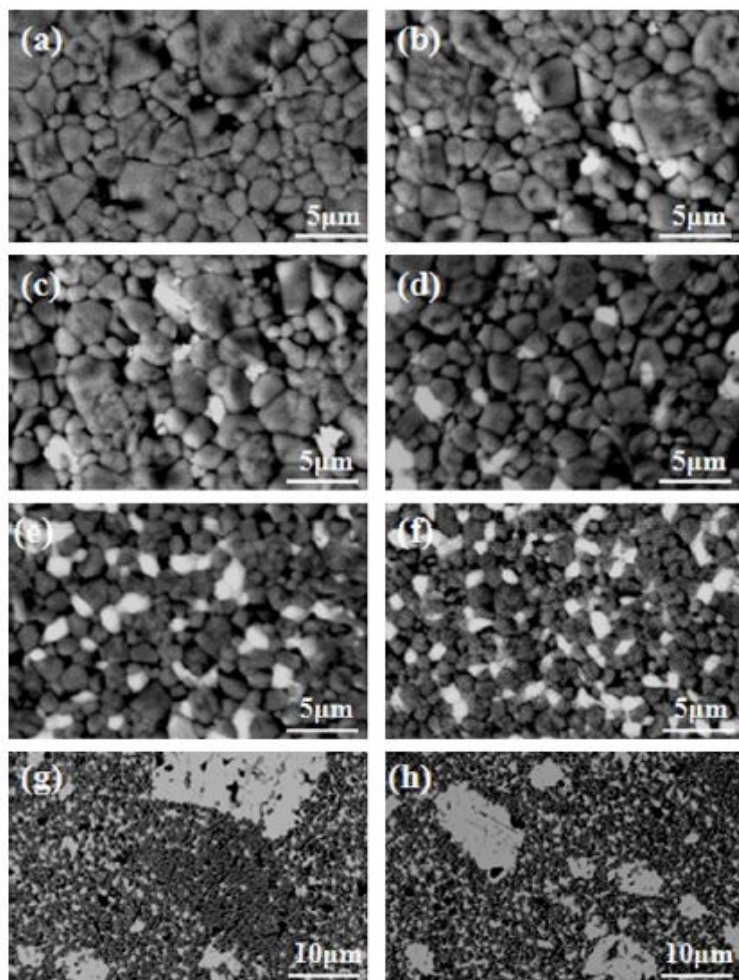


Fig. 3.2. SEM back-scattered electron images of samples: (a) LSMO, (b) LS-L1, (c) LS-L2, (d) LS-L3 (e) LS-L4, and (f) LS-L5. Low magnification micrographs are for the samples of (g) LS-L5 and (h) LS-L6.

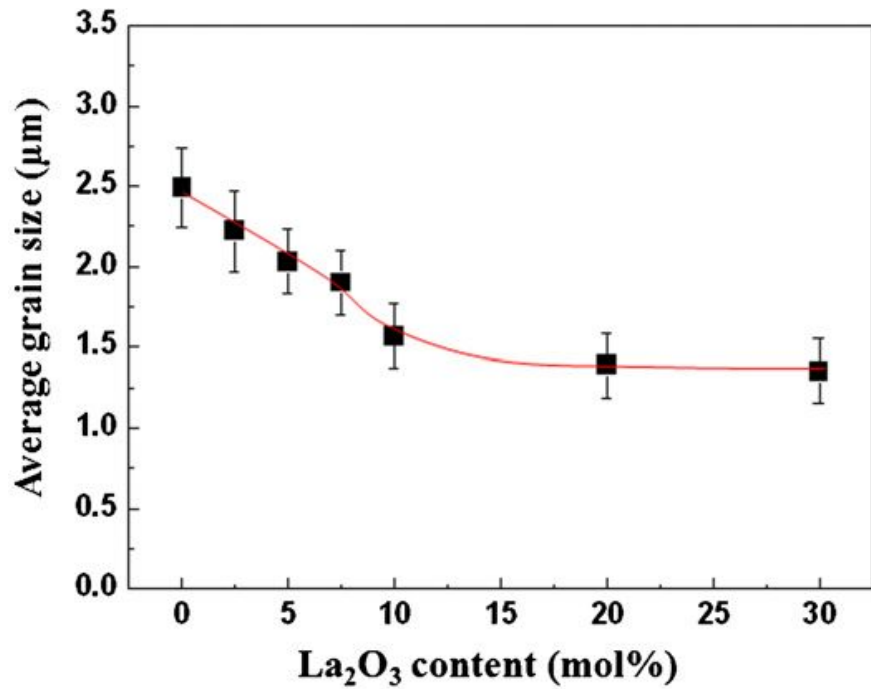


Fig. 3.3. The average LSMO grain size of samples as a function of the La_2O_3 contents.

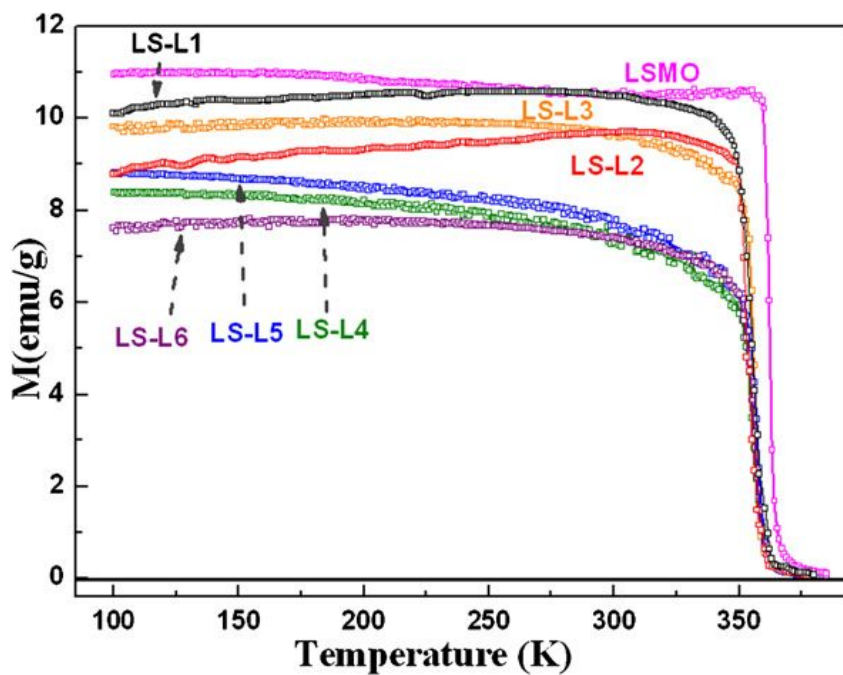


Fig. 3.4. Temperature dependence of magnetization for samples. The M - T curves were measured with field-cooled warming procedure under the applied field of 100 Oe.

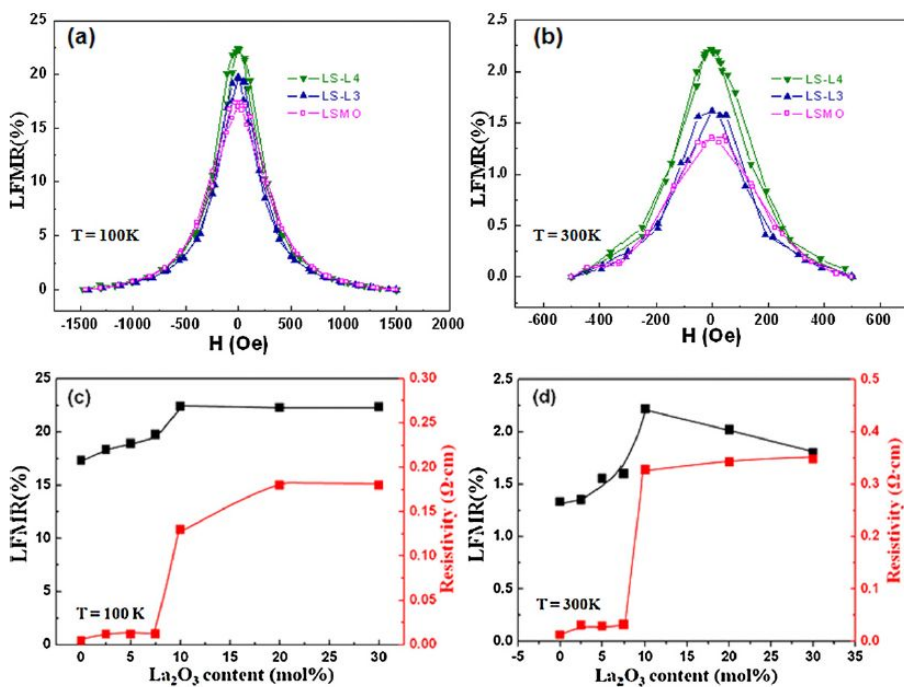


Fig. 3.5. The LFM R behaviors of samples measured at (a) 100 K and (b) 300 K. The electrical resistivity and LFM R values of samples are plotted as a function of the La₂O₃ content at (c) 100 K in 1500 Oe and (d) 300 K in 500 Oe.

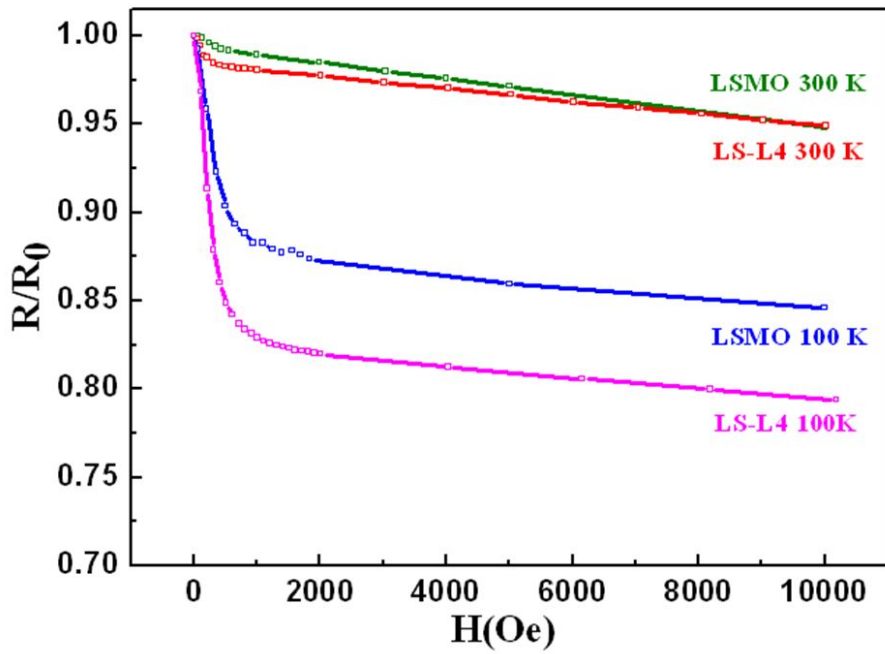


Fig. 3.6. The $R(H) / R(H=0)$ ratios of LSMO and LS-L4 samples, measured at 100 and 300 K, versus the applied field up to 1 T.

Chapter 4. LSMO-manganese oxide composite prepared by liquid phase sintering

4.1. Introduction

We have recently reported that the second phases like Mn_2O_3 (or Mn_3O_4) [1], chemically compatible with LSMO [2], were very effective for avoiding such a serious degradation both in T_C and electrical conductivity. As a new approach to improve the LFMR effect of LSMO, in this study, we tried to modify the LSMO grain boundaries by forming the eutectic structure between LSMO and manganese oxide via liquid phase sintering at the temperature above the eutectic temperature of 1430°C in air [1].

4.2. Experimental

The precursor materials of La_2O_3 , SrCO_3 , and Mn_2O_3 powders with all 99.9% purity were weighed to have the nominal compositions of $(1-x)\text{LSMO}-x\text{Mn}_2\text{O}_3$ ($x = 0, 0.1, 0.2, 0.3, 0.4, \text{ and } 0.8$), and ball-milled in ethyl alcohol using ZrO_2 balls for 24 h. The ball-milled slurry was dried and calcined twice at 1100°C for 8 h in air. As-calcined powder were uniaxially pressed into pellets with the diameter of 10 mm, and then consolidated by cold isostatic pressing ($\sim 2 \text{ ton cm}^{-2}$). The pellets were sintered at 1450°C for 1 h in air. Referring to the La_2O_3 - Mn_2O_3 phase diagram [2], we selected 1450°C for liquid phase sintering since the eutectic temperature between LSMO and Mn_3O_4 is reported to be 1430°C in air. In addition, according to the La_2O_3 - Mn_2O_3 phase diagram [2], at 1450°C in air, while the sample with the

nominal composition of $x = 0$ is pure LSMO phase, LSMO and liquid phase are equilibrium phases for the samples with the nominal compositions of $x = 0.1 - 0.4$, and Mn_3O_4 and liquid phase are equilibrium phases for the sample with that of $x = 0.8$. Therefore, at 1450°C in air, while LSMO is expected to be sintered by the solid state reaction, all composite samples are expected to be densified by liquid phase sintering. Further, the eutectic structures are expected to be formed from liquid phases during furnace cooling to room temperature.

Powder X-ray diffraction (XRD, BRUKER D8 ADVANCE) using $\text{Cu-K}\alpha$ radiation ($\lambda = 1.54 \text{ \AA}$) and scanning electron microscopy (SEM, JEOL JSM-6360) were performed for the analyses of phases and microstructures, respectively. For the SEM observations, all composite samples were polished and then thermally etched at 1300°C for 1 h in air. The microstructures were also analyzed by transmission electron microscopy (TEM) (JEOL JEM-3000F, JEM-2100F). Temperature dependency of magnetization (M) was measured with a superconducting quantum interference device (SQUID) magnetometer (MPMS XL5, Quantum Design). The M - T curves were measured with a field-cooled warming procedure under the applied field of 100 Oe. The Curie temperatures of samples were determined by the maximum $|dM/dT|$ point of the M - T curves. Measurements of LFMR were performed using the standard four probe method within the SQUID magnetometer.

4.3. Results and discussion

Fig. 4.1 shows the powder XRD patterns of pure LSMO and

composite samples with the nominal compositions of $(1-x)$ LSMO – x Mn₂O₃ ($x = 0.1, 0.2, 0.3, 0.4,$ and 0.8). The sample IDs for various nominal compositions are defined in Table. I. As can be seen in Fig. 4.1, the relative peak intensity of tetragonal (*T*)-Mn₃O₄ is gradually increased with increasing Mn₂O₃ mole fraction. According to the La₂O₃-Mn₂O₃ binary phase diagram [2], manganese oxide shows three different phases, cubic (*C*)-Mn₂O₃ transforms to *T*-Mn₃O₄ at 880°C, then transforms to *C*-Mn₃O₄ at 1160°C in air. However, the LSM4 and LSM5 samples, where *T*-Mn₃O₄ is the major phase, show that the small peaks of the *C*-Mn₂O₃ phase are detected while composite samples except LSM4 and LSM5 commonly exhibit the *T*-Mn₃O₄ phase. The same results were also observed in the La_{0.7}Sr_{0.3}Mn_{1+d}O₃ - manganese oxide composites with the same nominal compositions prepared by the solid state reaction in our previous study [1].

The SEM micrographs of pure LSMO and composite samples are shown in Fig. 4.2. While the micrograph in Fig. 4.2(a) is the surface image of as-sintered LSMO sample, the micrographs in Fig. 4.2(b)-(f) are the images of thermally etched surfaces of composite samples. Referring to the XRD data, the grains of bright and dark contrast regions for composite samples can be designated as the LSMO and manganese oxide phases, respectively. It can also be seen that the average grain size of LSMO decreases with increasing the amount of manganese oxide in the composite samples. These microstructures seem to be somewhat similar to those of our previous study on the same composites prepared by the solid state sintering [1] in that the dark contrast region is increased with increasing the amount of manganese oxide. However, we can see that detailed microstructures in Fig. 4.2 are quite different from those in ref. [1]. At first, compared with pure LSMO sample

sintered at 1300°C for 8 h in air in ref. [16], the pure LSMO sample sintered at 1450°C for 1 h in air in Fig. 4.2 (a) shows much higher porosity, which is attributed to the overfiring effect at too high sintering temperature. Next, unlike the typical microstructures of composite samples by the solid state sintering in ref. [1], all composite samples in Fig. 4.2 (b)-(f) show characteristic microstructures formed by liquid phase sintering. Two different types of LSMO grains of bright contrast are observed in Fig. 4.2 (b)-(f); One is relatively large faceted grains connected to each other and the other is relatively small round-shaped grains surrounded by the dark contrast phase region. On the other hand, Fig. 4.2 (f) shows relatively large faceted Mn_3O_4 grains of less dark contrast and relatively small round-shaped LSMO grains. In all composite samples, irregular shaped dark contrast regions are composed of many striped Mn_3O_4 grains. Therefore, we suggest that the striped Mn_3O_4 grains and round-shaped LSMO grains might be solidified from the eutectic liquid phase during the furnace-cooling process, while faceted LSMO and Mn_3O_4 grains existed as the pro-eutectic solid phases compatible with liquid phases during liquid phase sintering.

To further analyze the microstructure of the composite sample, we performed TEM analyses on the LSM3 sample as shown in Fig. 4.3. To identify the LSMO and Mn_3O_4 phases, scanning transmission electron microscopes (STEM)-energy dispersive spectrometer (EDS) elemental mapping was also performed as shown in Fig. 4.3 (a) and (b). From these data, the LSMO and Mn_3O_4 phase regions are clearly observed. Fig. 4.3 (c) shows the bright-field TEM image of the LSM3 sample, where a small LSMO phase surrounded by the Mn_3O_4 phase is shown, representing that a eutectic liquid phase might be solidified into two phases of a LSMO and Mn_3O_4 during

furnace-cooling to room temperature. Selected area diffraction (SAD) patterns of A and B areas are shown in the inset of Fig. 4.3 (c), indicating that each Mn_3O_4 phases are arranged by twin relationship. To further analyze the LSMO and Mn_3O_4 phases, HR-TEM analyses were carried out as shown in Fig.4.3 (d). The areas of A and C (or B and D) were confirmed to the same orientation by FFT patterns, relatively, which also supports the twin relationship in Fig. 4.3 (c).

The resistivity curves of samples are shown in Fig. 4.4. Although the average grain size of LSMO significantly decreases with increasing the amount of insulating manganese oxide (Fig. 4.2), the LSM1, LSM2, LSM3, and LSM4 samples still have lower resistivity than pure LSMO sample, implying that the LSMO phase of composite samples possess much lower resistivity value compared with pure LSMO. Interestingly, although conductive LSMO grains seem to be disconnected by insulating manganese oxide grain in Fig. 4.2 (e), this sample shows lower resistivity than pure LSMO sample. The reason is the following. The LSMO phase grown from the eutectic liquid phase is believed not to be a round particle but an elongated rod. These rods connect between themselves or between pro-eutectic faceted LSMO grains. On the other hands, the LSM5 sample shows the abrupt increase in resistivity since the conducting path of the LSMO phase is seriously blocked by the manganese oxide phase.

The temperature dependency of magnetization for all samples is shown in Fig. 4.5. The T_C values of the composite samples (359~368 K) are almost unchanged compared with that of pure LSMO (368K), which might be caused by the formation of $\text{La}_{0.7+d}\text{Sr}_{0.3}\text{MnO}_3$ solid solution with a very limited d value. These results are quite different from perovskite manganite-oxide

composites which show significantly depressed T_C values. The ferromagnetic ordering of LSMO is usually weakened by the addition of a secondary phase because of its chemical reaction with LSMO resulting in the magnetic dilution [3]. Like our previous results [1], however, the ferromagnetic ordering of the LSMO phase is insignificantly affected by the addition of manganese oxide since LSMO is chemically compatible with manganese oxide.

The LFMR behaviors of samples are represented in Fig. 4.6. The properties of all samples are summarized in Table 4.I. In comparison with our previous data for the LSMO and LSMO-manganese oxide composite samples prepared by solid state reaction, all composite samples, prepared by liquid phase sintering, show improved LFMR values. While the LFMR values are unchanged with increasing x from 0 to 0.2, it is abruptly increased to 1.28% from the composite sample with $x = 0.3$. The highest LFMR value of 1.3% could be obtained from the LSM5 sample among all composite samples. The MR peaks commonly become sharp, and thus the $(dMR/dH)_{\max}$ values monotonously increase as listed in the Table I. Similar to LFMR variation, the $(dMR/dH)_{\max}$ values are slightly increased with increasing x from 0 to 0.2, it is abruptly increased from 0.2 to 0.3, and slightly increased from 0.3 to 0.8. In comparison with pure LSMO, the composite samples surely have higher grain boundary areal density because of reduction in average grain size (see Fig. 4.2) and narrower disordered region near LSMO grain boundary due to the existence of manganese oxide chemically compatible with LSMO. Therefore, high grain boundary areal density and sharpening of a disordered region near LSMO grain boundary are believed to be responsible for the enhanced LFMR values of the composite samples. Further improved LFMR properties of these composite samples are attributed to an increase in the effective spin scattering

center at the grain boundaries.

4.4. Conclusions

The LSMO-manganese oxide composites prepared by liquid phase sintering at 1450°C for 1 h in air were turned out to have excellent LFMR effects at room temperature compared with those of the same composites prepared by a solid state reaction. The maximum LFMR value of 1.28% with $(dMR/dH)_{\max}$ value of 21.1 %/kOe at 290 K in 500 Oe could be achieved from the composite sample of 30 mol% Mn₂O₃ addition. These results are attributable to sharpening of disordered LSMO grain boundary region acting as more effective spin-dependent scattering centers by forming a characteristic LSMO-manganese eutectic structure.

References

- [1] Young-Min Kang et al., *Appl. Phys. Lett.* **95** (2009) 052510.
- [2] J. A. M. van Roosmalen et al., *J. Solid State Chem.* **114** (1995) 516.
- [3] Chun-Hua yan et al., *J. Appl. Phys.* **87** (2000) 5588.

Table 4. 1. Sample identifications (IDs) and properties of the LSMO and LSMO-manganese oxide composite samples. Mn mole fraction, $f_{\text{Mn}} = \text{Mn}/(\text{La}+\text{Sr}+\text{Mn})$ in the total precursor powders, sample resistivity (ρ) at 290 K, MR at 290 K in 500 Oe and $(d\text{MR}/dH)_{\text{max}}$ at 290 K.

Property	Sample IDs					
	LSMO	LSM1	LSM2	LSM3	LSM4	LSM5
f_{Mn}	0.5 ($x = 0$)	0.55 ($x = 0.1$)	0.6 ($x = 0.2$)	0.65 ($x = 0.3$)	0.7 ($x = 0.4$)	0.9 ($x = 0.8$)
ρ (Ωcm)	0.084	0.010	0.041	0.071	0.075	25.834
T_c (K)	368.4	359.4	368.4	365.6	360.2	364.4
MR (%)	1.07	1.06	1.06	1.28	1.27	1.30
$d\text{MR}/dH$ (% kOe^{-1})	7.1	8.3	9.2	21.1	25.4	27.8

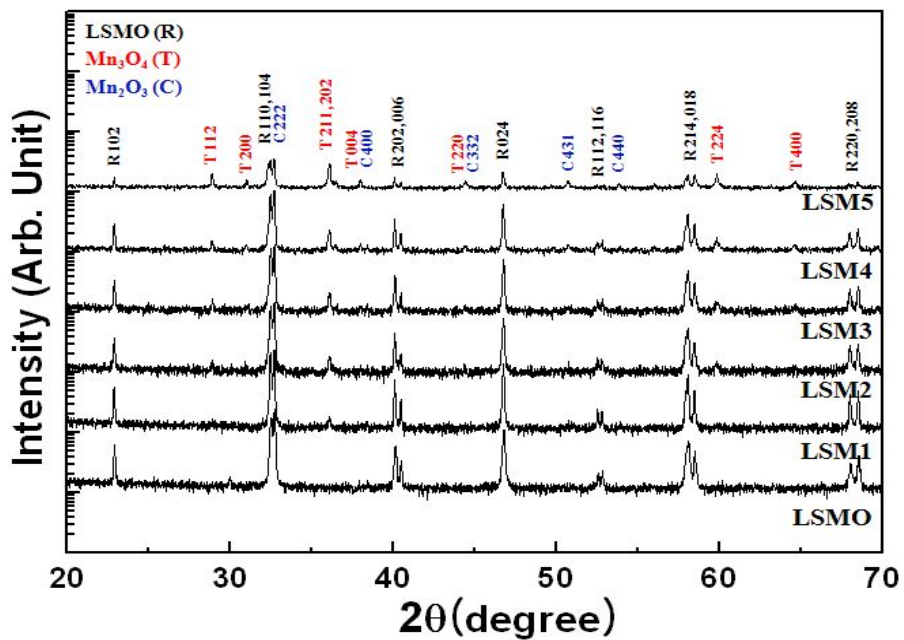


Fig. 4.1. XRD patterns of pure LSMO and LSMO-manganese oxide composites sintered at 1450°C for 1 h in air.

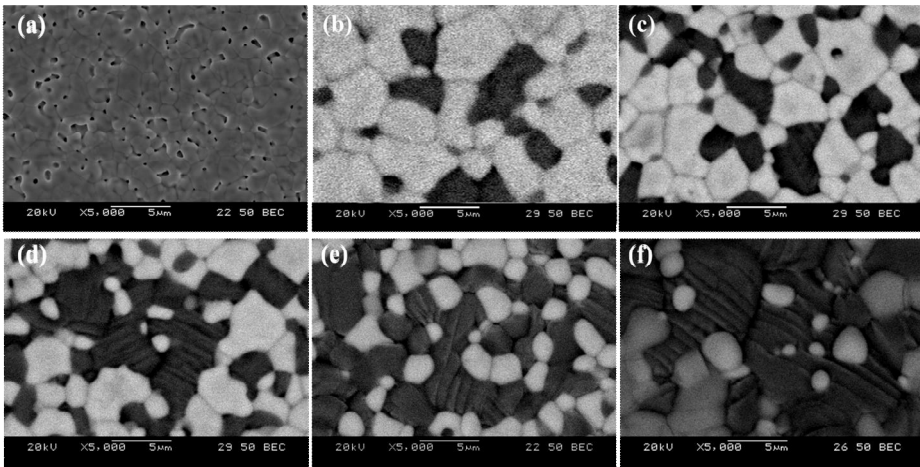


Fig. 4.2. SEM back-scattered electron images of (a) LSMO, (b) LSM1, (c) LSM2, (d) LSM3, (e) LSM4, and (f) LSM5.

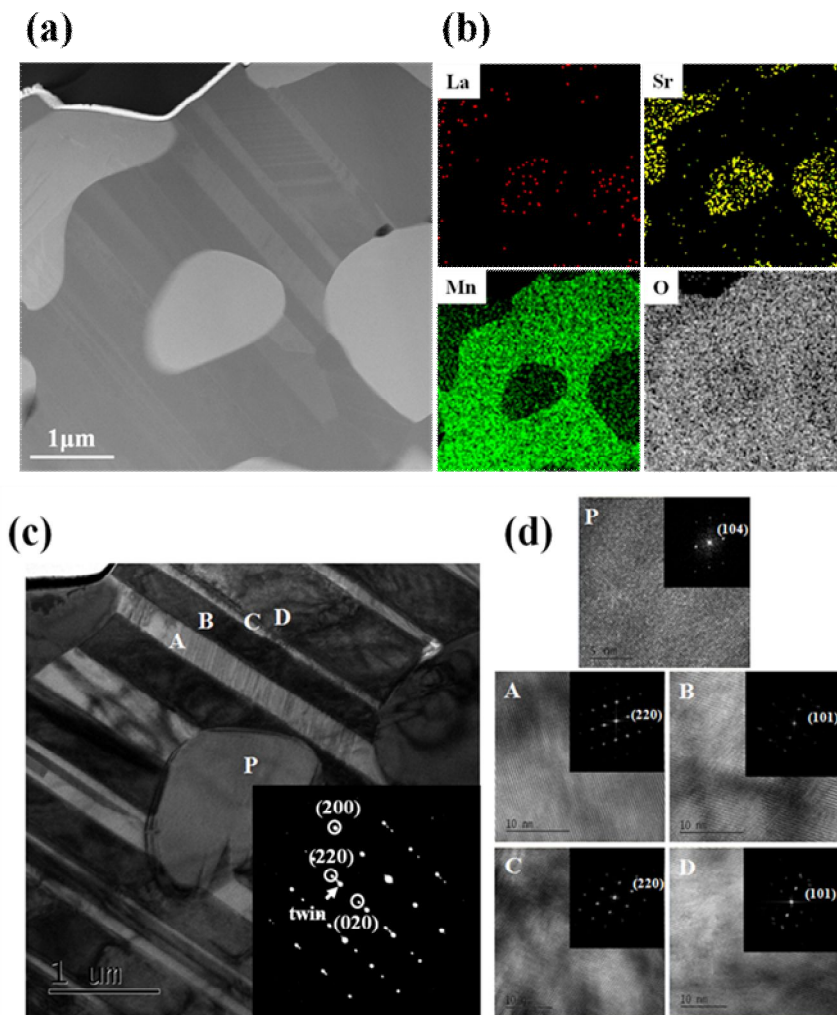


Fig. 4.3. (a) Z-contrast STEM image of the LSM3 sample and (b) the La, Sr, Mn, and O spectral images. (c) Cross-sectional TEM images of the LSM3 sample. Inset is SAD patterns of A and B areas (d) HR-TEM images of the LSMO (marked by P) and Mn_3O_4 phases (marked by A, B, C and D). Insets are FFT patterns of A, B, C and D areas in (c).

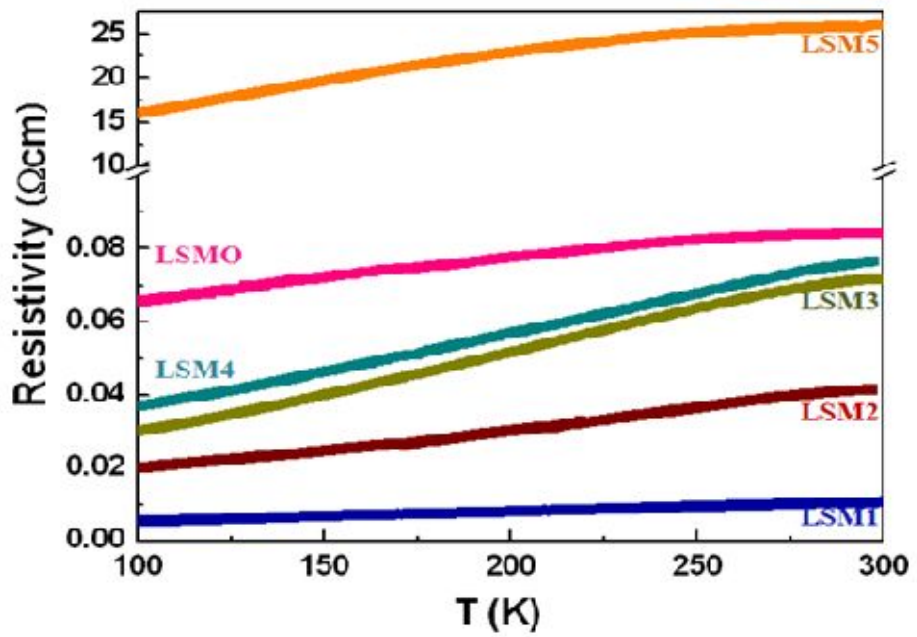


Fig. 4.4. The ρ - T curves for LSMO and LSMO-manganese oxide composite samples.

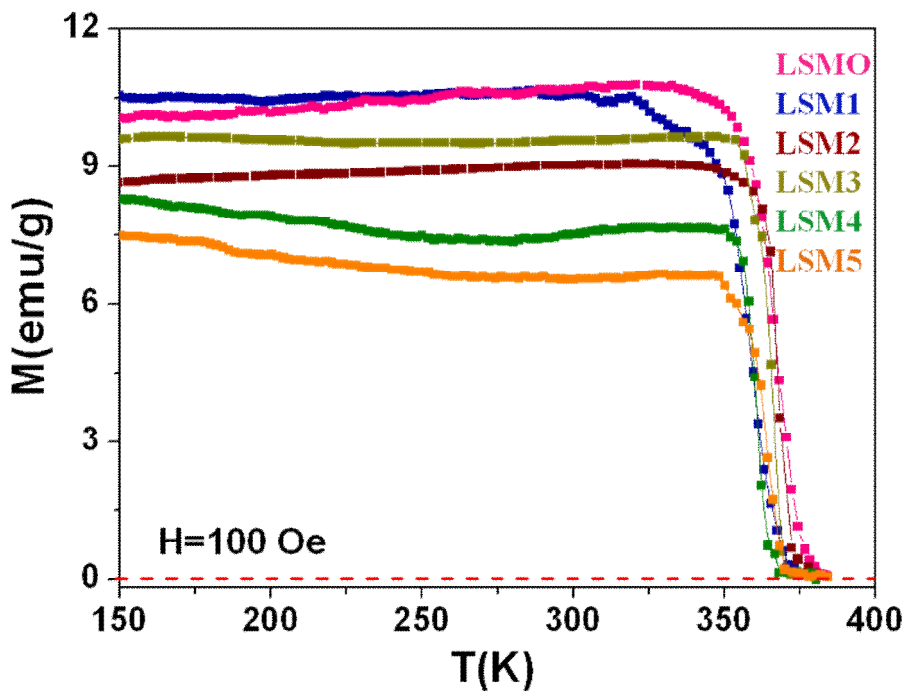


Fig. 4.5. Temperature dependence of magnetization for samples. The M - T curves were measured with field-cooled warming procedure under the applied field of 100 Oe.

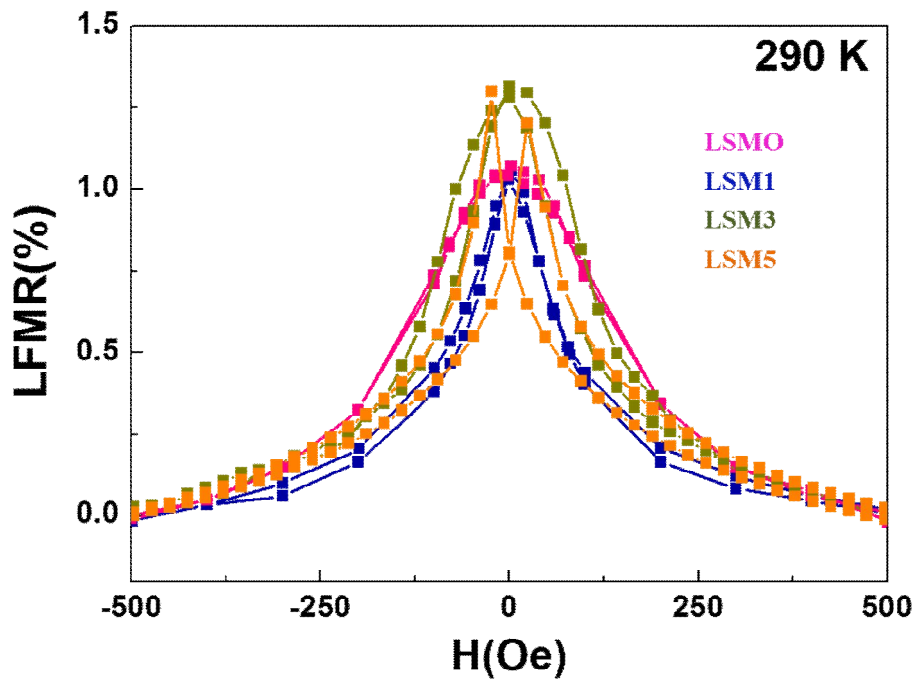


Fig. 4.6. The LFM R behaviors of the LSMO and composite samples measured at 290 K in 500 Oe.

Chapter 5. LSMO-manganese oxide composite thick films prepared by aerosol deposition

5.1. Introduction

The LFMR effect has been improved by preparing LSMO-insulating oxide composite films with various methods, including pulsed laser deposition (PLD) [1-3], magnetron sputtering [4], and metal-organic decomposition (MOD) [5, 6]. Reported LFMR values of the composite films are, however, still unsatisfactory for real applications since those are less than 1% at room temperature.

As an alternative approach to improve the LFMR effect, in this study, we tried to utilize the aerosol deposition (AD) method, recently developed for the fabrication of dense ceramic films using fine powders at room temperature [7,8], for the fabrication of pure LSMO and LSMM composite films on the *poly*-YSZ substrates. As-deposited films by the AD method were post-annealed for the recovery of magnetism and also for a modification of LSMO grain boundary.

5.2. Experimental

A pure LSMO ($\text{La}_{0.7}\text{Sr}_{0.3}\text{MnO}_3$) and LSMM (40 mol% LSMO - Mn_3O_4) composite films were prepared as the following. At first, utilizing the AD method, we deposited powders of LSMO and LSMM on the *poly*-YSZ (Yttrium Stabilized Zirconia, 8 mol% Y_2O_3 - Zr_2O_3) substrates at room

temperature. The pure LSMO and LSMM composite powders for AD were prepared by the conventional solid state reaction using precursor powders of La_2O_3 , SrCO_3 and Mn_2O_3 (all 99.9% purity). Precursor powders were weighed, ball-milled, and calcined at the temperature of 1100°C for 8 h in air to synthesize the LSMO compound and LSMM composite. AD-deposited films were annealed at 1100 and 1200°C for 2 h in air. The *poly*-YSZ substrates were sintered at 1550°C for 4 h in air, mechanically thinned, and surface-polished. In the AD process, as-synthesized powders were mixed with the nitrogen carrier gas to form an aerosol flow in the aerosol chamber. The aerosol state of powders could be formed by feeding the nitrogen carrier gas with the flow rate of 20 l/min and an additional mechanical vibration in the vertical direction. Powders in the aerosol state could be accelerated onto substrates in deposition chamber through the linear-type nozzle system by controlling the working pressure in the vacuum chamber below 10 Torr.

Phase analysis was performed by X-ray diffraction (D8 Advance, Bruker). Microstructure was analyzed by scanning electron microscopy (SEM) (JSM-6330F, JEOL). Temperature and field dependencies of magnetization were measured with a superconducting quantum interference device (SQUID) magnetometer (MPMS XL5, Quantum Design). The M - T curves were measured with zero field-cooled warming procedure in the field of 1 kOe applied parallel to the film plane. The magnetic field was also applied parallel to the film plane for the measurement of magnetization versus magnetic field (M - H) curves. The transport measurements for the evaluation of the LFMR and high-field magneto-resistance (HFMR) effects were performed using the standard four probe method within the SQUID magnetometer, where both electrical current and magnetic field were applied

along the long dimension of films. The T_c values of the films were determined by an extrapolation of magnetization versus temperature curves to the temperature axis of zero magnetization value in the ferromagnetic state.

5.3. Results and discussion

Fig. 5.1 (a) and (b) show the XRD patterns for pure LSMO and LSMM composite films, respectively. For a comparison, XRD patterns of *as*-synthesized powders are also shown in Fig. 5.1. Sample IDs in Fig. 5.1 are listed in Table 5.1. The most conspicuous feature in this figure is the XRD peak broadening of *as*-deposited films by the AD process. Similarly, Choi *et al.* [8] have reported the XRD peak broadening for *as*-deposited PZT films by AD. In accordance with their suggestion, we also regard residual strains and nano-sized grains as the origin for the XRD peak broadening. The strong and sharp XRD peaks of LSMO for post-annealed films are most probably due to a stress relief and a grain growth. In addition, as shown in Fig. 5.1 (b), relatively large XRD peaks of Mn_3O_4 in *as*-calcined LSMM composite sample are unobservable for *as*-deposited films and become very small for post-annealed films. The reason for these observations is unclear at the moment.

The SEM micrographs of all films are represented in Fig. 5.2. The surface morphologies of *as*-deposited films are shown in Fig. 5.2 (a) and (b), which is similar to typical morphologies of various other *as*-deposited oxide films like Al_2O_3 [7] and PZT [7, 8] by AD. The average grain size of both post-annealed LSMO and LSMM composite films increases with increasing

the annealing temperature (T_{an}). Interestingly, the LSMM composite films exhibit much larger average grain sizes than those of LSMO films, which is quite opposite to the microstructural observations for LSMO and LSMM composite bulk samples [9]. Normally, the grain growth of A in A-B composite oxides is hindered by the existence of B and hence the growth rate of pure A oxide is much faster than that of A in A-B composite oxides at a given annealing condition if A and B are chemically compatible. However, our post-annealed samples show the opposite trend.

To identify the origin for this peculiar phenomenon, we performed TEM analysis on the cross-sections of the films annealed at 1200°C. The cross-sectional TEM images of the LSMO and LSMM composite films are shown in Fig. 5.3. The TEM images of Fig. 5.3 (a) and (b) show the low-magnification images of LSMO and LSMM composite films, respectively. In accordance with the SEM plan-view observations in Fig. 5.2, the average grain size in the LSMM composite film in Fig. 5.3 (b) is much larger than that of the LSMO film in Fig. 3(a). Fig 5.3 (c) and (d) show elemental mappings of the LSMO and LSMM composite films, respectively, which were analyzed by the scanning transmission electron microscopy (STEM)-energy dispersive X-ray spectroscopy (EDS). Fig. 5.3 (d) shows that the Mn_3O_4 grains coexist with the LSMO grains in the LSMM composite film. To further identify the origin for larger grain growth in the LSMM composite film, we performed the high resolution (HR)-TEM analyses as shown in Fig. 5.3 (e) and (f). While a clean interface between LSMO and YSZ substrate is observed in Fig. 5.3 (e), an intermixed layer is clearly observed at the interface between Mn_3O_4 and YSZ substrate in Fig. 5.3 (f). From the fast Fourier transform (FFT) converted SAD (selected area diffraction) patterns

shown in the inset, it can be seen that the intermixed layer is the cubic-ZrO₂ phase transformed from the tetragonal-ZrO₂ phase. This phase transformation might be due to a reaction between Mn₃O₄ and YSZ during post-annealing procedure since no reaction was observed between LSMO and YSZ. The cubic-ZrO₂ phase formation of YSZ due to the diffusion of Mn in Mn₃O₄ into YSZ has been reported by several researchers [10, 11]. Further, enhanced grain growth of YSZ due to the Mn diffusion was also reported by Tsuyoshi Kawashima et al. [11]. The reaction between Mn₃O₄ and YSZ seems to induce enhanced grain growth of LSMO in our LSMM composite film, of which origin, however, requires further identification.

The resistivity curves for post-annealed LSMO and LSMM composite films are shown in Fig. 5.4. The resistivity values for both samples are decreased with increasing the T_{an} , which is attributed to a significant reduction in the LSMO grain boundary area because of grain growth. Since the average grain size (~ 600 nm) of LSMO grains in post-annealed LSMM composite films is much larger than that (~ 200 nm) of post-annealed LSMO films, which are annealed at 1200°C, the composite films have lower resistivity values than LSMO films although those include insulating Mn₃O₄ grains. On the other hand, The T_{M-I} (metal-insulator transition temperature) points are represented as the arrows in Fig. 5.4. With increasing the T_{an} , the T_{M-I} values are increased from ~ 194 and 287K to 266 and 289K for LSMO and LSMO composite films, respectively. This result is also attributed to the grain growth of LSMO during the post-annealing heat treatment at 1200°C. Compared with the LSMO bulk samples [9], the LSMO films show around 10 times larger resistivity values. This increase in resistivity is attributed to a large increase in the grain boundary area because

of greatly reduced average grain size of LSMO. While the average grain size of LSMO is $\sim 10.2 \mu\text{m}$ in the LSMO bulk sample sintered at 1300°C in air, it is $\sim 100 \text{ nm}$ in the LSMO films post-annealed at 1200°C as shown in Fig. 5.2.

Temperature dependence of magnetization is shown for all films in Fig. 5.4. The inset figure shows the M - T curves of *as*-deposited films. The T_C values of post-annealed LSMO and composite films are listed in Table 5.1. As-deposited LSMO and LSMM composite films commonly exhibit very broad ferromagnetic-paramagnetic (FM-PM) phase transition and relatively lower saturation magnetization (M_s) values compared with those of post-annealed films. For the annealed LSMO and LSMM composite films, the T_C values increase above room temperature and thus become close to the T_C value of bulk sample ($\sim 370\text{K}$) which is most probably due to improved crystallinity of LSMO grains as previously mentioned on the basis of XRD patterns in Fig. 5.1. Another magnetic phase transition observed at $\sim 43\text{K}$ in the annealed LSMM composite films is originated from the ferromagnetic to paramagnetic transition of the tetragonal Mn_3O_4 phase [12]. The coercivity fields (H_c) of films are also listed in Table 5.1. With increasing the T_{an} from 1100 to 1200°C , the H_c values measured at 300K are decreased from 20 and 39 Oe to 16 and 15 Oe for the LSMO and LSMM composite films, respectively, which is surely due to a reduction in the LSMO grain boundary area, acting as the domain wall pinning site, because of faster grain growth. In fact, somewhat larger average grain size of LSMO is observable for the LSMO and LSMM composite films annealed at 1200°C in Fig 5.2. (c) – (f).

The LFMR behaviors of the samples at 100K and 300K are shown in Fig. 5.6 (a) and (b), respectively. The LFMR values of samples were

calculated by equation of $MR = 100 \times (\rho_H - \rho_0) / \rho_0$, where ρ_0 and ρ_H are the resistivity values at zero field and with applied field, respectively. All post-annealed LSMM composite films show much higher LFMR values at 300K than post-annealed LSMO films. With increasing the T_{an} from 1100 to 1200°C for the LSMM composite films, while the LFMR value at 100K in 1.5 kOe is decreased from 11.2 to 9.6%, the LFMR value at 300K in 0.5 kOe is slightly increased from 1.09 to 1.12%. Compared with annealed LSMO films, the MR peaks of annealed LSMM composite films commonly become sharper, and thus the field sensitivity of $(dMR/dH)_{max}$ values are increased as listed in Table I. The highest $(dMR/dH)_{max}$ value of 158.8 %kOe⁻¹ at 300 K was achievable from the LSMM composite film annealed at 1200°C. This sample shows the LFMR value of 0.8% even at 50 Oe. Especially, both annealed composite films show the $(dMR/dH)_{max}$ values greater than 100 %kOe⁻¹ in a field range of 10~30 Oe which are unprecedentedly high values for pure manganite bulks and LSMO -based composite bulks and films ever reported [4, 9, 13]. According to previous reported paper, 28.3 %kOe⁻¹ at 300 K in a field range of 10~30 Oe was obtained from a same composition of LSMM composite bulk sample [9], 37.4 %kOe⁻¹ at 300 K in a field range of 10~30 Oe from a 0.9 μm-thick LSMO-50 mol% Mn₃O₄ composite film deposited by dc sputtering [4], and ~12 %kOe⁻¹ and ~20 %kOe⁻¹ at room temperature in a field range of 10~30 Oe from La_{0.67}Sr_{0.33}MnO₃ and La_{0.67}Ba_{0.33}MnO₃ bulk samples, respectively [13]. This result implies that the annealed LSMM composite film is very promising for real applications since a MR sensor should operate under very low field (<several tens of oersted) at room temperature. The enhanced LFMR behaviors in the LSMM composite films are attributed to a sharp grain

boundary effect [9]. The sharp grain boundary effects of LSMO are obviously achievable from annealed composite films.

Fig. 5.7. (a) and (b) show another evidence supporting the sharp grain boundary effect of the composite film. This figure indicates the high-field magnetoresistance (HFMR) of annealed films measured at 100 K and 300 K. In high magnetic field (> 0.2 T), while the resistance slope with field $d(R/R_0)/dH$ at 100 K are 0.466 and 0.361 %kOe⁻¹, those at 300 K are 0.372 and 0.355 %kOe⁻¹ for LSMO and composite films annealed at 1200°C, respectively. The values of $d(R/R_0)/dH$ of the LSMO film at 100 and 300K are higher than those of the LSMM composite film, implying that the spins at the grain boundary region have already been better aligned. Thus, it can be understood that the composite film has sharper grain boundaries with strengthened grain boundary surface ferromagnetism compared with pure LSMO film.

5.4. Conclusions

The enhanced LFMR properties of polycrystalline La_{0.7}Sr_{0.3}MnO₃-manganese oxide composite films on YSZ substrates can be obtained by aerosol deposition method and then followed by the post-annealing at the temperatures of 1100, 1200°C for 2 h. While as-deposited films commonly show poor magnetic properties, the post-annealed films exhibit very good magnetic properties with T_c ranging from 355 to 370K. Especially, the LFMR and the $(dMR/dH)_{\max}$ values of all LSMO-manganese oxide composite films are much higher than those of pure LSMO films, suggesting that a magnetic disorder at the LSMO grain boundary, known as a key factor

suppressing effective spin-dependent scattering center, can be effectively cured by the addition of manganese oxide. The maximum LFMR value of 1.2% and the $(dMR/dH)_{\max}$ value of 158.8 \%kOe^{-1} at 300 K in 0.5 kOe could be achieved from the composite film annealed at 1200°C with almost no variation in resistivity. Consequently, the $\text{La}_{0.7}\text{Sr}_{0.3}\text{MnO}_3$ -manganese oxide composite films are very promising alternative for the LFMR device application.

References

- [1] Zhenxing Bi et al., *J. Appl. Phys.* **109** (2011) 054302.
- [2] L. Yan et al., *J. Appl. Phys.* **96** (2004) 1568.
- [3] A. Chen et al., *Adv. Funct. Mater.* **21** (2011) 2423.
- [4] Y. M. Kang et al., *J. Magnetism* **17** (2012) 265.
- [5] S. A. Koster et al., *Appl. Phys. Lett.* **81** (2002) 1648.
- [6] I. B. Shim et al., *J. Mag. Mag. Mat.* **239** (2002) 279.
- [7] Akedo J., *J. Am. Ceram. Soc.* **89** (2006) 1834.
- [8] J. J. Choi et al., *J. Appl. Phys.* **102** (2007) 044101.
- [9] Young-Min Kang et al., *Appl. Phys. Lett.* **95** (2009) 052510.
- [10] Tsuyoshi Kawahima, *Materials Transactions JIM*, **40** (1999) 967.
- [11] Tsuyoshi Kawahima and Masakazu Hishinuma, *Materials Transactions JIM*, **39** (1998) 617.
- [12] A. S. Borovick-Ramanove and M. P. Orlova, *Sov. Phys. JETP*, **5** (1957) 1023.
- [13] Yunhui Xu, U. Memmert and U. Hartmann, *Sens. Actuators A: Physical*, **91** (2001) 26.

Table 5.1. Sample identifications (IDs) and properties of samples: Curie temperature (T_c), Coercivity (H_c), resistivity (ρ) measured at 300 K, MR values at 100 K in 1.5 kOe, MR values and $(dMR/dH)_{\max}$ values at 300K in 0.5 kOe of the LSMO and LSMO-manganese oxide composite films prepared at the T_{an} of 1100 and 1200°C, respectively. The data from ref. [9] for the composite bulk with the same composition are also listed for a comparison.

	Sample IDs	T_c (K)	H_c (Oe)	ρ (Ωcm)	MR (%) at 100 K	MR (%) at 300 K	$(dMR/dH)_{\max}$ (%/kOe) at 300 K
LSMO films	LSMO 1100	357	20	0.817	10.8	0.58	10.6
	LSMO 1200	358	16	0.250	12.2	0.70	15.7
LSMM composite films	LSMM 1100	370	39	0.153	11.2	1.09	131.6
	LSMM 1200	357	15	0.052	9.6	1.12	158.8

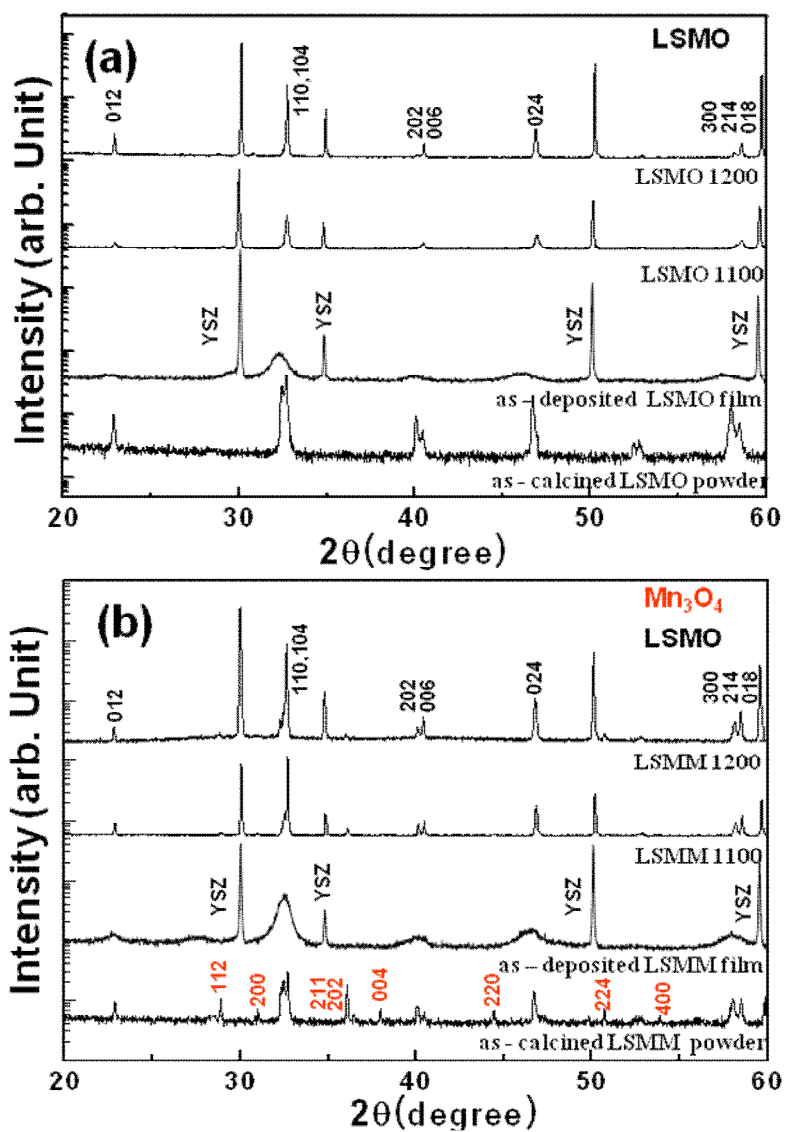


Fig. 5.1. XRD patterns of (a) calcined LSMO powder, *as*-deposited LSMO film by AD process, and annealed LSMO films, and (b) calcined LSMM composite powder, *as*-deposited LSMM composite film by AD process, and annealed LSMM composite films.

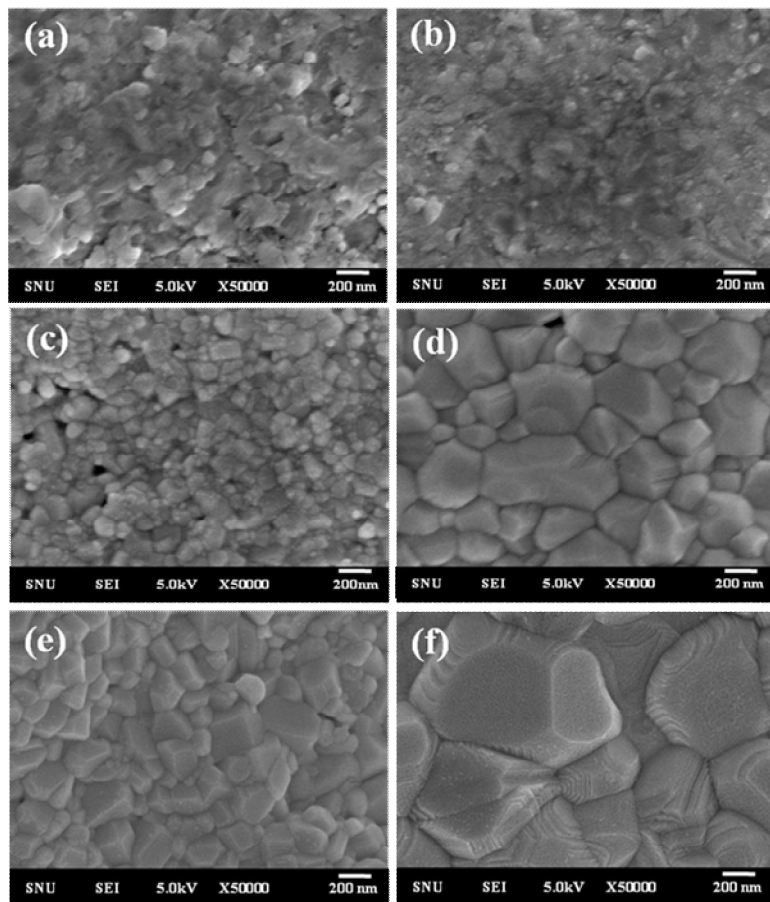


Fig. 5.2. SEM micrographs of (a) as-deposited LSMO, and (b) composite films, (c) LSMO film, and (d) LSMM composite film annealed at 1100°C, and (e) LSMO film and (f) LSMM composite film annealed at 1200°C.

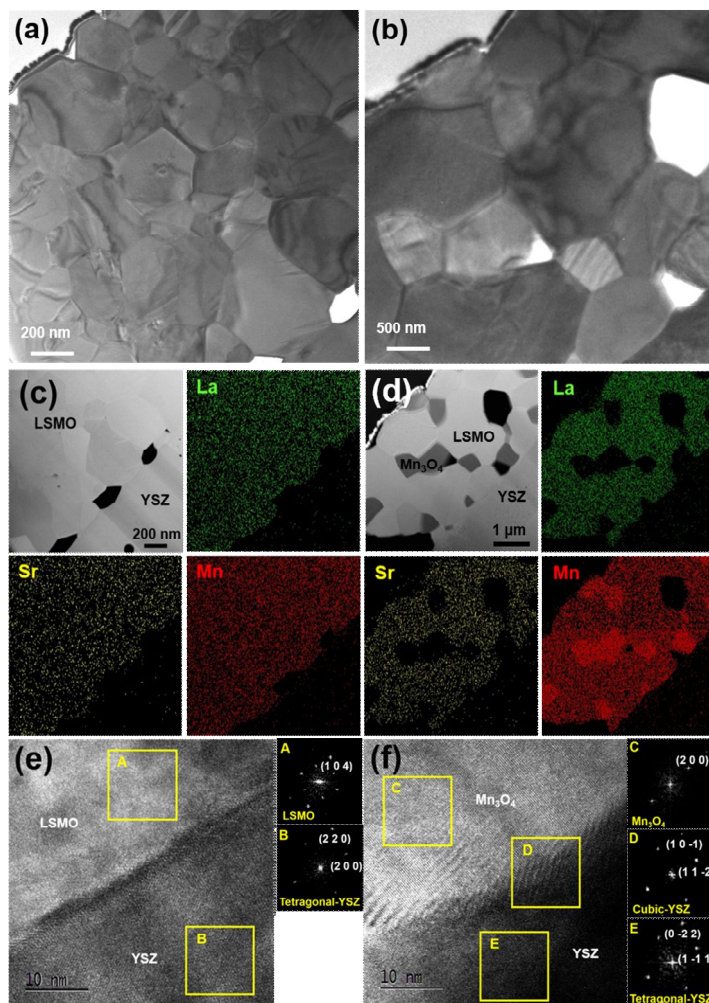


Fig. 5.3. The cross-sectional TEM images of the (a) LSMO and (b) LSMO composite films annealed at 1200 °C. The cross-sectional Z-contrast STEM images of the (c) LSMO and (d) LSMM composite film, and the La, Sr, Mn spectral images. High resolution TEM images of the (e) LSMO and (f) LSMM composite film, and inset in (e) and (f) represents FFT patterns of the square area related by a yellow line.

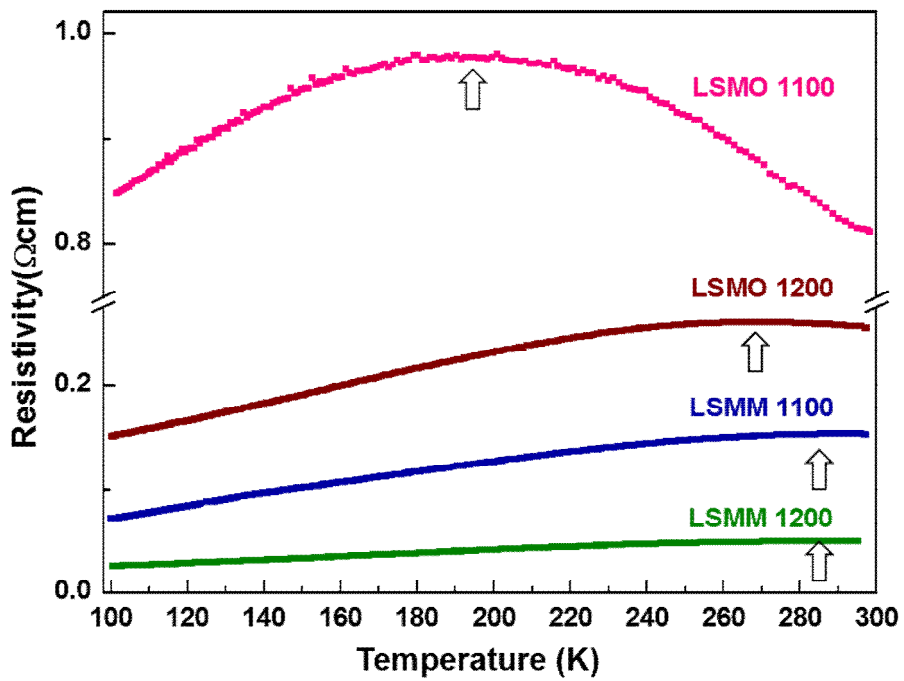


Fig. 5.4. $\rho - T$ curves for post-annealed LSMO and LSMM composite films.

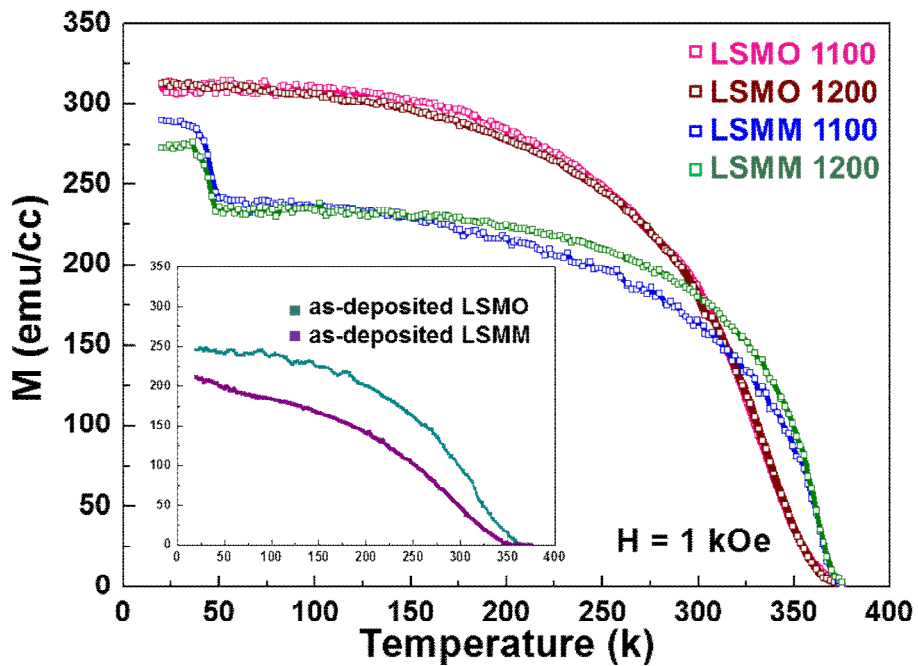


Fig. 5.5. The M - T curves for annealed LSMO films and LSMM composite films. Inset figure shows the M - T curves for *as*-deposited LSMO and composite films by AD process.

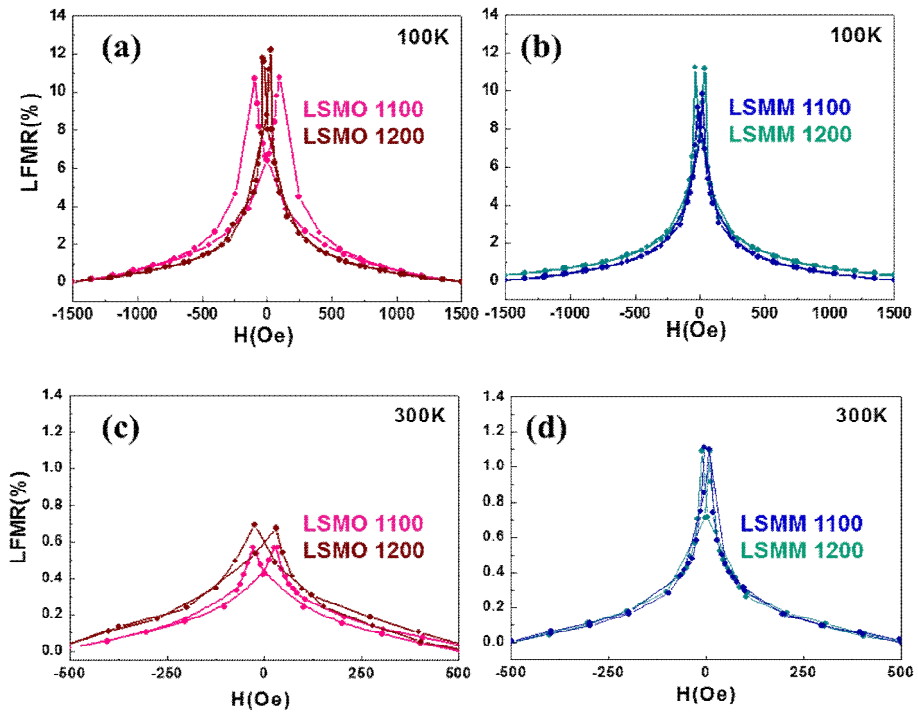


Fig. 5.6. The LFM R behaviors of post-annealed films: (a) LSMO and (b) LSMM composite films measured at 100 K, (c) LSMO and (d) LSMM composite films measured at 300 K.

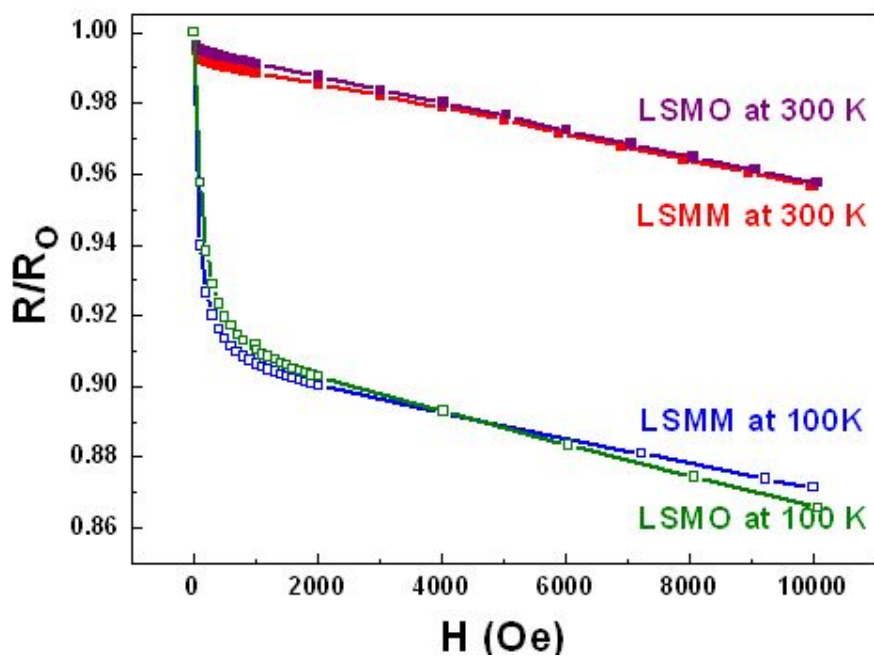


Fig. 5.7. The $R(H) / R(H=0)$ ratios of LSMO and LSMM composite films annealed at 1200°C , versus the applied field up to 10 kOe, measured at 100 and 300 K.

Chapter 6. Ga-doped MnZn ferrites

6.1. Introduction

The LFMR effect has drawn a continuous interest from researchers due to a potential application for MR devices. Up to date, a lot of work has been carried out to realize a LFMR sensor competitive with the GMR and AMR sensors. However, a large LFMR effect sufficient for real devices is usually obtainable at the temperatures much lower than room temperature. Therefore, in order to realize the LFMR sensors operating at room temperature, a new magnetic material with higher LFMR effect at room temperature must be developed.

Spinel ferrites have been important soft magnetic materials because of their excellent combination of good electrical and magnetic properties [1]. On the other hand, since magnetite shows high T_c and half metallic behavior, studies of the LFMR effect in the spinel ferrites [2-10] have been focused mainly on the magnetite, Fe_3O_4 , up to now. Only a few reports are found for other spinel ferrites [11-13]. For example, the LFMR effect was found in a $MnFe_2O_4$ nanoparticle compact, and its LFMR ratio was reported to be about 1% at RT in 0.5 kOe [13].

MnZn ferrites must be also a potential candidate to overcome the present limitation of the LFMR effect at room temperature since MnZn ferrites have relatively high saturation magnetization and low resistivity in comparison with other spinel ferrites [14]. The MnZn ferrites have been normally applied for high density magnetic cores, read-write heads for high speed disk recording, high-frequency transformers, and high-frequency

inductors. The MnZn ferrites are known to have a mixed spinel structure in which the tetrahedral sites are shared by 80% Mn^{2+} and 100% Zn^{2+} ions and the octahedral sites are shared by 20% Mn^{2+} and 100% Fe^{3+} ions. They are ferrimagnets with high T_c values (the highest $T_c \sim 600$ K for MnFe_2O_4 , and T_c is decreased with increasing the Zn content in the Mn site), which is explained in terms of a double exchange interaction [14]. However, the LFMR properties of MnZn ferrites have never been reported yet. Furthermore, in our preliminary experiments, the electrical resistivity of MnZn ferrites could be drastically decreased by substituting the Ga^{3+} ions for the $(\text{Mn}, \text{Zn})^{2+}$ sites.

In this work, we carefully investigated the LFMR effects in polycrystalline pure and Ga-doped MnZn ferrites with various Ga_2O_3 doping concentrations. In order to understand the mechanism of the LFMR effect in MnZn ferrites, we studied the relationship between the AC electrical properties and magneto-transport properties by impedance spectroscopy with AC frequencies in the region of 100 ~ 40 MHz over the temperature region of -100 ~ 120°C.

6.2. Experimental

Polycrystalline bulk samples of Ga-doped MnZn ferrite were prepared by the conventional solid state reaction. The precursor materials of Mn_2O_3 , ZnO , Fe_2O_3 powders with all 99.9% purity were weighed to have the nominal compositions of $(\text{Mn}_{0.8}\text{Zn}_{0.2})_{(1-x)}\text{Ga}_x\text{Fe}_2\text{O}_4$ ($x = 0, 0.01, 0.02, 0.03, 0.05, 0.1$) and ball-milled in ethyl alcohol using ZrO_2 balls for 24 h. The dried powder mixture was calcined twice at 1200°C for 8 h in air with an intermediate grinding. As-calcined powder were uniaxially pressed into

pellets with the diameter of 10 mm, and then consolidated by cold isostatic pressing ($\sim 2 \text{ ton cm}^{-2}$). The pellets were sintered at 1400°C for 2 h in air. To investigate the effect of the sintering conditions on the LFMR effect, 2 mol% Ga-doped MnZn ferrites were sintered in air at the temperature region of $1250 \sim 1500^\circ\text{C}$ for the holding periods of 30 min \sim 3 h.

High resolution X-ray diffraction (XRD, BRUKER D8 ADVANCE) with θ - 2θ scan using Cu- $K\alpha$ radiation ($\lambda = 1.54 \text{ \AA}$), and scanning electron microscopy (SEM (JEOL JSM-6360), FE-SEM (JSM-6330F)) were performed for phase and microstructure analysis, respectively. Temperature and field dependencies of magnetization were measured with a vibrating sample magnetometer (VSM). The M - T curves were measured under the applied field of 3 kOe by VSM. The LFMR properties were measured using the standard four probe method within a magnetoresistance measurement system. Both the electrical current and magnetic field were applied along the long dimension of samples (see Fig. 6.1). The frequency-dependent resistance and capacitance were measured by an impedance/gain-phase analyzer (HP-4194a) in the frequency range from 100 Hz to 40 MHz with an oscillation voltage of 500 mV. For evaluating the resistivity and capacitance values of grain and grain boundary, the Z^* spectroscopy analysis was performed at the temperatures ranging from -100°C to 120°C .

6.3. Results and discussion

6.3.1 LFMR properties of Ga-doped MnZn ferrites

The XRD patterns for the pure MnZn ferrite and Ga-doped MnZn

ferrite bulks with varying Ga_2O_3 doping concentrations are presented in Fig. 6.2 (a). From the XRD patterns, all peaks in both undoped- and Ga-doped MnZn ferrite bulks belong to the cubic spinel phase and thus no other second phases are detected. Fig. 6.2 (b) shows the lattice parameters of the samples. The inset shows that the main peaks ($2\theta \sim 29^\circ$) of samples are shifted to higher diffraction angle with increasing the Ga substituent x for the $(\text{Mn}, \text{Zn})^{2+}$ site, indicating that relatively small size of the Ga^{3+} ion ($a = 0.47 \text{ \AA}$) can substitute the $(\text{Mn}, \text{Zn})^{2+}$ sites for the full range of doping concentration, i.e. $x=0.1$, in this study. It is interesting to note that after a large decrease in the lattice parameter with 1 mol% Ga doping, the lattice constant is linearly decreased with increasing up to 10 mol% Ga doping, which seems to follow the Vegard's rule quite well. The reason for this peculiar variation is unclear now and thus further study is under progress.

The SEM micrographs of pure and Ga-doped MnZn ferrite samples are shown in Fig. 6.3(a)-(e). All samples are observed to be composed of large grains. These abnormally grown large grains contain many pores within the grains (intra-granular pores) and also at the grain boundary region (inter-granular pores). While the average grain size of undoped sample was $\sim 75 \text{ }\mu\text{m}$, those of all Ga-doped samples were about $\sim 55 \text{ }\mu\text{m}$ as shown in Fig. 6.3(f).

The temperature dependency of the magnetization for pure and 2 mol% Ga-doped MnZn ferrite samples is shown in Fig. 6.4 (a). One can see that the effect of Ga^{3+} substituent for the $(\text{Mn}, \text{Zn})^{2+}$ site on the paramagnetic-ferrimagnetic transition temperature is insignificant. The magnetization curves and normalized ones at low field regime ($0\sim 3 \text{ kOe}$) of the samples are presented in Fig. 6.4 (b) and (c), respectively. All samples showed small M -

H hysteresis curves with coercivity field (H_c) of ~ 10 Oe. However, all Ga-doped samples except the sample with $x=0.1$ show much steeper initial magnetization curves compared with undoped sample. It is also shown that 2 mol% Ga-doped MnZn ferrite exhibits the highest initial susceptibility defined by $(dM/dH)_{H=0}$.

In order to investigate the Ga_2O_3 doping effects on the electrical properties of MnZn ferrite, we have measured the resistivity of samples as a function of temperature. As shown in Fig. 6.5, while the resistivity value of the Ga-doped MnZn ferrite sample abruptly decreases with increasing x from 0 to 0.02, then slightly decreases with further increasing x from 0.02 to 0.03, again abruptly decreases from 0.03 to 0.05, and then slightly decreases from 0.05 to 0.1. The decrease in resistivity is ascribed to increased hopping electrons between Fe^{2+} and Fe^{3+} with increasing the doping content of Ga_2O_3 . However, the reason for this discontinuous decrease in resistivity with increasing x is unclear at the moment. These results might be due to a hole doping effect by the Ga^{3+} ion substitution for the $(\text{Mn}, \text{Zn})^{2+}$ sites. This suggestion is in good agreement with previous report [15] arguing that Ga^{3+} ions can occupy the tetrahedral sites in the spinel structure.

The LFMR values of samples are represented in Fig. 6.6. The LFMR values at RT were evaluated using the equation of $\text{MR} (\%) = (\text{R}_H - \text{R}_{H=500\text{Oe}}) / \text{R}_{H=500\text{Oe}} \times 100\%$. The magneto-transport properties of all samples measured in this study are summarized in Table 6.1. While the maximum LFMR value of pure MnZn ferrite sample is 1.5%, it is abruptly increased to 2.5% for the sample with $x = 0.02$, and then it monotonously decreases with further increasing x up to 0.1. This behavior can be understood as the following; various doping amounts of Ga_2O_3 can change the ratio of Fe^{2+}

against Fe^{3+} . With increasing x , the resistivity values are decreased, and thus the LFMR values can be varied. The mechanism of the LFMR behaviors in polycrystalline perovskites manganites, CrO_2 , Fe_3O_4 , and etc., has been explained in terms of the spin-polarized tunneling effect between neighboring grains [16], in which the grain boundary plays a role of the spin scattering center, and hence it is very important to control the microstructure for the enhancement of the LFMR effect. However, in this study, the average grain sizes of all samples are not much different from each other (see Fig. 6.3). Therefore, we speculate that the variation in their LFMR effects is closely related to the Ga_2O_3 doping content in the MnZn ferrite.

The $R(H)/R(H=0)$ ratios at RT of all samples versus the applied field are rerepresented in Fig. 6.7. These results show another evidence supporting the role of hopping electrons for enhanced LFMR effects. Below the magnetic fields of ~ 0.5 kOe, the LFMR value abruptly increases with increasing magnetic field, which is related to the LFMR effect. At higher fields ($H > 0.5$ kOe), the MR value almost lineally increases with increasing the field. Such an abrupt resistivity drop in low fields is attributed to the magnetic domain alignment. Much slower linear resistivity drop in high fields is due to a forced spin alignment in spin-disordered region near grain boundary. Fig. 6.7 also reveals that the slopes of $d(R/R_0)/dH$ in high field region ($H > 0.5$ kOe) are almost identical for all samples, i.e., independent of the Ga doping concentration of x . This result implies that the high field MR response is not related to the electrical properties but to the magnetic ordering of the spins at the grain boundaries, which is in good agreement with the suggestion of previous studies for the manganite systems [16 and references therein].

6.3.2 Effects of the annealing conditions on the LFMR properties of Ga-doped MnZn ferrites

In order to identify the annealing effect on the LFMR properties of 2 mol% Ga-doped MnZn ferrite, various annealing temperatures and times were applied for the fabrication of samples. Fig. 6.8 and 6.9 show the XRD patterns and SEM micrographs of samples sintered at various annealing conditions. From the XRD patterns, while the spinel phases of 2 mol% Ga-doped MnZn ferrite are detected in all samples. The Fe_2O_3 phase is detected in the samples sintered below 1400°C and holding periods below 2 h at 1400°C . Fig. 6.9(a) shows the surface images of sample sintered at 1250°C for 2 h. We can observe a characteristic microstructure composed of Fe_2O_3 and Ga-doped MnZn ferrite phases which might be due to the decomposition of Ga-doped MnZn ferrite phase during furnace-cooling. However, as the sintering temperature is increased over 1300°C , only MnZn ferrite single phase is observed, implying that the decomposition of Ga-doped MnZn ferrites are effectively prevented during furnace-cooling.

Fig. 6.10 (a) and (b) show various properties of 2 mol% Ga-doped MnZn ferrite as a function of the sintering temperature (at $1300\sim 1550^\circ\text{C}$ for 2 h) and holding period (for 30 min ~ 3 h at 1400°C) in air, respectively. As shown in Fig. 6.9 and Fig. 6.10 (a), abnormally grown large grains with the average grain size over $50\ \mu\text{m}$ are observed at the sintering temperature above 1400°C . It is also observed in Fig. 6.10 (b) that the abnormal grain growth is completed after 1 h and thus the average grain becomes constant up to the sintering period of 3 h. Meanwhile, in Fig. 6.10 (a), while the resistivity of sample sintered at 1300°C for 2 h are about $\sim 10^4\ \Omega\text{cm}$, it is abruptly

decreased to $\sim 10^2 \Omega\text{cm}$ at 1400°C for 2 h and almost unaltered up to 1550°C for 2 h. When the sintering temperature was raised above 1300°C , since Fe_2O_3 is reported to be converted into Fe_3O_4 [17], the concentration of divalent iron in the Ga-doped MnZn ferrite might be increased, and hence the resistivity could be decreased. Furthermore, the resistivities of samples are almost unchanged when holding periods are varied from 1 to 3 h after a small decrease from 30 min to 1 h at sintering temperature of 1400°C . Usually, the transport phenomenon in MnZn ferrites is based on the model of thermally activated hopping between local electronic states of iron ions. It is proposed that the electron exchange takes place between different valency metal ions occupying the octahedral sites of the spinel lattice [17]. Therefore, the conduction mechanism of all samples would be electron hopping between the Fe^{2+} and Fe^{3+} .

As shown in Fig. 6.10 (a) and (b), the maximum LFMR value of 2.8% in 0.5 kOe at RT is achieved from the sample sintered at 1300°C for 2 h. However, the resistivity is very high ($10^4 \Omega\text{cm}$ at RT), and hence it is required to lower resistivity without sacrificing the LFMR effect. As such an effort, we tried to study the two step sintering process. While sample was directly ramped up to the sintering temperature in one step sintering, samples were heated up to the sintering temperature and then heated up to the final firing temperature in two step sinterings, to be held for short periods (for 5 and 10 min, respectively). The heat treatment schedules are shown in Fig. 6.11.

As previously shown in Fig. 6.10 (a), resistivity of the sample sintered at 1400°C was abruptly decreased, probably due to enhanced electron hopping between Fe^{2+} and Fe^{3+} ions. Fig. 6.12 shows the XRD

patterns of 2 mol% Ga-doped MnZn ferrite samples sintered by two step sintering process. Both of samples show the single spinel phase without any second phases. The SEM micrographs of samples are shown in Fig. 6.13. It is observable that the grain size of the sample by two step sintering for 5 min (Fig. 6.13 (b)) is almost identical to that of the sample by one step sintering (Fig. 6.13 (a)). Meanwhile, abnormally grown large grains are observed for the sample sintered by two step sintering for 10 min in Fig. 6.13 (c). It can also be observed that most of pores exist at the grain boundary before abnormal grain growth in Fig. 6.13 (a) and (b), but those exist within grains after abnormal grain growth in Fig. 6.13 (c). We carried out the EBSD analysis for this sample, as shown in Fig 6.14. It is obvious that abnormally grown large grains are like porous single crystals.

In order to clarify the electron hopping effects in samples, we performed the XPS measurements as shown in Fig 6.15. Detailed atomic percentages and positions of Fe^{2+} and Fe^{3+} ions are listed in Table 6.2. One can see that the ratios of Fe^{2+} to Fe^{3+} ions are increased by two step sintering, resulting in increased electron hopping. The properties of samples sintered by one step and two step sintering are plotted in Fig. 6.16. Although the LFMR values of two step sintering samples are slightly increased, the resistivity values are abruptly decreased, which might be due to increased electron hopping, and, even more interestingly, the average grain size of the sample sintered by two step sintering for 10 min is much larger than that of the sample sintered by one step sintering. These results are quite different from other LFMR materials like perovskite manganites exhibiting that larger LFMR effect is obtainable from the sample with smaller grain size due to increased grain boundary acting as the spin-scattering center.

To explain the above peculiar LFMR behavior in Ga-doped MnZn ferrites, we tried to evaluate the electrical properties of grain and grain boundary quantitatively through the impedance analyses. Z^* and M^* spectroscopy were used for obtaining the quantitative ρ and C values of grain and grain boundary using the following equations [18],

$$M^* = j\omega C_0 Z^* = M' + jM'' \quad (\text{Eq. 6. 1})$$

$$Z''_{\max} = \frac{R}{2}, \quad M''_{\max} = \frac{C_0}{2C} \quad (\text{Eq. 6. 2})$$

$$\omega\tau = 2\pi f_{\max} RC = 1 \quad (\text{Eq. 6. 3})$$

where Z''_{\max} and M''_{\max} are the peak of imaginary part of Z^* and M^* spectroscopy, respectively, $C_0 = \epsilon_0(A/t)$, where ϵ_0 is the permittivity of free space (8.854×10^{-14} [F/cm]), A is the area of electrode, t is the sample thickness, f_{\max} is the top of arc in Z^* spectroscopy, and ω is the angular frequency. Fig. 6.17 (a), (c), and (e) show the frequency dependence of the Z'' values of samples measured at $-110 \sim 140^\circ\text{C}$. The ρ_g , ρ_{gb} , C_g , and C_{gb} values imply the ρ and C values of grain and grain boundary. These values were calculated using the equivalent circuit composed of two parallel RC elements of grain and grain boundary connected in series. The E_g and E_{gb} are the activation energy (E) of grain and grain boundary, respectively, which were calculated from the Arrhenius plots of σT vs $1/T$. The evaluated E_g , E_{gb} , ρ_g , ρ_{gb} , C_g , and C_{gb} values in samples are summarized in Table 6.3. As listed in Table 6.3, the ρ_{gb} and C_g values are smaller than those of ρ_g and C_{gb} values, respectively. It can be seen that samples having low resistivity have low activation energy and vice versa. The Arrhenius plots of $T\sigma$ versus inverse temperature ($10^3/T$) are shown in Fig. 6.16(b), (d), and (f). All the ρ_g

and ρ_{gb} values obey the Arrhenius law, and the activation energies from grain and grain boundary show the values of 0.23~0.31 and 0.37~0.39 eV, respectively. The decrease of E_g and E_{gb} can be explained by the fact that increased Fe^{2+} concentration in the samples prepared by two step sintering facilitates the electron hopping between Fe^{3+} and Fe^{2+} . The activation energies were obtained from the following equation [19]

$$\sigma = \frac{ne^2 a^2 f\nu}{kT} \exp\left(-\frac{E_H}{kT}\right) \quad (\text{Eq. 6.4})$$

where n is the density of small polarons, e the fundamental charge (1.6×10^{-19}), a the jump distance, f the probability of the nearest neighboring sites of a polaron being vacant, ν the vibrational attempt frequency, E_H the activation energy for a small polaron hopping, while the other terms have their usual significance. The activation energy is found to be sensitive to sintering conditions. Moreover, the difference between the activation energy of grain and that of grain boundary becomes the maximum value for the sample with abnormally grown large grains sintered by two step sintering for 10 min. In general, the grain boundaries are insulating while grains are more conducting in spinel ferrites. However, in this study, grain boundaries show lower resistivity values than those of grains in all samples. Interestingly, the LFMR value is increased with increasing the difference between E_g and E_{gb} ($E_g - E_{gb}$), implying that it is closely related to the magnetism of grains and grain boundaries. Further investigation is required for a full identification of the origin for the LFMR effect in Ga-doped MnZn ferrite with abnormally

grown large grains.

6.4. Summary

We have fabricated $(\text{Mn}_{0.8}\text{Zn}_{0.2})_{(1-x)}\text{Ga}_x\text{Fe}_2\text{O}_4$ ($x = 0, 0.01, 0.02, 0.03, 0.05, 0.1$) ceramics by the solid state reaction at various sintering conditions. The lattice parameters were decreased with increasing Ga_2O_3 substitution. From the transport measurements of our samples, it was found that, with the addition of the Ga_2O_3 dopant, the resistivity level of the pure MnZn ferrite was abruptly dropped over two orders of magnitude, and further the LFMR value at RT was greatly improved. Furthermore, we carefully investigated the effects of sintering temperature and holding periods on the microstructure and the LFMR properties of 2 mol% Ga-doped MnZn ferrite. The homogeneously distributed small grains ($\sim 10 \mu\text{m}$) in the sample sintered at 1300°C for 2 h were changed into abnormally large grains ($\sim 75 \mu\text{m}$) in the sample sintered at 1400°C for 2 h. The *dc* resistivity values and the LFMR values at RT in the samples showed a strong dependence on the sintering conditions and thus on microstructures. In addition, we tried to investigate the effects of two step sintering on the LFMR effect. The annealing process by one step (at 1300°C for 2h) and two step (sintered at 1300°C for 2 h and then directly additionally sintered at 1400°C for 5 and 10 min, respectively) for 2 mol% Ga-doped MnZn ferrite samples were used for this work. The LFMR properties of samples were strongly related to the electrical and magnetic properties. While the samples annealed by one step sintering showed the resistivity value of $\sim 11,994 \Omega\text{cm}$ with the LFMR value of 2.81% at RT, annealed by two step sintering with holding time of 5 min showed the

resistivity value of $\sim 1,860 \text{ } \Omega\text{cm}$ with LFMR value of 2.98% at RT. It was accompanied by a very high increase in the electron hopping between Fe^{2+} and Fe^{3+} with the almost same average grain size of $\sim 10 \text{ } \mu\text{m}$. With further increasing additional annealing holding time up to 10 min, an abnormal grain growth was occurred. This sample with the average grain size of $\sim 80 \text{ } \mu\text{m}$ showed the LFMR value of 3.07% with relatively lower resistivity value of $\sim 262 \text{ } \Omega\text{cm}$ at RT. The data measured by complex impedance (Z^*) spectroscopy revealed that the variation of LFMR values in the samples was exactly coincident with the difference in the activation energy (E_a) values between the grain and grain boundary. With increasing the difference in E_a between grain and grain boundary, the LFMR value of samples was increased.

References

- [1] N. S. Gajbhiye et al., *Hyp. Int.* **156/157** (2004) 57.
- [2] J.M.D. Coey et al., *Appl. Phys. Lett.* **72** (1998) 734.
- [3] J.M. Li et al., *Phys. Rev. B* **61** (2000) 6876.
- [4] M. Venkatesan et al., *J. Appl. Phys.* **93** (2003) 8023.
- [5] K. Liu et al., *J. Appl. Phys.* **93** (2003) 7951.
- [6] S.I. Rybchenko et al., *Phys. Rev. B* **72** (2005) 054424.
- [7] D. Serrate et al., *J. Appl. Phys.* **97** (2005) 084317.
- [8] W.D. Wang et al., *J. Appl. Phys.* **99** (2006) 08J108.
- [9] P.Y. Song et al., *J. Appl. Phys.* **100** (2006) 044314.
- [10] Z.L. Lu et al., *J. Phys. Chem. B* **110** (2006) 23817.
- [11] C. Y. Chou et al., *IEEE Trans. Magn.* **41** (2005) 906.
- [12] C. T. Lie et al., *IEEE Trans. Magn.* **39** (2003) 2800.
- [13] Junfeng Wang et al., *J. Magn. Mage. Mater.* **320** (2008) 227.
- [14] J. Smit and H. P. J. Wijn., “Ferrites” (1965).
- [15] C. Quintanar et al., *J. Magn. Mage. Mater.* **54-57** (1986) 1339.
- [16] P. K. Siwach et al., *J. Phys.: Condens. Matter.* **20** (2008) 273201.
- [17] Long Wu et al., *J. Phys. D: Appl. Phys.* **13** (1980) 259
- [18] V. P. Mirishkin et al., *Phys. Stat. Sol. (a)* **66** (1981) 503.

[19] H. I. Yoo and H. L. Tuller, *J. Am. Ceram. Soc.* **70** (1987) 388.

Table 6.1. Properties of Ga-doped MnZn ferrites: sample resistivity (ρ), LFMR and $(dMR/dH)_{\max}$ at RT, and relative sintered density.

The Ga doping content x	ρ (Ωcm)	LFMR (%)	dMR/dH (%/kOe)	Relative sintered density (%)
0	428.2	1.5	5.4	96.0
0.02	77.1	2.5	14.4	95.1
0.03	53.5	2.3	13.3	95.2
0.05	8.6	1.7	3.8	96.0
0.1	8.5	0.9	0.9	95.5

Table 6.2. Atomic percentages of Fe²⁺ and Fe³⁺ ions in 2 mol% Ga-doped MnZn ferrites prepared by different sintering conditions. The data were analyzed by XPS.

	One step (position, eV)	Two step 5 min (position, eV)	Two step 10 min (position, eV)
Fe ²⁺ (at%)	19.9 (711.7)	45.4 (711.4)	49.9 (711.3)
Fe ³⁺ (at%)	80.1 (713.0)	54.6 (713.0)	50.1 (713.0)

Table 6.3. The evaluated E_g , E_{gb} , $E_{gb}-E_g$, ρ_g , ρ_{gb} , C_g , and C_{gb} values of 2 mol% Ga-doped MnZn ferrites prepared by different sintering conditions. These data were analyzed by Impedance analysis.

	Activation energy (E) (eV)			Resistivity (ρ) (Ωcm)		Capacitance (C) (nF/cm)	
	E_g	E_{gb}	$E_{gb}-E_g$	ρ_g at 293 K	ρ_{gb} at 293 K	C_g at 293 K	C_{gb} at 293 K
One step	0.319 (± 0.0065)	0.395 (± 0.0034)	0.076	2285.1	207.48	0.14272	2.957
Two step 5min	0.247 (± 0.0121)	0.377 (± 0.0076)	0.130	13991.6	376.26	0.00796	28.952
Two step 10 min	0.231 (± 0.0038)	0.373 (± 0.0087)	0.142	727.0	617.35	0.00661	266.136

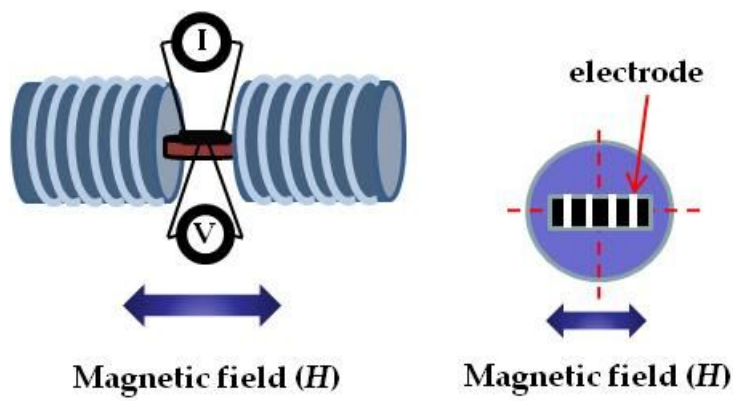


Fig. 6.1. Schematics of the magnetoresistance measurement system.

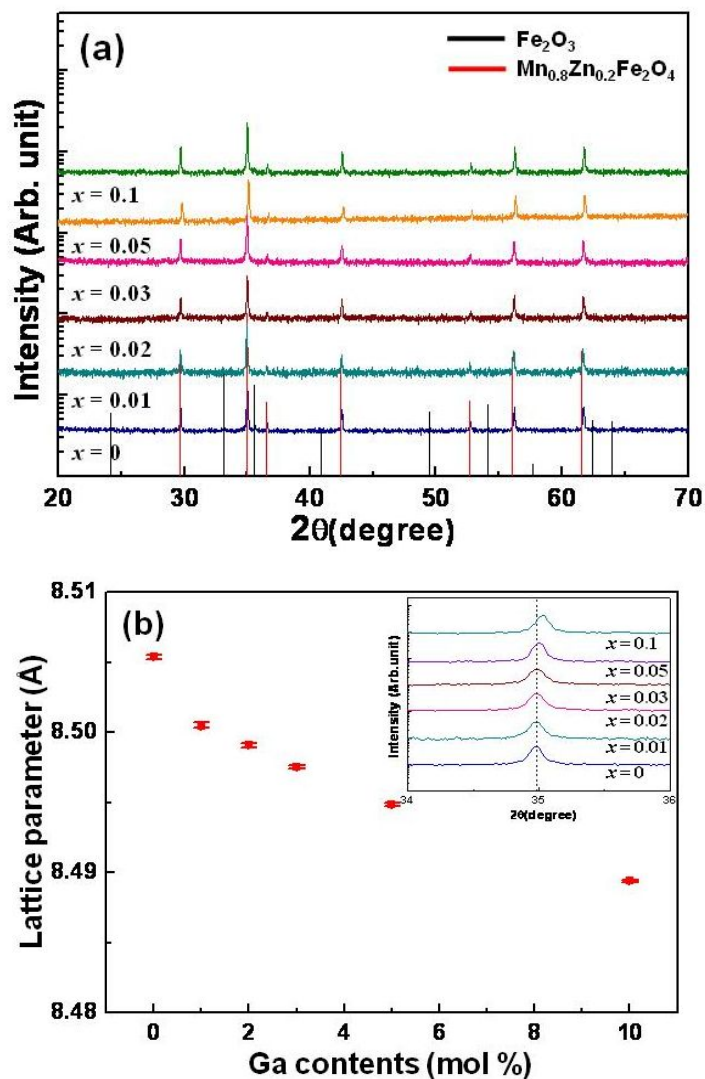


Fig. 6.2. (a) The XRD patterns and (b) the variation of the lattice constants of $(\text{Mn}_{0.8}\text{Zn}_{0.2})_{(1-x)}\text{Ga}_x\text{Fe}_2\text{O}_4$ ($x = 0, 0.01, 0.02, 0.03, 0.05, 0.1$) samples.

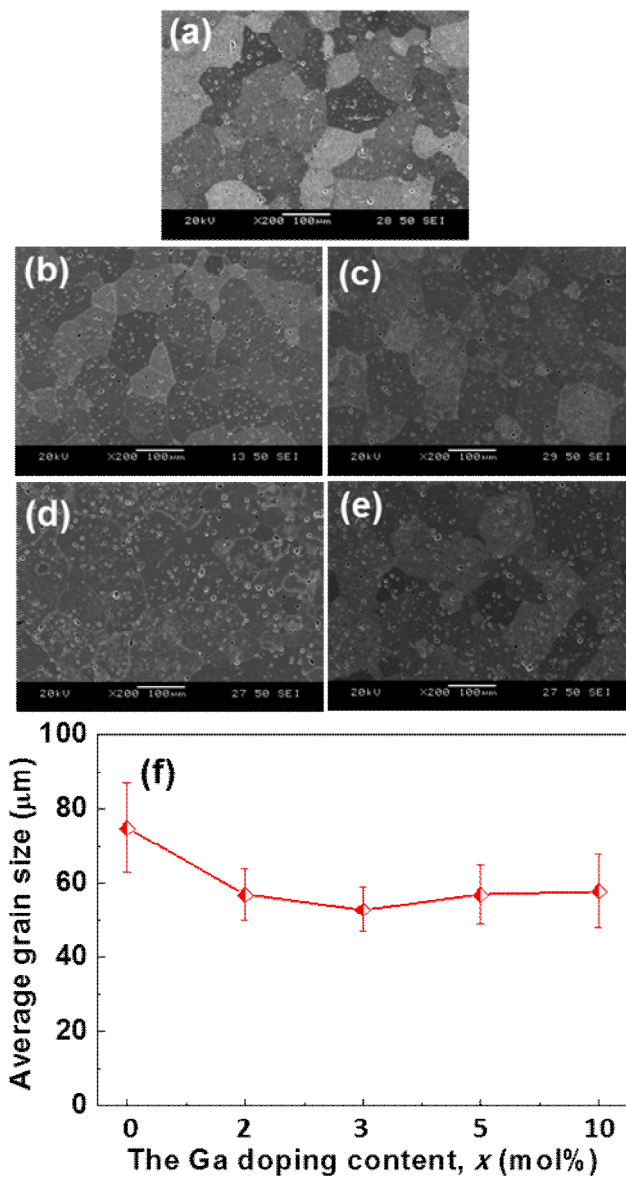


Fig. 6.3. SEM micrographs of (a) 0, (b) 2, (c) 3, (d) 5, and (e) 10 mol% Ga-doped MnZn ferrites. The average grain sizes versus the Ga₂O₃ contents in (Mn_{0.8}Zn_{0.2})_(1-x)Ga_xFe₂O₄ ($x = 0, 0.01, 0.02, 0.03, 0.05, 0.1$) samples.

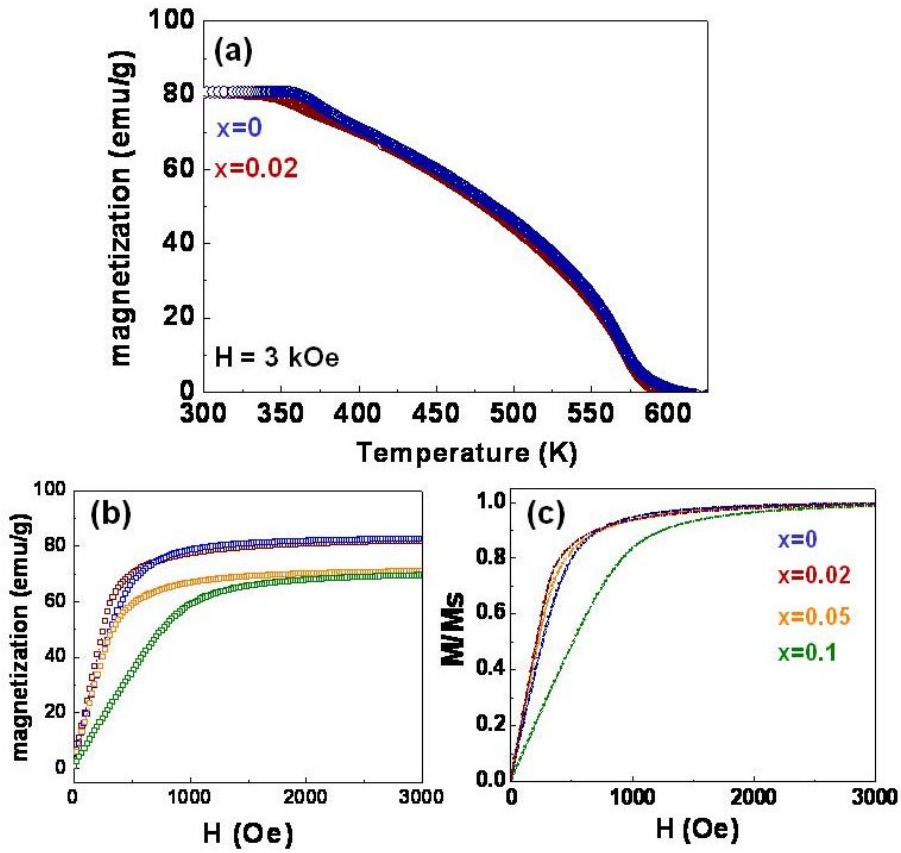


Fig. 6.4. (a) Temperature dependence of magnetization for MnZn ferrites. The M - T curves for the samples with $x = 0$ and 0.02 in $(\text{Mn}_{0.8}\text{Zn}_{0.2})_{(1-x)}\text{Ga}_x\text{Fe}_2\text{O}_4$ were measured with field-cooled warming procedure under the applied field of 3 kOe. (b) M - H curves and (c) M/M_s - H curves for the samples with $x = 0, 0.02, 0.05,$ and 0.1.

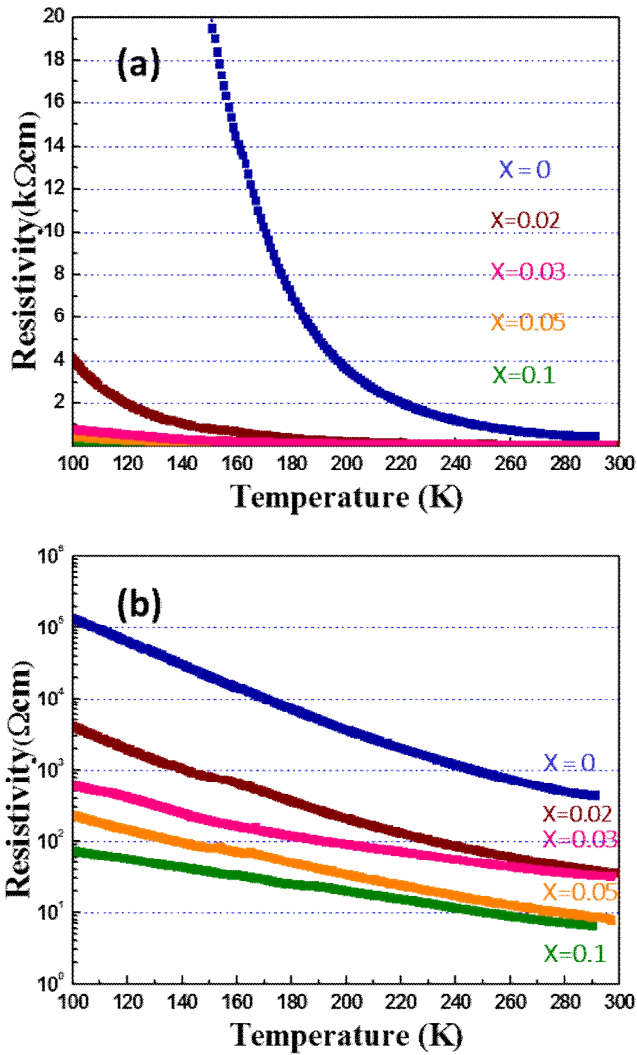


Fig. 6.5. The temperature dependence of resistivity for the $(\text{Mn}_{0.8}\text{Zn}_{0.2})_{1-x}\text{Ga}_x\text{Fe}_2\text{O}_4$ ($x = 0, 0.01, 0.02, 0.03, 0.05, 0.1$) samples. (a) Resistivity (ρ) vs T and (b) $\log \rho$ vs T plots.

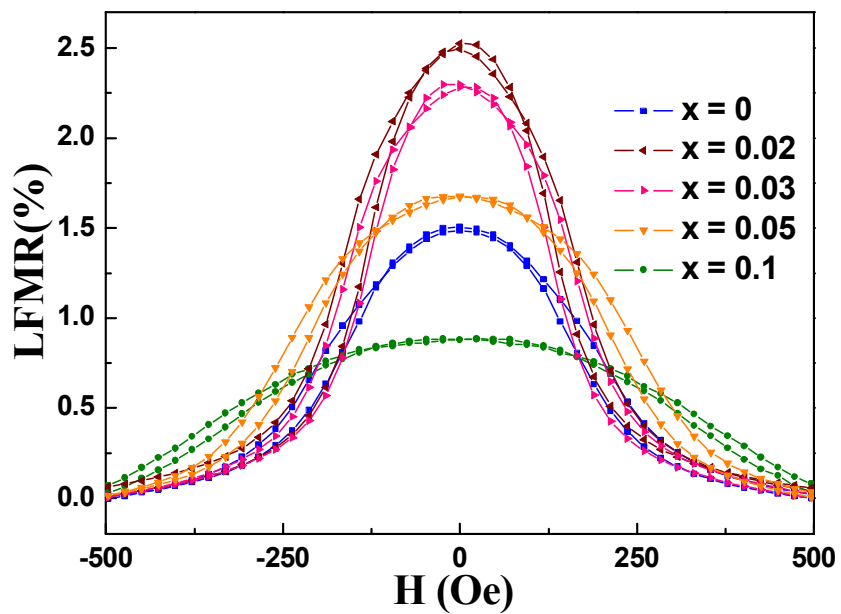


Fig. 6.6. The LFM R behaviors at RT for undoped and Ga-doped MnZn polycrystalline samples with $x = 0, 0.02, 0.03, 0.05,$ and 0.1 in $(\text{Mn}_{0.8}\text{Zn}_{0.2})_{(1-x)}\text{Ga}_x\text{Fe}_2\text{O}_4$.

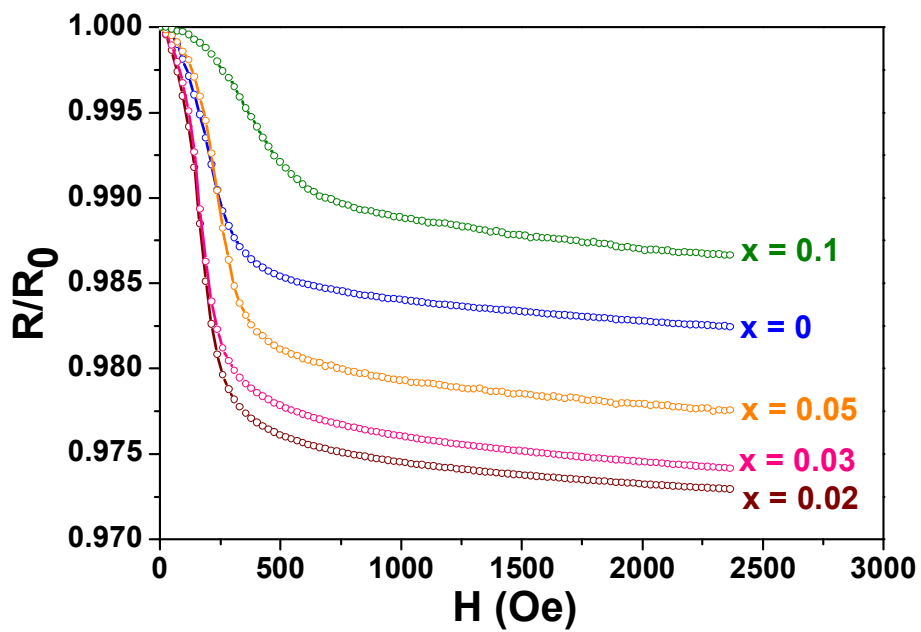


Fig. 6.7. $R(H)/R(H=0)$ at RT as a function of the applied magnetic field up to 0.3 kOe for Ga-doped MnZn ferrites with $x = 0, 0.2, 0.03, 0.05,$ and 0.1 .

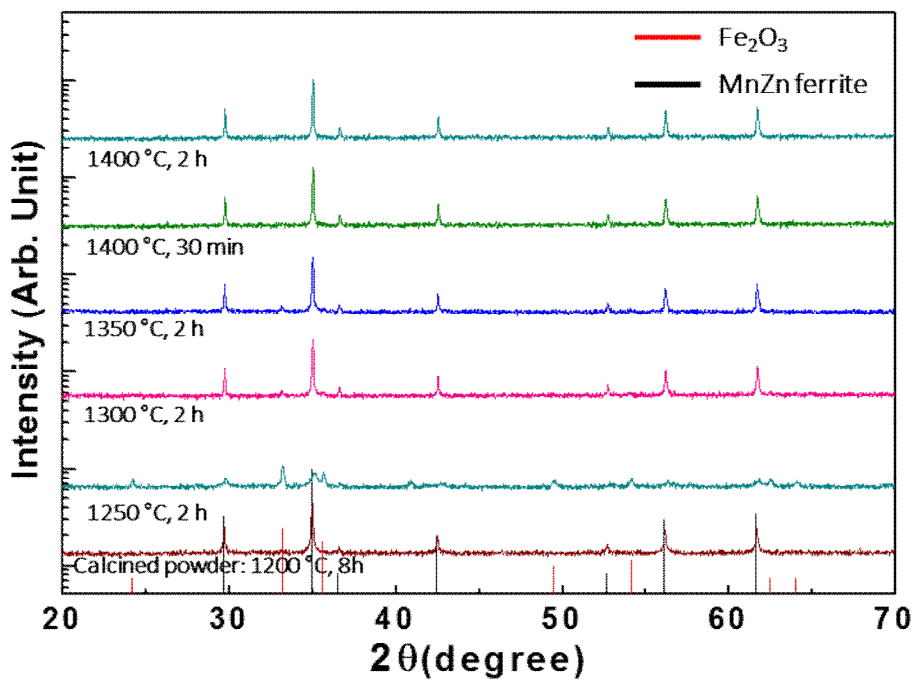


Fig. 6.8. XRD patterns of 2 mol% Ga-doped MnZn ferrite samples with various sintering conditions in air.

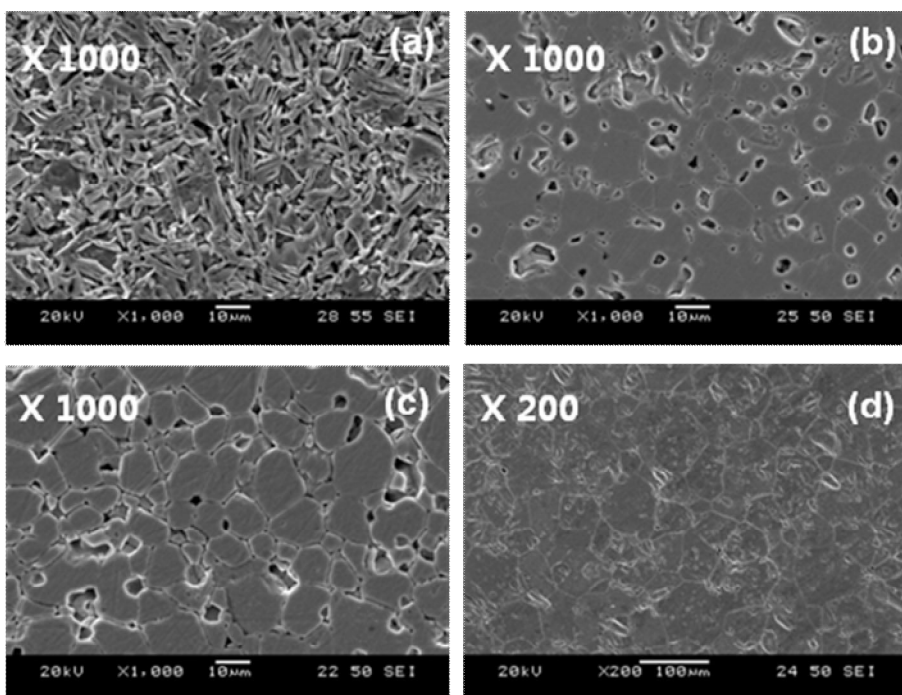


Fig. 6.9. SEM micrographs of 2 mol% Ga-doped MnZn ferrite samples sintered at (a) 1250°C, (b) 1300°C, (c) 1350°C, and (d) 1400°C for 2 h in air.

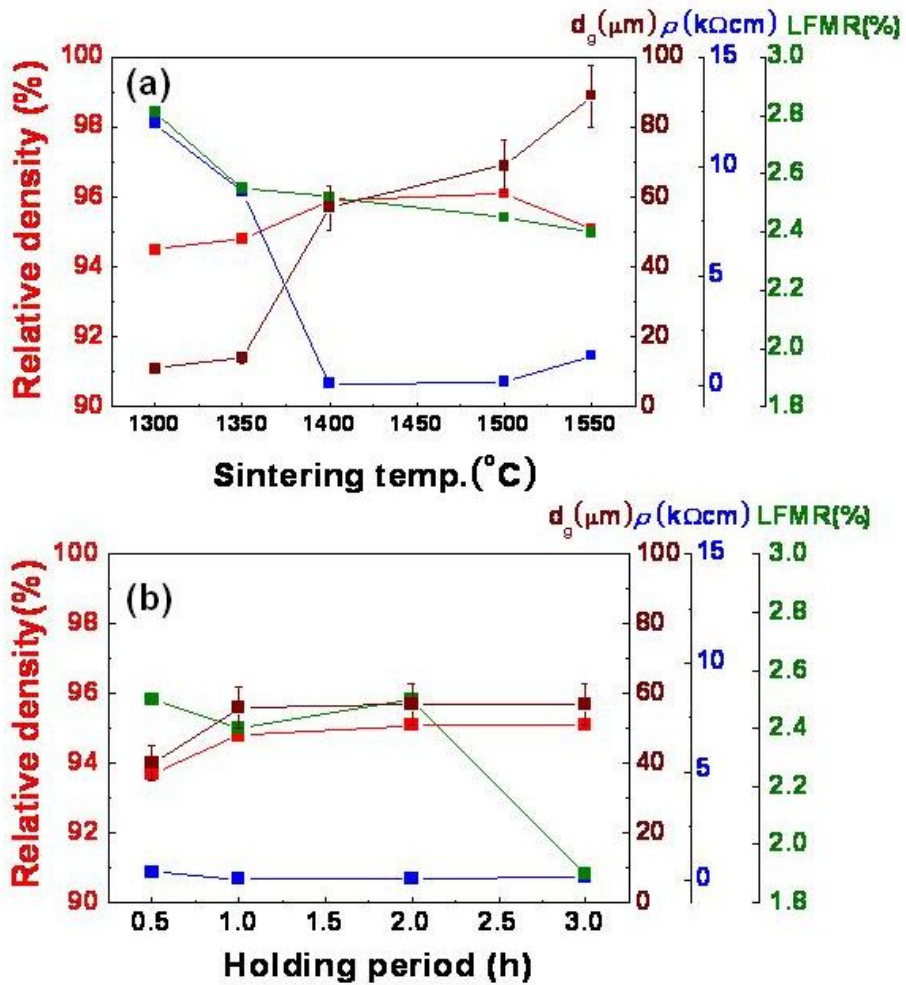


Fig. 6.10. The relationship among relative sintered density, average grain size (d_g), dc resistivity (ρ), and LFMR at RT of 2 mol% Ga-doped MnZn ferrite samples as a function of sintering temperatures (a) and holding periods (b). All samples were sintered for 2h in air in (a), and the sintering temperature was 1400°C in air in (b)

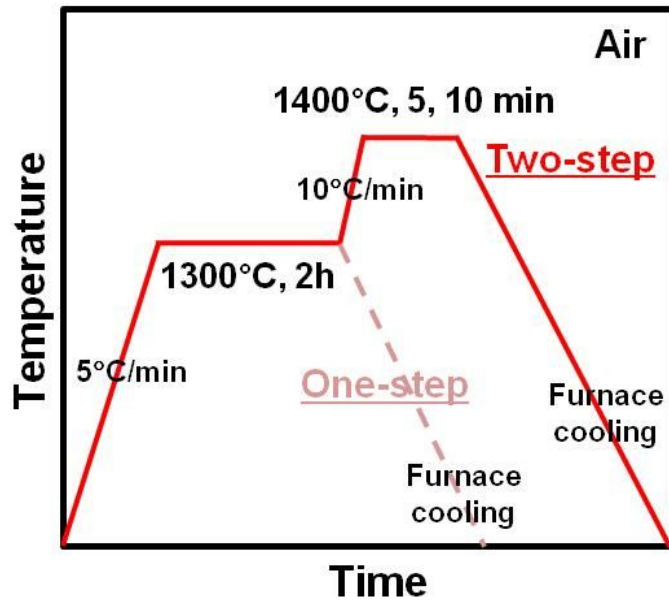


Fig. 6.11. The heat treatment schedules for the one step and two step sintering.

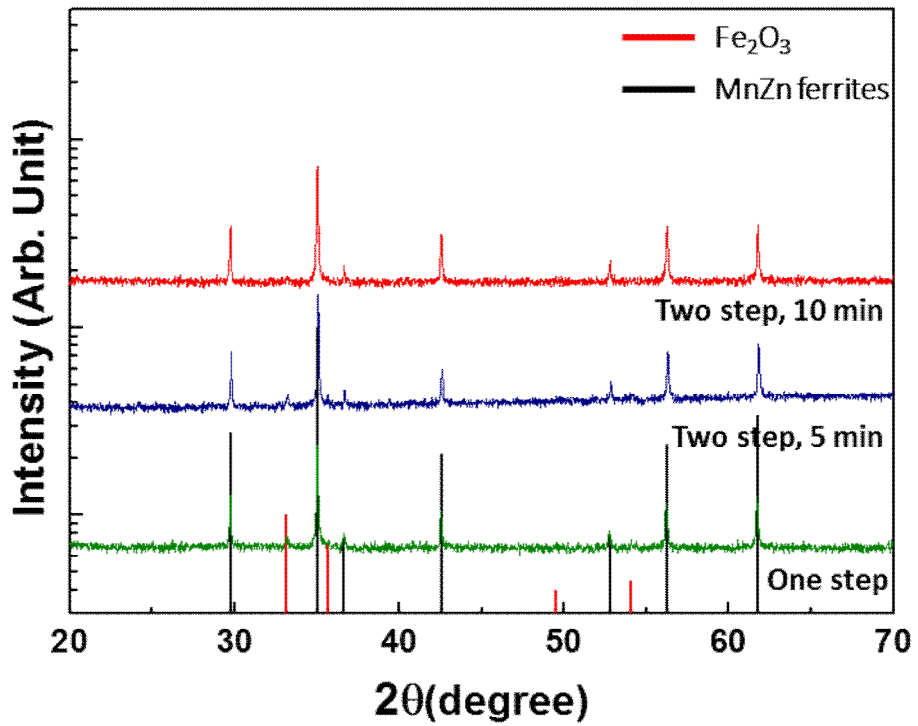


Fig. 6.12. XRD patterns of 2 mol% Ga-doped MnZn ferrite samples prepared by three different sintering conditions.

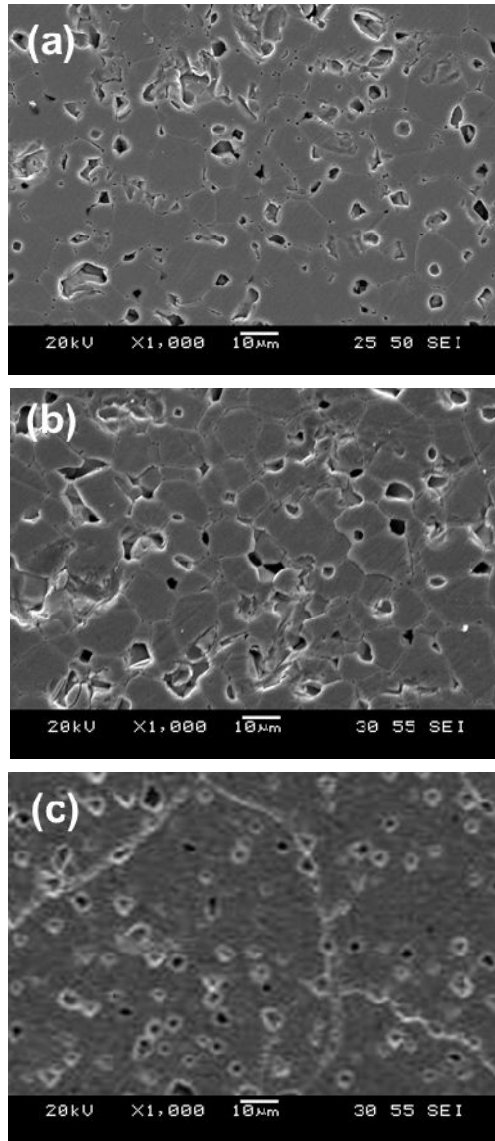


Fig. 6.13. SEM micrographs of MnZn ferrite samples with $x = 0.2$ sintered by (a) one step sintering, (b) two step sintering for 5 min, and (c) two step sintering for 10 min.

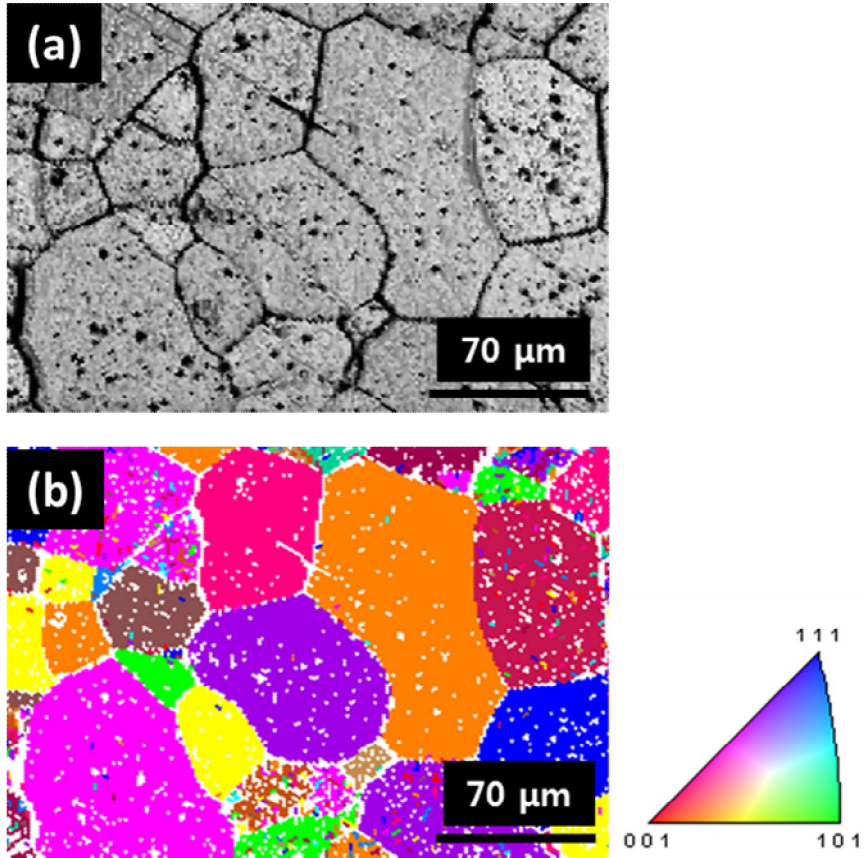


Fig. 6.14. SEM image (a) and its EBSD image (b) for 2 mol% Ga-doped MnZn ferrite sample sintered by two step sintering for 10 min.

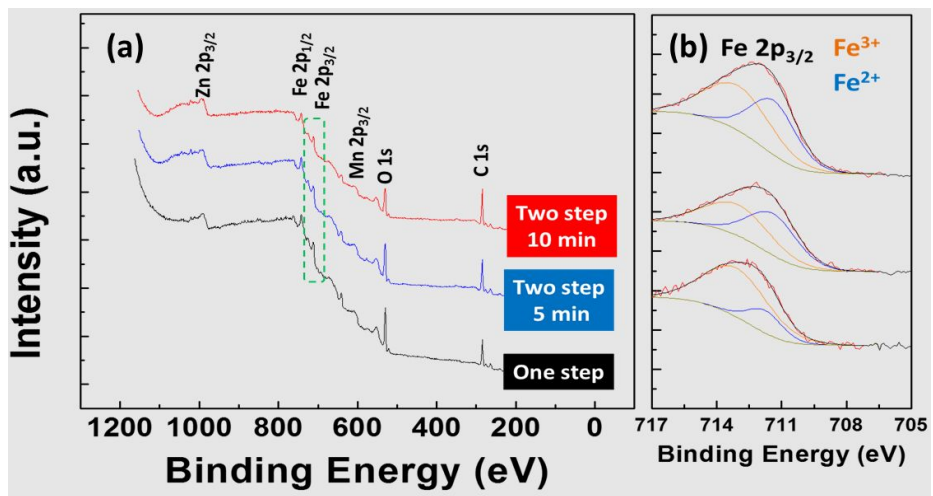


Fig. 6.15. (a) XPS data of 2 mol% Ga-doped MnZn ferrites prepared by three different sintering conditions. The dotted region in (a) was enlarged in (b).

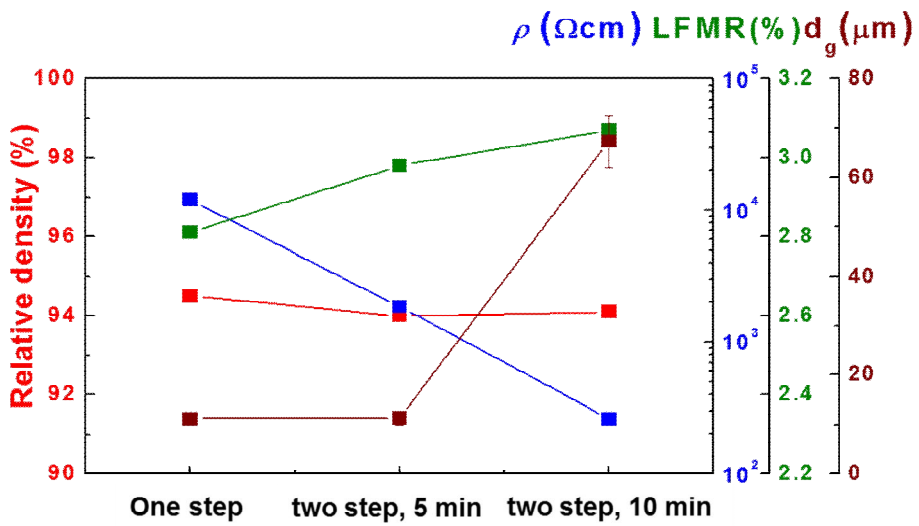


Fig. 6.16. The relationship among relative density, grain size (d_g), dc resistivity (ρ), and LFMR at RT of samples prepared by three different sintering conditions

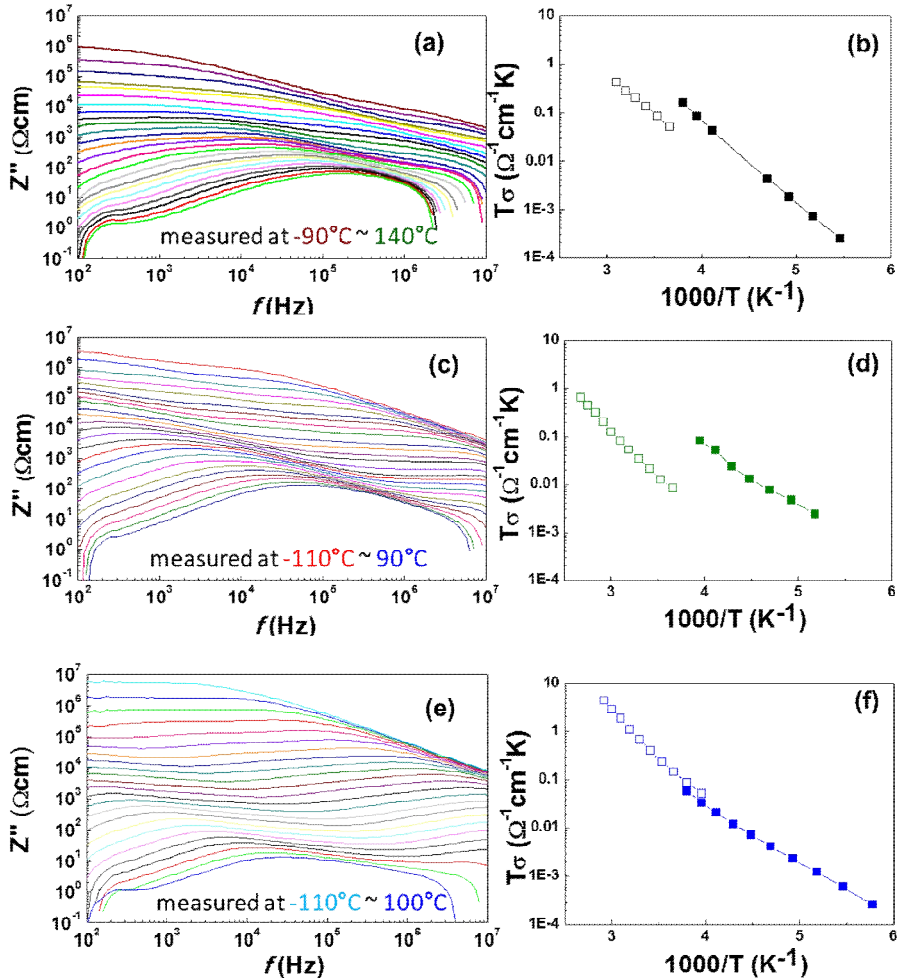


Fig. 6.17. Z'' properties of samples sintered by (a) one step sintering, (c) two step sintering for 5 min, and (e) two step sintering for 10 min in the measurement frequency ranging from 10^2 to 10^7 Hz. The Arrhenius plots of $T\sigma$ versus $1000/T$ of samples sintered by (b) one step sintering, (d) two step sintering for 5 min, and (f) two step sintering for 10 min.

Chapter 7. Summary

Although the LFMR effects have drawn a considerable attention in recent years, the LFMR effects have been unsatisfied for real applications due to relatively low MR value and low T_c . It is still critical drawbacks for practical application in the MR applications. Thus, in this research, we investigate enhanced LFMR effects in well known LSMO-based composites and new materials of doped MnZn ferrites for the real magnetic sensor application. Then, we also tried to clarify the mechanisms of high LFMR effects in doped MnZn ferrites. The LFMR effects in doped MnZn ferrites have been revealed, and the experimental results have been explained by magnetically disordered grain boundaries model. The major results of this literature are summarized as the following

First, we report the enhanced LFMR properties of composite bulks of (1-x) LSMO - x La₂O₃ (x= 0, 0.025, 0.05, 0.075, 0.1, 0.2, 0.3) prepared using the conventional solid state reaction. In order to improve the LFMR effect, grain boundary engineering is very crucial since more effective spin-dependent tunneling barriers are achievable at the grain boundaries. Since La₂O₃ phases are thermodynamically compatible with LSMO at high temperatures, all composite samples are composed of two different phases of LSMO and La₂O₃. While the T_c of all composites were almost unaltered in the range of 355~358 K, an optimally processed LSMO-La₂O₃ composite exhibited greatly enhanced LFMR of 2.22% at 300 K in 500 Oe with only one order increase in its resistivity in comparison with LSMO. We also tried to modify the LSMO grain boundaries of the LSMO-manganese oxide

composite by liquid phase sintering above the eutectic temperature between LSMO and Mn_2O_3 since a large increase in effective spin scattering center at the grain boundaries would be hopefully enabled by a eutectic structure of LSMO and manganite oxide after liquid phase sintering. We here report that it is possible to obtain improved LFMR effects from the LSMO-manganese oxide composites prepared by liquid phase sintering. The maximum LFMR value of 1.28% at 290 K in 500 Oe could be achieved from the composite sample of 30 mol% Mn_2O_3 addition. We also studied a LSMO based composite film system prepared by AD. As-deposited films by the AD method were post-annealed at 1100 and 1200°C for 2 h in air for the recovery of magnetism and also for a modification of LSMO grain boundary. While as-deposited films commonly exhibited a poor LFMR property with depressed T_c , post-annealed films exhibited a very good LFMR property with high T_c values ranging from 355 to 370 K. The highest LFMR value of 1.2% in 0.5 kOe and unprecedentedly high $(d\text{MR}/dH)_{\text{max}}$ value of 158.8 % kOe^{-1} were obtainable at 300 K from the LSMM composite film annealed at 1200°C. Compared with pure LSMO film, the LSMM composite films possess higher LFMR values with higher $(d\text{MR}/dH)_{\text{max}}$ values, which is mainly attributed to a greatly reduced magnetically disordered region near the LSMO grain boundary because of chemically compatible Mn_3O_4 phase.

Second, for the first time, we confirmed that the LFMR properties of Ga_2O_3 -doped Mn-Zn ferrites were systemically investigated the microstructures, electric properties, and magnetotransport properties depending on the various amounts of Ga_2O_3 and sintering conditions. Various amounts of Ga_2O_3 were doped to a pure Mn-Zn ferrite to have the nominal composition of $(\text{Mn}_{0.8}, \text{Zn}_{0.2})_{1-x}\text{Ga}_x\text{Fe}_2\text{O}_4$ ($x = 0\sim 0.1$). The maximum

LFMR value of 2.5% in 0.5 kOe at RT could be obtained from the $x = 0.02$ sample sintered at 1400°C for 2 h in air. In order to confirm the annealing condition effects on LFMR properties, 2 mol% Ga₂O₃-doped Mn-Zn ferrites were fabricated by two kinds of sintering processing schedule, which are named by one-step and two step sintering method. While one-step sintering means that the samples were directly ramped up to the sintering temperature, two-step sintering means that the samples were heated up to sintering temperature, and then more heated up to the final firing temperature, held for short time (5 and 10 min, in this experiment, respectively). From this studies, LFMR value of 3.1% in 0.5 kOe at RT is achieved from 2 mol% Ga₂O₃-doped Mn-Zn ferrites fabricated by two step sintering.

Finally, we clarified the origins of enhanced LFMR properties in MnZn-ferrites. The condition for LFMR observation have been revealed, and the experimental results have been explained by magnetically disordered grain boundaries model. The data measured by complex impedance (Z^*) spectroscopy revealed that the variation of LFMR values in samples was exactly coincident with those of differences in activation energy (E_a) values between grain and grain boundary. With increasing the difference in E_a between grain and grain boundary, LFMR value of samples was increased.

Publications

Papers (SCI journals)

- **H. J. Kim**, S. I. Yoo “Enhanced low field magnetoresistance in $\text{La}_{0.7}\text{Sr}_{0.3}\text{MnO}_3 - \text{La}_2\text{O}_3$ composites” *Journal of alloys and compounds* 521 (2012) 30
- **H. J. Kim**, D. G. Yoo, S. I. Yoo “Large planar Hall effect in the $\text{La}_{0.7}\text{Sr}_{0.3}\text{MnO}_3$ thin films at room temperature” *Materials Letters* 123 (2014) 23
- **H. J. Kim**, J. H. You, S. M. Choi, and S. I. Yoo “Magnetic and magneto-transport properties of $\text{La}_{0.7}\text{Sr}_{0.3}\text{Mn}_{1+d}\text{O}_3$ – manganese oxide composites prepared by liquid phase sintering” *journal of magnetics (submitted)*
- **H. J. Kim**, Y. J. Yoon, and S. I. Yoo “Magneto-transport properties of $\text{La}_{0.7}\text{Sr}_{0.3}\text{MnO}_3$ -manganese oxide composite films on YSZ substrates prepared by aerosol deposition” *Ceramics international (submitted)*
- **H. J. Kim**, and S. I. Yoo “ Excellent low field magnetoresistance and transport properties of Ga_2O_3 -doped MnZn ferrites” *Applied physics letters (to be submitted)*

Contributed papers (SCI journals)

- Y. M. Kang, H. J. Kim, S. I. Yoo “Excellent low field magnetoresistance properties of the $\text{La}_{0.7}\text{Sr}_{0.3}\text{Mn}_{1+d}\text{O}_3$ – manganese oxide composites” *Applied physics letters* 95 (2009) 052510
- Y. M. Kang, H. J. Kim, S. I. Yoo “Enhanced low field magnetoresistance $\text{La}_{0.7}\text{Sr}_{0.3}\text{Mn}_{1+d}\text{O}_3$ – Mn_3O_4 composite films prepared by ex-situ phase crystallization” *Journal of magnetics* 14 (2012) 265

초 록

본 학위 논문에서는 페로브스카이트를 기본구조로 하는 $\text{La}_{0.7}\text{Sr}_{0.3}\text{MnO}_3$ (LSMO) 기반의 복합체와 스피넬 구조의 $\text{Mn}_{0.8}\text{Zn}_{0.2}\text{Fe}_2\text{O}_4$ 에서의 저자장 자기저항효과 (low field magnetoresistance, LFMR)에 관한 연구이다. LFMR 효과는 다결정을 갖는 강자성체 물질에서 나오는 현상으로 결정립계를 지나는 전자의 스핀의존산란 효과에 의한 것이다. LSMO 물질은 상대적으로 높은 전이온도 (~ 370 K)를 갖으며 LFMR 효과를 나타내는 물질 중에 가장 우수한 특성을 나타내는 것으로 알려져있다. 본 연구에서는 순수한 LSMO 물질에 상평형도상 LSMO 물질과 화학적으로 안정한 La_2O_3 와 manganese oxide를 이차상으로 첨가하여 미세구조를 조절하였고 최종적으로 벌크 및 박막에서 그 특성을 극대화 하였다. 보통 LSMO에 절연체를 이차상으로 첨가 할 경우 고온에서 서로 반응하여 전이온도의 감소 및 비저항 증가 등의 문제가 발생한다. 본 연구에서는 이러한 문제를 피하고 순수한 LSMO 물질보다 좀 더 높은 LFMR 효과를 구현할 수 있었다. LSMO에 La_2O_3 를 이차상으로 첨가한 복합체의 경우 고상소결법을 통하여 제조하였고, manganese oxide 를 이차상으로 첨가한 복합체의 경우 액상소결법을 통해 제조하여 공정상을 갖는 미세구조를 구현하였다. LSMO- La_2O_3 복합체에서 상온, 0.5 kOe의 자장하에 최대 2.2%의 LFMR 값을 보였으며 LSMO-manganese oxide 복합체에서 동일 조건하에 1.3%의 LFMR 값을 보였다. 실제 순수한 LSMO 물질의 LFMR 값은 약 1% 정도이며 비저항은 약 $10^{-3}\Omega\text{cm}$ 의 값을 보이는 반면 LSMO- La_2O_3 복합체에서 비저항의 증가가 10배

증가한데 반해 LFMR 값이 2%가 넘는 우수한 결과를 얻을 수 있었다. 하지만 La_2O_3 상은 매우 흡습성이 강한 물질로써 공기중에서 본 물질을 사용하기 위해서는 추가적인 표면 코팅이 필요하다. LSMO-manganese oxide 복합체에서도 마찬가지로 향상된 LFMR 값을 얻을 수 있었으며 비저항의 증가는 거의 발생하지 않았다.

실제 LFMR 현상을 이용하여 자기저항 소자로써 상용화 하기 위해서는 박막소자로 제조하여 그 특성을 구현해야 한다. 지금까지 다양한 박막 제조법을 이용하여 벌크에서 얻는 특성을 박막에서도 구현하고자 많은 연구가 진행되고 있다. 하지만 박막으로 제조하게 될 경우 그 특성이 벌크에서 얻어지는 것 보다 현저히 떨어져 낮은 LFMR 변화를 보이며 또한 비저항의 증가 등의 문제를 야기시켰다. 본 연구에서는 이러한 문제를 해결하고 동시에 벌크와 비슷한 LFMR 특성을 얻고자 에어로졸 증착법을 통하여 박막을 증착하고 후열처리 법을 통하여 결정성 및 미세구조를 조절하여 그 특성을 극대화 시키고자 하였다. 에어로졸 증착에 앞서 박막으로 증착 될 LSMO와 LSMO-manganese oxide 복합체를 하소 과정 및 밀링 과정을 거쳐 분말을 제조 하였고 증착 된 박막은 두께가 약 $3\mu\text{m}$ 정도의 비정질 후막으로 제조 되었음을 확인하였다. 비정질 후막을 결정화 시키기 위하여 $1000 \sim 1200^\circ\text{C}$ 에서 후열처리를 진행하였으며 모든 박막에서 1000°C 이상에서 다결정질로 결정화가 이루어 지는 것을 확인하였다. 실제 복합체 박막을 1200°C 에서 후열처리할 경우 가장 우수한 LFMR 변화를 보였으며 상온, 0.5 kOe 자장하에서 약 1.2%의 LFMR 값을 보였다. 흥미롭게도 자장 민감도를 나타내는 특성인 dMR/dH 값이 실제 벌크 보다 박막에서 10배 이상 높게 나타났으며 ($\sim 158\%/\text{kOe}$ at 300 K in 0.5kOe) 이러한 결과는 LFMR 특성을 이용한 자기저항 센서 소자로써의 상용화 가능성을

매우 높은 것으로 사료된다.

본 학위 논문에서는 LSMO를 기반으로 하는 복합체뿐만이 아니라 스피넬 구조를 갖는 MnZn 페라이트에서 처음으로 LFMR 현상을 확인 하였으며 또한 Ga이 치환된 MnZn 페라이트에서 매우 우수한 (3.1% 상온, 0.5 kOe) 특성을 구현하였다. 즉, 스피넬 구조에서 4면체 자리에 위치한 $(\text{MnZn})^{2+}$ 에 Ga^{3+} 이온을 치환함으로써 홀 도핑에 의한 비저항의 감소를 유도하였고 동시에 높은 LFMR 특성을 구현하고자 하였다. 실제 Ga_2O_3 를 2 mol% 치환한 샘플에서 가장 우수한 LFMR 특성을 얻었으며 (2.5%, 상온, 0.5 kOe) 순수한 MnZn 페라이트 (1.5%, 상온, 0.5 kOe)에 비교하여 비저항 또한 5배 이상 감소시킬 수 있었다. 추가로 열처리 조건에 따른 특성의 최적화를 위하여 2 mol% Ga_2O_3 를 치환한 MnZn 페라이트 분말을 이용하여 소결 조건을 변화시켜가며 실험을 진행하였다. 소결 온도를 1250–1550° C, 유지 시간을 30분–4시간 변화를 주어 실험을 진행하였으며 약 1350° C 에서부터 비정상 입자 성장이 발생하는 것을 확인하였다. 1300° C에서 2시간동안 소결할 경우 평균 결정립 크기가 약 10 μm 정도인 샘플을 얻을 수 있었으며 1400° C 이상의 온도에서 소결 할 경우 약 60 μm 정도의 평균 결정립 크기를 갖는 샘플을 제조 할 수 있었다. 실제 상대적으로 결정립 크기가 작은 샘플에서 조금 더 우수한 LFMR 특성을 구현하였으며 그 값은 상온에서 0.5 kOe 자장하에 약 2.8%를 갖는 것으로 확인하였다. 하지만 본 샘플의 경우 매우 높은 비저항으로 ($\sim 10^4 \Omega\text{cm}$) 따라서 추가적인 연구로 높은 자기저항값을 유지하면서 동시에 낮은 비저항을 갖는 새로운 소결법을 고안하였다. 기존의 소결법은 해당 소결온도에서 1차 소결 후 노냉각하는 방법 (1단계 소결)이지만 추가 연구로 고온에서의 유지를 2차에 걸쳐 시행한 후 노냉각하는 방법 (2단계 소결)을 사용하였다.

이는 1300° C에서 소결한 후 1400° C에서 단시간 유지하여 상대적으로 작은 결정립 크기를 갖으며 동시에 낮은 비저항을 얻고자 고안해 낸 방법이다. 실제 스피넬 페라이트에서 8면체에 위치하고 있는 Fe 이온은 1300° C 이하에서 Fe³⁺로 존재하고 있으며 그 이상의 온도에서는 Fe²⁺로 양이온 가수가 변하게 된다. 이는 최종적으로 Fe²⁺와 Fe³⁺ 사이의 전자 호핑이 증가하여 재료의 비저항을 낮추는 결과를 얻게 된다. 이러한 점을 이용하여 2 mol% Ga₂O₃를 치환한 MnZn 페라이트를 2단계 소결법을 수행하였으며 최대 3.1%의 높은 LFMR 변화율과 상대적으로 낮은 비저항 (~10² Ωcm)을 갖는 샘플을 제조 할 수 있었다. 마지막으로 본 연구에서 처음으로 제시한 MnZn 페라이트에서의 LFMR 현상에 대한 메커니즘을 명확히 하고자 임피던스 분석을 시행하였으며 결정립과 결정립계의 전기적 특성 (비저항, 정전용량, 활성화 에너지)을 각각 구하여 미세구조 및 전자기적 특성이 본 물질의 저자장 자기저항의 변화 효과에 어떻게 기인하는지 확인하였다.

주요어: 페로스카이트 망간산화물, 스피넬 페라이트, La_{0.7}Sr_{0.3}MnO₃ (LSMO), LSMO-기반 복합체, MnZn 페라이트, 에어로졸 증착, 후열처리, 저자장 자기저항 효과, 스핀의존산란, 자기수송특성, 자기적 특성, 전기적 특성

학 번: 2008-20640